The Philosophical Magazine

UNIVERSITY OF HAWAII
LIBRARY
FEB '61

FIRST PUBLISHED IN 1798

A Journal of Theoretical Experimental and Applied Physics

Vol. 5 December 1960 No. 60
Eighth Series

25s. 0d., plus postage
Annual Subscription £13 10s. 0d., payable in advance

ALERE FLAMMAM

Printed and Published by
TAYLOR & FRANCIS LTD
RED LION COURT, FLEET STREET, LONDON, E.C.4

THE PHILOSOPHICAL MAGAZINE

Editor

Professor N. F. Mott, M.A., D.Sc., F.R.S.

Editorial Board

Sir Lawrence Bragg, O.B.E., M.C., M.A., D.Sc., F.R.S.
Sir George Thomson, M.A., D.Sc., F.R.S.
Professor A. M. Tyndall, C.B.E., D.Sc., F.R.S.

Authors wishing to submit papers for publication in the Journal should send manuscripts directly to the Publishers.

Manuscripts should be typed in *double* spacing on one side of quarto (8 × 10 in.) paper, and authors are urged to aim at absolute clarity of meaning and an attractive presentation of their texts.

References should be listed at the end in alphabetical order of authors and should be cited in the text in terms of author's name and date. Diagrams should normally be in Indian ink on white card, with lettering in soft pencil, the captions being typed on a separate sheet.

A leaflet giving detailed instructions to authors on the preparation of papers is available on request from the Publishers.

Authors are entitled to receive 25 offprints of a paper in the Journal free of charge, and additional offprints can be obtained from the Publishers.

The *Philosophical Magazine* and its companion journal, *Advances in Physics*, will accept papers for publication in experimental and theoretical physics. The *Philosophical Magazine* publishes contributions describing new results, letters to the editor and book reviews. *Advances in Physics* publishes articles surveying the present state of knowledge in any branch of the science in which recent progress has been made. The editors welcome contributions from overseas as well as from the United Kingdom, and papers may be published in English, French and German.

The Soft X-ray Spectra of Lithium, Magnesium and Aluminium and their Alloys†

By R. S. CRISP‡ and S. E. WILLIAMS
Department of Physics, University of Western Australia

[Received June 30, 1960]

ABSTRACT

The Li K and Mg L_{23} spectra have been observed from a range of Li–Mg alloys, evidence for electron transfer from Mg being obtained. More distinct changes have been observed for the same spectra when Li was evaporated onto solid Mg and Mg onto solid Li. Changes in the Li K and Al L_{23} were observed when Li was evaporated onto Al and in the Al L_{23} when Al was evaporated onto Mg. No changes greater than 5×10^{-2} ev were observed in edge wavelengths or edge widths although marked depopulation of higher energy states occurred in Mg and Al. It is inferred that changes in the screening of K and L levels compensate almost exactly for the effects of electron transfer. The results of Catterall and Trotter (1959) were confirmed in that the Mg band contracted and the Li band extended on the low-energy side. Li deposited on Al shows a K spectrum without any metal edge, suggesting that the first zone is filled and that there is no overlap with the second zone.

§ 1. INTRODUCTION

THE effect of alloying on the valence band energy levels of metals of low atomic number has been the subject of a number of investigations. Earlier work seeking possible changes in the soft x-ray spectra was hampered by the difficulties of photographic photometry in this region which makes accurate measurements of intensities almost impossible to obtain. The attendant need to dissipate large amounts of power in the alloy target and the inability of the photographic method to detect the short-term effects of target contamination are added handicaps. As a consequence few definite and confirmed effects resulting from alloying have been recorded.

Photoelectric detection based on photon-counting enables the reproduction and measurement of intensities to 1 or 2% in this region. The power dissipated in the target is reduced to about one-hundredth of that needed for photography, and changes of intensity with time resulting from target contamination can be observed and therefore often avoided.

The first changes caused by alloying in the Li–Mg system observed by photoelectric means were reported by Catterall and Trotter (1959). Evidence was obtained pointing to electron transfer from the constituent of higher to the constituent of lower valency while the spectrum of each constituent retained a recognizable though somewhat modified identity.

---

† Communicated by the Authors.
‡ Now at National Research Council, Ottawa.

The observations reported below, though based initially on the same alloy system, recorded the most marked changes in metallic combinations not normally regarded as involving alloying since they consisted of evaporated layers of one constituent on a solid, cooled base of the other. Since the changes can be most effectively interpreted in terms of electron transfer, alloying, even though it be very restricted in the dimension of depth, is assumed to occur.

§ 2. EXPERIMENTAL

The emission spectra were obtained with the photon-counting spectrometer previously described (Fisher *et al.* 1958). In the initial experiments on Li–Mg alloys, target currents up to 11 mA and voltages of 4 kv were used. The pressure in the specimen chamber was about 10^{-5} mm and carbonaceous contamination of the target surface by decomposed residual vapours was serious. With this type of contamination intensities decrease linearly with time (Crisp 1958 a). Subsequently the vacuum in the specimen chamber was improved to $1–2 \times 10^{-6}$ mm and the target was almost completely surrounded by a copper baffle cooled to $-115°$c by external conduction (Pollard 1953) to a rod immersed in liquid air. The cooling could be maintained indefinitely and the target was kept under vacuum for one or two days before making observations. So long as the baffle was cooled below $-100°$c carbonaceous contamination was reduced to a negligible amount. A glass window allowed observation of the interior of the specimen chamber.

The target current was stabilized to 0·5% (Crisp 1958 b), enabling relative intensities to be reproduced to within 1 or 2%. The variable speed drive was replaced by a gearbox with fixed speeds so that spectra could be accurately reproduced to a chosen wavelength scale. The use of more sensitive photomultipliers† allowed the reduction of target currents to about 1 mA. The aluminium grating used in previous work was replaced by a glass grating of similar constants. The resolution, calculated according to the criterion of Fisher (1954), was maintained at 0·9 Å.

A four-sided target with faces of Cu, Al, Mg and Be was used so that spectra for the relevant elements either from the solid or from evaporated layers on Cu could be recorded without breaking the vacuum. Solid Li specimens were accommodated in a different target. The tungsten carbide scraper was used to clean target surfaces when required. The target area covered by the electron beam is about 10 × 5 mm.

All spectra reproduced have been traversed from the high-energy side so that the recorder trace (i.e. the time axis) runs from right to left. The chart speed was always one inch per minute. If contamination is occurring the low-energy side will be reduced in intensity and the maximum may be shifted slightly towards higher energies. All wavelengths in a given spectrum appear to show similar rates of contamination with the exception of the Li 'line' at 253 Å which grows approximately as $[1-\exp(-xt)]$. The appearance of this 'line' and the closely associated fluroescence of the Li target will be discussed elsewhere, but it should be recorded that after it was discovered that a massive evaporation of Li has the effect of suppressing the appearance of the 'line' this precaution was always taken before recording a Li spectrum.

---

† Made by the Institut für technische Physik der E.T.H. (Abteilung für Industrielle Forschung).

Our Li K spectrum has been published elsewhere (Crisp and Williams 1960). The Mg L_{23} and Al L_{23} spectra seen by our instrument are shown in figs. 2 and 5† respectively. Although the resolution is insufficient to record the full height of the Al 'spike', the small kink at about 181 Å is always seen and constitutes a real feature of the spectrum not previously recorded. Its position corresponds to the minimum in Matyas' theoretical N(E) curve (Tomboulian 1957) which marks the lowest energy for states in the second Brillouin zone.

Edge wavelengths, taken at half maximum intensity of the edge were checked by reference to the fiducial marks made on the recorder trace at every revolution of the lead screw. Variations less than 0·2 Å (equivalent to about 0·05 ev) are considered to be within the limits of experimental error. Edge widths, taken between the points of 5% and 95% maximum intensity can be measured to the same accuracy.

§ 3. LITHIUM–MAGNESIUM ALLOYS

Solid specimens of alloys of Mg–Li containing 15, 40 and 70 at. % Li were examined. The alloys were received as metal bars contained in a clear, but unidentified packing oil. Specimens were milled to shape using the packing oil as cutting fluid. They were pressed into a frame which was soldered to the target holder with Woods' metal. Heating of the specimens was in this way kept to a minimum. Any oxidation of the target surface was subsequently removed in vacuum by the scraper. Thermal contact of the specimens with the water-cooled target holder was poor.

At target currents up to 11 mA and a pressure 8×10^{-6} mm a rapid time variation of intensity was observed for both Mg and Li. The form of the variation is shown in fig. 1. As the Li intensity increased a strong blue fluorescence appeared over the bombarded area. The time variation suggested that under the action of the beam Li atoms were migrating to the surface. Although spectra can be recorded at a time when the variation of intensity is slow, it is doubtful whether the surface layer examined has the same composition as the original alloy.

Subsequently, in the improved vacuum and with improved sensitivity, the intensity variation was examined for target currents between 0·7 and 4 mA. The intensity was then found to decay exponentially for both constituents with a half-intensity period about one minute for the 30/70 and 60/40 alloys and somewhat larger for the 85/15 alloy. This is approximately the same as the half-period for growth of the Li 'line'.

---

† Figures 2–5 are shown as plates.

Figure 2 shows recorded spectra† for the three alloys together with the spectrum of pure Mg. Contamination in these cases is slower but in the 30/70 alloy the Mg has disappeared in less than 9 min and has been replaced by the Li 'line'.

In general the changes in the Mg spectra agree with the results of Catterall and Trotter (1959). There is a distinct diminution of the Mg 'spike', indicating a depopulation of the higher electron states. This diminution becomes more marked as the fraction of Li increases, though its exact extent is masked by the overlap of the Li 'line'. The edge wavelength does not change appreciably and there is no convincing evidence that the edge is broadened. The low-energy maximum appears to shift from 261 Å in pure Mg to about 257 Å in the alloys, but this may again be caused by the Li 'line'. Because of low intensities and the effects of contamination it was not possible to obtain information about the shape of the Li K spectrum.

Fig. 1

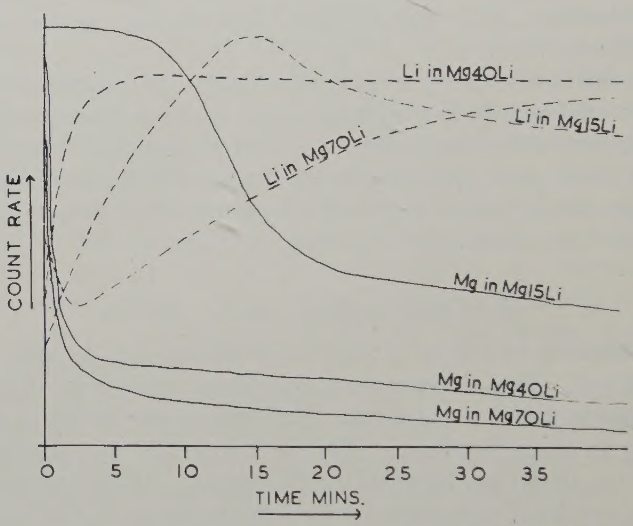

Time variation of intensity (counts per second) for Li K and Mg L_{23} spectra in various Li–Mg alloys. Target current 11 mA voltage 4 kv. Pressure 10^{-5} mm.

§ 4. Evaporated Layers

Since it appeared, from the intensity changes obtained with high target powers, that Li atoms were migrating toward the surface and possibly producing a lithium-rich layer on the surface, it was decided to look at the Mg spectrum when a lithium-rich layer was deliberately produced by evaporating Li onto a solid Mg target. The result was surprising. The Mg spectrum was modified to a much greater extent than in the alloy spectra. Subsequently, Mg was evaporated onto Li, producing further big changes in the Mg spectrum. The effect of evaporating Li, Na and K onto Be, Mg and Al was examined. Combinations for which alloying does not normally occur showed no spectrum changes. The only appreciable changes involved combinations of Li, Mg and Al which are discussed below.

---

† Date, target, full-scale count rate, percentage error at half-full scale (Elmore and Sands 1949) target current and voltage, optical resolution and pressure are recorded on each spectrum reproduced.

Examples of recorded spectra illustrating the effect of evaporating Li onto Mg and Al, Mg onto Li and Al onto Mg are shown in figs. 3, 4, and 5. Contamination was appreciable only in the case of Mg on Li where it has the effect of reducing intensities on the low energy side of the spectrum.

The changes in the spectra are so marked that it is assumed they are due to alloying, either instantaneously by diffusion following release of latent heat by the condensing element, or very rapidly under the action of the bombarding electrons, even though the underlying constituent is held at the temperature of the cooling water. In the interval of less than a minute between ceasing evaporation and recording the maximum of the Mg peak the changes have been completed. Alloying in thin films has been discussed by Weaver and Hill (1959) who record that Michel (1956) observed immediate alloying following successive evaporation of Ag–Zn and Ag–Sn. Michel's suggestion that alloy formation is observable for metal pairs whose diffusion constants at room temperature are larger than $10^{-20}\,\mathrm{cm}^2/\mathrm{sec}$ is not consistent with the observation of changes in the L_{23} spectrum of Al deposited on Mg, the only pair for which diffusion constants are available. Fujiki (1959) has observed instantaneous alloying following successive depositions of metal vapours on a Formvar film, but in this case the latent heat released is sufficient to raise the temperature of the film. However, Fujiki showed that alloy formation was promoted by small grain size and large area of the substrate surface. Target surfaces subjected to repeated scraping would meet these requirements. The Li–Mg, Li–Al and Al–Mg systems have not been studied by electron diffraction.

Film thicknesses could not be quantitatively controlled, although a degree of control was obtained by running the furnace at minimum power for evaporation and switching off at different intervals after a visible film first appeared. In this way 'thin' and 'thick' films could be deposited. As the emission spectrum is produced in a surface layer of the order of 10^4 Å thick (Skinner 1940), it is assumed that for appreciable emission to be observed the film thickness could be at least of the order of 10^3 Å.

The spectra of each element are discussed separately below to facilitate comparison of the modifications with the spectrum of the pure metal.

§ 5. MAGNESIUM

The L_{23} spectrum of pure Mg seen by our instrument is shown in fig. 2. In fig. 3 are shown the spectra of Mg when overlain by Li and when evaporated onto solid Li. In fig. 6 various Mg spectra have been superimposed with the intensity at the low-energy maximum adjusted to a constant value, the remainder of the spectrum being normalized accordingly.

Three spectra of pure Mg were averaged; three of Mg under Li, four of Mg over Li and four of Mg in Mg_2Sn. The wavelength of the high-energy edge has in each case been calculated by comparison with the edge of pure Mg obtained with the grating in the same adjustment. The averaged curves are taken from spectra in which evaporation has been continued until no further changes occur in the shape of the Mg spectrum. A light evaporation reduces the Mg spike slightly making the spectrum resemble that from an Mg–Li alloy.

Fig. 6

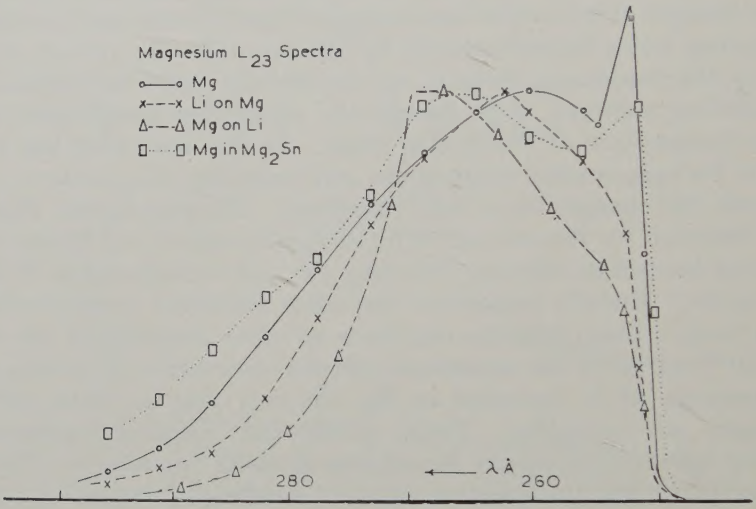

Smoothed averages of three spectra of pure Mg, three of Mg under Li, four of Mg deposited on Li and four of Mg in powdered Mg_2Sn. Intensities normalized to make the low-energy maxima equal.

From fig. 6 it is concluded that the edge wavelength is constant within the experimental uncertainty (5×10^{-2} ev), and that the width of the edge between the 5% and 95% maximum intensity points is similarly constant. Although the change in position of the low energy maximum from 260 Å for pure Mg to about 262 Å for Mg under Li is not established with certainty, the change to a flatter maximum with a mean at 267 Å for Mg on Li is real. This change represents a decrease of more than one electron volt in the energy of the states making contact with the boundary of the first Brillouin zone. Together with this shift in the maximum, the ratio of maximum intensity at the edge to maximum intensity in the band is 68% (probable error 1·5% from 17 spectra) for Li on Mg and 51% (probable error 3% from four spectra) for Mg on Li. The two spectra are quite distinct. On the low-energy side the Mg bandwidth is decreased in Mg under Li relative to pure Mg by about 0·5 ev. A similar decrease is found by comparing averaged spectra taken with the aluminium grating. This is in agreement with the results of Catterall and Trotter for Mg–Li alloys.

Although the Mg on Li shows a more marked decrease, this is largely if not wholly due to contamination. Assuming the contamination produced an exponential decrease in intensity (since it was associated with the appearance of fluorescence and the Li 'line') a rough correction of the intensities in the tail shows no definite decrease in the band width.

Li can dissolve in Mg to about 18 at. % and since the Mg remains in its h.c.p. state the Mg spectrum should not be much changed in shape. This is found to be so for Li on Mg. Mg can dissolve in Li to about 70 at. % Mg but the structure is b.c.c. and the Mg spectrum should be modified appropriately. The distinct difference between the Mg spectra noted above suggests that the Mg deposited on Li dissolves in the Li.

Between the maximum at 262 Å and the kink at 255 Å the intensities for pure Mg are higher than for Mg under Li. This difference, together with the possible shift of the maximum may result from a dilution of the spectrum of Mg containing dissolved Li by a small contribution from the spectrum of Mg dissolved in Li. In the case of Mg on Li the situation is reversed and the spectrum of Mg on Li may be diluted though the distinctive shape of the maximum is not lost.

Figure 6 also includes an averaged Mg spectrum from the intermetallic compound Mg_2Sn in powder form. Counting rates were low and the background was high in the four spectra averaged and only the general trend of the curve is significant, the position of the low energy maximum and the breadth of the band near the tail being to some extent dependent on the choice of background intensity. Since Mg_2Sn has a fluorite structure it was to be expected that the Mg L_{23} spectrum from this compound would be modified. However, it closely resembles the spectrum of pure Mg, the edge wavelength and edge width being unchanged. There is some indication of an increased band-width on the low-energy side. The result does not support Farineau's (1937) observation of similar K spectra for the constituents of the Al–Mg intermetallics, Al_2Mg_3 and Al_3Mg_2.

When Al is evaporated onto Mg no changes are observed in the Mg spectrum although as will be seen from fig. 5 the Al L_{23} is changed. Since a normal Mg L_{23} spectrum will be produced from the solid Mg target, this will be observed as well as that from the Mg in contact with the Al.

§ 6. ALUMINIUM

Figure 4 shows three recordings of the Al L_{23} spectrum for increasing thicknesses of Li deposited on solid Al. Figure 5 shows the normal Al spectrum seen by our instrument in which the resolution is insufficient to show the full extent of the high energy spike. There is also shown in fig. 5 the spectrum of Al evaporated onto Mg. Figure 7 shows the result of averaging three spectra of Al, four spectra of Al with a superimposed 'thick' layer of Li and two spectra of Al deposited on Mg.

The point chosen on the Al spectrum at which to normalize the intensities has been taken at about 189 Å. This is well below the maximum intensity of states in the first zone and was chosen on the assumption that the population of states in the first zone of Al would not be affected by alloying because the second zone is half-filled. This assumption is not borne out when the results are analysed.

The trend of absorption by Li is also indicated in fig. 7 following Skinner and Johnson (1937), with an arbitrary zero corresponding to the absorption at the low-energy side of the K edge. Li absorption should be roughly constant to the high-energy side of the normalizing wavelength. On the low-energy side there are two increases to a maximum at 196 Å which qualitatively correspond to the two regions in which the intensity of the modified spectrum of Al falls below that of pure Al. However, no quantitative match has been achieved and it appears that the N(E) curve of Al is modified in this region. The spectrum of Al on Mg shows distinct divergencies from that of pure Al in the same region and since these latter cannot be attributed to absorption they constitute further evidence for changes in the N(E) curve for the first zone.

Fig. 7

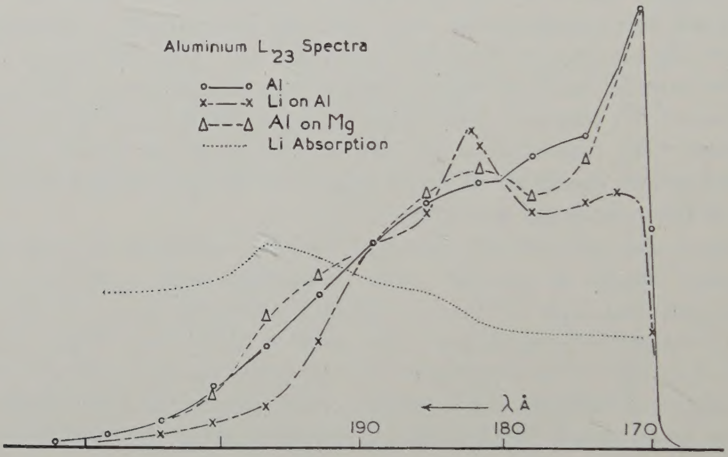

Smoothed averages of three L_{23} spectra of pure Al, four spectra of Al with a superimposed ‘ thick ’ layer of Li and two spectra of Al deposited on Mg. Intensities have been normalized to the same value at 189 Å. Kinks in the pure Al spectrum at 173 Å and 181 Å are reproducible. Li absorption in this region is also shown with an arbitrary zero and scale.

The prominent maximum at 183 Å may have been enhanced by the choice of normalizing wavelength and by Li absorption. Its position corresponds to the maximum density of states in the first Brillouin zone of pure Al. To the high-energy side the shape of the spectrum resembles Matyas' (Tomboulian 1957) theoretical N(E) curve with excision of states of higher energies. If, for the ‘ thick ’ layer of Li, it is assumed that no further change in the Al spectrum will result from increasing the thickness of Li, then by analogy with the case of Li on Mg, no dilution by the spectrum of normal Al from the underlying solid target should be present. Therefore the modified Al spectrum is the result of a combination of (i) structure changes which produce a different N(E) distribution, (ii) depopulation of higher energy states of the first and second zones resulting from electron transfer, and (iii) Li absorption whose undetermined extent makes estimates of the decrease in band width at the low energy side very hazardous.

For Al on Mg a normal Al spectrum produced in the unalloyed outer region of the Al film will dilute that from modified Al. The Al spike has not disappeared as with the thick Li layer and there is no absorption. However, structure changes in the alloyed Al could produce changes in the N(E) curve at lower energies. The choice of 189 Å as the normalizing wavelength then loses its significance.

The edge wavelength and edge width are apparently not changed and no edge shift to 171·8 Å reported by Gale and Trotter (1956) for Mg–Al alloys is present. Nothing can be said about the band width. There is no resemblance in the Al on Mg spectrum to the alloy spectra of Gale and Trotter.

§ 7. Lithium

The K spectrum of Li shows a distinct high energy edge extending to about 75% of the intensity at the maximum (Crisp and Williams 1960). On the low-energy side the shape and width of the band can be seriously affected by development of the Li 'line' whose maximum comes at 253 Å (Fisher *et al.* 1958). After the discovery that the development of the line and the associated fluorescence could be stopped by massive evaporation of Li as a 'getter' this was always done before recording Li spectra. The Li spectra of figs. 3 and 4 and the smoothed curves of fig. 8 are therefore not affected by the Li line.

Figure 8 shows the result of averaging four spectra of pure Li, four spectra of Li on Mg and four spectra of Li on Al. These have been normalized to the same intensity at the maximum and for the first two the edge is taken to extend to 75% of the maximum. Only two spectra of Li under Mg were recorded, neither suitable for analysis, and all that can be said is that for Li under Mg no differences from normal Li have been established.

Figure 3 shows that when Li is deposited on Mg there is a relative increase in intensities on the low-energy side of the spectrum. This accords with the observations of Catterall and Trotter for Li–Mg alloys. There is no observable change in edge wavelength, edge width or energy of the maximum. The latter energy is determined by the contact of the anisotropic Fermi surface with the first zone boundary and that this should be unchanged suggests that emission from the overlying b.c.c. Li is observed as well as that from the Li presumably dissolved in the h.c.p. Mg. Catterall and Trotter obtained a similar result for an alloy containing 20·9% atomic Li which presumably is mainly a solution of Li in Mg.

Figures 4 and 8 show that when Li is deposited on Al the Li spectrum is changed very radically. The high-energy edge has disappeared, the maximum has shifted and the band width has increased. The 'edge width' to 75% maximum intensity is now about 1·2 ev, comparable with the 'edge width' shown by non-conductors (Skinner 1940). The maximum has shifted about 0·5 ev to lower energies. The band width, including the tail, is about 8 ev compared with 4·2 ev for pure Li, for which the extrapolated band width is 3·0 ± 0·1 ev (Crisp and Williams 1960). If this spectrum comes from Li atoms at the interface combined with Al as LiAl, the first Brillouin zone of Li could be practically full. A spectrum such as that seen would be expected if the zone was full and an energy gap existed between first and second zones. Any zone overlap would prevent the disappearance of the edge.

Fig. 8

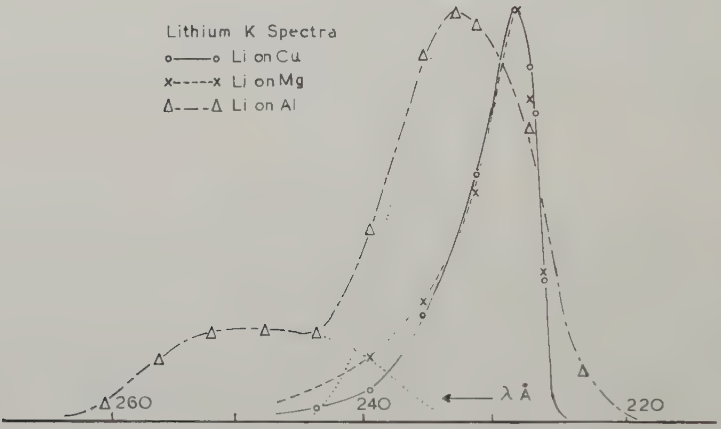

Smoothed averages of four K spectra of pure Li, four spectra of Li on Mg and four spectra of Li on Al. Intensities normalized to make the maxima equal. Dotted curves show a hypothetical separation of the Li on Al into two components, assuming the low-energy bulge is symmetrical about the maximum at 247 Å.

It should be emphasized that the low-energy bulge has nothing to do with the Li 'line'. Its maximum is at 247 Å compared with 253 Å for the 'line'. No fluorescence, which always accompanies the line, was visible on the target when these spectra were obtained. Figure 8 shows a tentative separation of the Li spectrum into two components assuming that the low-energy bulge is symmetrical about its maximum. The low energy component might result from the appearance of excitation states (Parratt 1959) of Li in LiAl. The width of the high energy component is about 5 ev.

§ 8. Discussion

The spectrum changes noted in Li–Mg alloys are seen to a much greater extent with evaporated layers. This is taken as evidence for instantaneous alloying at the interface. Observations made by Catterall and Trotter (1959) on Li–Mg alloys are supported by our results for both alloys and evaporated films. There is no change greater than 5×10^{-2} ev in edge wavelengths, or edge widths. The band width for the constituent of higher valency is lessened, the change showing up on the low-energy side. The band width of the constituent of lower valency is increased, the increase showing on the low-energy side. The exception is the case of Li deposited on Al in which the band shape is radically changed.

Since the Mg L_{23} under Li shows a complete loss of the spike, which is the result of second zone overlap, it is assumed that the depopulation of energy states due to electron transfer has progressed at least as far as the energy at the base of the spike, emptying the second zone entirely and the first zone also to some extent. However, the absence of any measurable change in energy of the edge shows that this emptying of the upper levels has been offset very effectively by changes in the screening of the L levels. The screening compensation is so much more exact than for the case of copper–zinc alloys discussed by Varley (1956), that a close connection between the extent of electron transfer, leading to changes in the population of energy states and the changes in screening of the inner levels, is indicated.

Since the edge has, in effect, moved up, the tail follows, and the energy range over which depopulation has occurred should be estimated from the narrowing of the band at the tail. It will be seen from fig. 6 that this energy range is approximately equal to that from the edge to the foot of the spike. If the structure remains the same the low-energy maximum should shift to higher energies by the same amount. This is not observed. As pointed out above, it is possible that the spectrum of h.c.p. Mg containing dissolved Li is diluted by the spectrum of Mg dissolved in b.c.c. Li for which the maximum is shifted to lower energies by the structure change. The required shift of low-energy maximum is seen in fig. 3 of Catterall and Trotter (1959) but the maximum for their pure Mg occurs at 264 Å compared with 260 ± 1 Å in our fig. 6.

The above considerations cannot apply to the intermetallic Mg_2Sn because it has a fluorite structure and the N(E) curve should be different. However, the increased band width, if real, is seen on the low-energy side as in Li, the edge energy being unchanged.

As regards Li on Mg, there is agreement with the observations of Catterall and Trotter that the intensities increase in the tail while the maximum does not change energy. If shielding is reponsible for there being no change in edge energy, increased population of high-energy states should move the maximum to lower energies and decrease the height of the edge. This has not been observed, either by Catterall and Trotter, for an alloy containing 20·9% atomic Li or by ourselves for Li on Mg. Whilst in our case the Li spectrum from the unalloyed part of the Li film would dilute that from the modified Li, the lack of any change at all in the maximum makes this an inadequate explanation.

The case of Li deposited on Al involves the most drastic change recorded in a soft x-ray spectrum. The energy at half-intensity of the modified Li spectrum is very nearly equal to the edge energy in pure Li, and the shift in maximum is approximately the same as the low-energy increase in band width. This accords with the arguments stated above. However, the shape of the maximum has changed considerably although the structure change from Li to LiAl is slight. If the tails and the maxima of the two spectra are brought into coincidence the pure Li edge approximately bisects the modified Li band. This supports the inference that the complete loss of high energy edge indicates a completely filled first zone with an energy gap above it.

The case of Al is more difficult to interpret. If, as assumed above the evaporation of Li was carried so far that no dilution by the normal Al L_{23} spectrum from the underlying solid is present, the observed Al spectrum results from the three effects previously listed. A structure change from f.c.c. Al to b.c.c. LiAl would produce a modification of the N(E) curve for Al, but its true extent is disguised by Li absorption.

Until the spectrum from bulk LiAl can be observed it is futile to analyse the modified Al spectrum. Dilution from pure Al may be reponsible for the greater prominence of the high energy spike in the Al overlying Mg. However, if this is so the modified Al spectrum must possess a more prominent maximum at 182 Å and the modification of the low-energy region would be more severe than appears in fig. 7.

Acknowledgments

We are indebted to the Armour Research Foundation, Chicago, for the provision of the Li–Mg alloys; to Professor A. G. McLellan of Christchurch, New Zealand, for the loan of a glass grating, and to Dr. W. Baumgartner of E.T.H., Zurich, for assistance in providing specially modified photomultipliers. R.S.C. thanks the Australian Atomic Energy Commission for a Fellowship during the tenure of which this work was done. The continued interest and encouragement of Professor C. J. B. Clews is greatly appreciated.

References

Catterall, J. A., and Trotter, J., 1959, *Phil. Mag.*, **4,** 1164.
Crisp, R. S., 1958 a, *Aust. J. Phys.*, **11,** 449; 1958 b, *J. sci. Instrum.*, **35,** 470.
Crisp, R. S., and Williams, S. E., 1960, *Phil. Mag.*, **5,** 525.
Elmore, W. C., and Sands, M., 1949, *Electronics* (New York : McGraw-Hill), p. 250.
Farineau, J., 1937, *C. R. Acad.*, **205,** 365.
Fisher, P., 1954, *J. opt. Soc. Amer.*, **44,** 665.
Fisher, P., Crisp, R. S., and Williams, S. E., 1958, *Opt. Acta,* **5,** 31.
Fujiki, J., 1959, *J. phys. Soc., Japan*, **14,** 913.
Gale, B., and Trotter, J., 1956, *Phil. Mag.*, **1,** 759.
Michel, P., 1956, Thesis, University of Strasbourg (quoted by Weaver and Hill).
Parratt, L. G., 1959, *Rev. mod. Phys.*, **31,** 616.
Pollard, J., 1953, *Rev. sci. Instrum.*, **24,** 996.
Skinner, H. W. B., 1940, *Phil. Trans*, **239,** 95.
Skinner, H. W. B., and Johnson, J. E., 1937, *Proc. roy. Soc.* A, **161,** 420.
Tomboulian, D. H., 1957, *Handb. Phys.*, **30,** 281 (Berlin : Springer).
Varley, J., 1956, *Nature, Lond.*, **178,** 939.
Weaver, C., and Hill, R. M., 1959, *Advanc. Phys.*, **8,** 375.

Pitting of Aluminium at Grain Boundaries after Ageing†

By G. A. Bassett‡ and C. Edeleanu
Tube Investments Research Laboratories, Hinxton Hall, Essex

[Received June 16, 1960]

Abstract

Thin foils of 99·999% aluminium prepared by electropolishing have been found to develop surface pits along the grain boundaries during ageing at room temperature. It is suggested that the pits are formed by a vacancy mechanism, and that they are associated with the initiation of etch attack along the grain boundaries of aged pure aluminium.

§ 1. Introduction

The localization of etching attack of pure aluminium has been widely associated with the emergence of dislocations (see for example Amelinckx 1953, Lacombe 1947, Lacombe and Beaugard 1948) or with the segregation of impurities to the dislocation lines (Wyon and Crussard 1951, Forty and Frank 1955). In the case of the etching of slip lines on strained aluminium, Bassett and Edeleanu (1960) have advanced an alternative suggestion, that it is the rupture of the natural oxide film and its subsequent failure to repair perfectly, which plays an important part in the initiation of etch attack.

Braun, *et al.* (1958) have found that periods of room temperature ageing are necessary after the preparation of the specimen surface, before grain boundary etching is observed. They have suggested this behaviour is due to diffusion of impurities along the grain boundaries and into the oxide film.

A consideration of the likely residual impurities in high purity aluminium, and the thermodynamics of the replacement of aluminium in the oxide film with these impurities, makes this view difficult to accept. The work described now suggests a possible alternative explanation of grain boundary attack after ageing treatments.

§ 2. Experimental

Specimens of polycrystalline aluminium of 99·999% purity were prepared as foils thin enough for transmission electron microscopy, by electropolishing in a bath of one part perchloric acid to five parts ethyl alcohol. The initial foil was 0·001 in. thick and had a highly polished surface finish. Prior to electropolishing foils were heated to 600°C followed by air cooling. Electron microscope examination was carried out using a Siemens Elmiskop I operated at 80 or 100 kv, specimens being mounted in the stereo holder so that dislocations in the foils could be brought into satisfactory contrast.

---

† Communicated by the Authors.

‡ Present address: Physics Department, University of Bristol.

After thinning, foils were aged, mounted on grids ready for examination in the microscope, in a vacuum desiccator for periods up to four months. Some foils were given an accelerated ageing treatment by maintaining at a temperature of 100°C in an air oven for 24 hours. For comparison with the thin film observations anodic film replicas of the foil surfaces have also been made.

§ 3. RESULTS AND INTERPRETATION

Some typical grain boundaries in a foil aged at room temperature for four months after thinning are shown in fig. 1 (*a*) and (*b*)†, and at a higher magnification in fig. 2. These micrographs reveal the formation of small surface pits along the grain boundaries. This pit formation is quite general, all grain boundaries appearing pitted. The higher magnification micrograph shows one example in which the pits are bounded by well-formed crystallographic faces. For comparison specimens before ageing have been examined and found to have grain boundaries which are completely free of pits of this type.

Accelerating the ageing process by holding a thin foil at 100°C for 12–24 hours it has been possible to photograph in the electron microscope the same grain boundary both before and after ageing. Figures 3 and 4 show such a pair of micrographs in which the appearance of pits at the grain boundary at A and B is clearly seen. A piece of dirt on the left-hand side of the picture forms a convenient point of reference.

The size of pits which have been observed lies between 100 Å and 1000 Å; some tendency for the pits to be larger but fewer in specimens aged at room temperature has been noticed compared with those in which the ageing was accelerated. Figure 5 gives some information of the depth of the pits where an array can be seen at both foil surfaces on an inclined grain boundary. The depth of these pits is about one-fifth of the foil thickness, judged from the interception of the extinction contours in the grain boundary. This figure makes quite evident that the pits are confined to the foil surfaces.

The relative shallowness of the pits has made their detection on oxide replicas uncertain. Although some oxide replicas have shown evidence of the pitting along the boundaries this has not always been seen. Carbon replicas have been tried but in general have failed to detect the pits. An explanation could be that the pits have formed under the natural oxide film and a carbon replica would then not reveal the pits unless the film was completely collapsed.

---

† All figures are shown as plates.

The electron micrograph, fig. 6, is typical of an aged thin foil which has been very lightly etched in $HCl/HNO_3/HF$. The disposition of the holes made in the foil by this treatment strongly suggests that etching started at the grain boundary pits produced on ageing. This type of etching behaviour was confined to aged specimens and was not observed on freshly prepared ones.

§ 4. Discussion

Thin film electron microscope observations have shown that after ageing surface pits form along the grain boundaries in aluminium. Such behaviour can best be interpreted as a migration and aggregation of vacancies at the surface of metal and beneath the natural oxide film. The formation of surface pits on aluminium has previously been reported by Doherty and Davies (1959). In their experiments the pits visible under an optical microscope formed after a small, but critical, drop of temperature, after holding the aluminium specimen at a high temperature. Doherty and Davies interpret their results in terms of the aggregation of the excess vacancies produced by the temperature drop. It is interesting to note that they observe that pits form only in the grains and that near grain boundaries no pits are found; the boundaries acting as very effective sinks for vacancies.

In the present experiments any possible concentration of thermal vacancies quenched in from the heat treatment is too small to account for the pits. It is probable in any case that many quenched-in vacancies are annealed out during electropolishing when a thin foil may reach quite high temperatures. The present pits presumably must also result from segregation of vacancies but it would seem more reasonable that in this case the vacancies migrate across the specimen surface or grain boundary and that metal atoms move away from the region of the pit. The driving force is presumably the large surface energy associated with the T-like junction made by the grain boundary and outer surface and is the same as in thermal etching. The final stable condition in that case would be a trench rather than pits as now found but parametric or crystallographic factors may favour the formation of pits. It is not possible from the present work to say whether the effect is associated with a grain boundary diffusion of vacancies and metal or whether the outer surface is involved, but it seems likely in either case that the film above the voids will be disturbed and it is suggested that this will then favour local etching.

Acknowledgments

We thank Professor F. C. Frank and several laboratory colleagues for helpful comments and discussion, and the Chairman of Tube Investments Ltd. for permission to publish the paper.

References

Amelinckx, S., 1953, *Phil. Mag.*, **44,** 1048.
Bassett, G. A., and Edeleanu, C., 1960, *Phil. Mag.*, **5,** 707.
Braun, I., Frank, E. C., and Meyrick, G., 1958, *Phil. Mag.*, **35,** 1312.
Doherty, P. E., and Davies, R. S., 1959, *Acta. Met.*, **7,** 118.
Forty, A. J., and Frank, F. C., 1955, *J. phys. Soc., Japan*, **10,** 656.
Lacombe, P., 1947, *Strength of Solids*, Report of Bristol Conference (London: Physical Society).
Lacombe, P., and Beaugard, L., 1948, *J. Inst. Met.*, **78,** 7.
Wyon, G., and Crussard, C., 1951, *Rev. Métall.*, **48,** 121.

Etch Pits and Dislocations in Ice Crystals†

By G. W. Bryant and B. J. Mason
Imperial College, London

[Received June 23, 1960]

Abstract

Etching of ice crystals grown from both the vapour and the melt has revealed etch pits in concentrations of up to $10^6/\mathrm{cm}^2$ which apparently mark the sites of emergent dislocations. Silvered Formvar replicas show the etch pits on the basal surface to be hexagonal pyramids on which spiral or closed terraces of steps are often visible. These features are interpreted in terms of the etching of helical dislocations. The etch pits tend to group themselves along low-angle grain boundaries and slip lines. When the crystal is mechanically stressed, etch channels appear on the basal plane along the $\langle 11\bar{2}0 \rangle$ directions which suggests that these are the preferred glide directions.

Double rows of small etch pits radiating from impurity specks and local centres of high stress probably mark the sites of dislocation loops intersecting the surface. Pyramidal hillocks appearing in concentrations of $10^5/\mathrm{cm}^2$ on the basal faces of crystals grown from the vapour may be growth features and not the result of etching.

§ 1. Introduction

Thermal or chemical etching acts by the preferential evaporation or dissolution of the surface at imperfections where molecules are surrounded by fewer nearest neighbours than usual and so are less strongly bound. The shape of an etch pit will depend upon the geometrical arrangement of the molecules in the particular crystal face and upon the relative rates of dissolution in directions parallel and perpendicular to the surface. The geometry of the etch pits may therefore allow the crystal face and the directions of crystallographic axes to be identified.

But much more important, it has recently been demonstrated, by several workers, that etch pits mark the locations of emergent dislocations. This has been most convincingly demonstrated by Jones and Mitchell (1957) who were able to decorate and make visible dislocations in silver-halide crystals by the preferential deposition there of metallic silver, and show that the terminations of dislocations in the crystal surface coincided with the positions of etch pits. Further evidence of this close association was provided by Johnston *et al.* (1957) who were able to match the etch pits appearing on opposite sides of an etched thin slice of a silicon crystal, the inference being that the members of a matched pair were joined by a dislocation line passing through the crystal normal to the surfaces. Furthermore, Johnston and Gilman (1959), during successive stressing and etching of lithium fluoride crystals, observed that successive rows of etch pits formed in the manner expected if they originated on dislocations which moved progressively under the applied stresses.

---

† Communicated by the Authors.

The rather extensive studies of etched crystals, mainly germanium and silicon, have revealed that:

(i) Although it is by no means certain that all emergent dislocations are revealed by the appearance of etch pits (dislocations of large Burgers vector will obviously be favoured), observations of the pits provide useful information on the density and distribution of dislocations.

(ii) Although screw and edge dislocations produce etch pits of similar shape, those associated with screw dislocations are generally smaller, more shallow, and less symmetrical than those associated with dislocations of strong edge character.

(iii) Having revealed the existence of helical dislocations by the decoration of fluorite crystals, Amelinckx, Bontinck and Dekeyser (1957) have suggested that etching of such dislocations may explain the occasional appearance of spiral pits on germanium and silicon.

(iv) Etch pits tend to group themsleves along slip lines and low-angle grain boundaries. The presence of etch pits not only reveals these features but a detailed study of the distribution, density, asymmetry and depth of the pits enables one to deduce the angle between grain boundaries and the directions of slip for both edge and screw dislocations.

Because a study of etch-pit formation appeared to offer a simple and powerful method of studying the dislocation structure of crystals, we decided to exploit it in our studies of ice crystals where dislocations have not been revealed by the appearance of spiral terraces of growth steps nor by attempts to decorate them.

The appearance of etch pits on the surfaces of ice crystals was first reported by Truby (1955). Hexagonal pyramidal features of base diameter $\frac{1}{2}$–20 μ and depth $\frac{1}{4}$–$\frac{1}{2}$ μ were observed and sometimes exhibited a stepped-layer structure concentric with the c axis. Higuchi (1958) and Muguruma and Higuchi (1959) discovered that etch pits could be produced on the surfaces of ice and snow crystals by etching with a Formvar solution. Hexagonal pits appeared on the basal surface of a snow crystal in concentrations of up to $10^5/\text{cm}^2$. After prolonged etching the bottom surfaces of the pits revealed the layer-type structure noted by Truby, the height of individual steps varying between 3 and 16 μ. These Japanese authors have used the etch pits to determine the size distribution of, and orientation of the crystal axes in, individual grains of polycrystalline ice.

The object of the present investigation was to make a more detailed study of etch pits on ice crystals and to relate them to the dislocation structure.

§ 2. Etching Technique

Surfaces of ice crystals, grown from both the vapour and the melt, were etched with a 1% solution of polyvinyl formal (Formvar) in ethylene dichloride. A small quantity of the solution was poured onto the ice surface and the solvent allowed to evaporate and leave a thin, transparent, plastic film on the surface which could be peeled off and examined as a replica. Etching occurred because traces of water in the ethylene dichloride froze to produce filamentary ice crystals which subsequently evaporated to leave small holes in the Formvar film. Etching, by evaporation, then proceeded beneath these holes to produce wide, shallow pits on the ice surface. Smaller, pyramidal etch pits subsequently appeared inside these large pits as shown in fig. 1†. Subsequent applications of the Formvar solution gave rise, in similar manner, to further large pits which merged with earlier ones so that, eventually, the whole surface became etched. The etch pits could be studied at any stage by peeling off the plastic film with a piece of transparent adhesive tape, fixing it face upwards on a microscope slide and viewing it under the microscope in transmitted light. To obtain better contrast and resolution a thin layer of silver was evaporated onto the replica which, when viewed in reflected light with magnifications of × 400, revealed the detailed structure of the etch pits as shown in figs. 4 and 6.

§ 3. Etch Pits on Ice Crystals Grown from the Melt

A rectangular metal channel was filled with distilled water and cooled slowly below 0°c in a cold room to produce a block of ice whose flat surfaces contained ice crystals of various orientations which could be identified by the shapes of the large etch pits. The ice block was placed in a refrigerator held at -20°c, its surface polished with fine emery paper followed by a silk cloth and plastic replicas of its surface taken at intervals of 24 hours.

The first replica showed only the fine scratches produced during polishing but the second replica, taken 24 hours later, showed a flat surface covered by wide, shallow etch pits about $100\,\mu$ across with a surface density of about 10^3/cm^2. Etch pits appeared on all the exposed crystal faces, their shapes revealing the crystalline symmetry and the orientation of the face. Figure 2 shows shallow hexagonal pits on the basal surface, each about $100\,\mu$ in diameter, viewed in transmitted light.

The replica in fig. 1 shows many small pyramidal etch pits (seen inverted), 5 to $10\,\mu$ in diameter, formed inside a large, shallow pit on a basal surface. The smaller pits, appearing in concentrations of up to 10^5/cm^2, were hexagonal in cross section with their sides usually parallel, but occasionally perpendicular, to the sides of the large pit. The heights of the pyramids were roughly equal to the diameters of their bases. Under vertical illumination the sides of the smaller pits appeared smooth but, when illuminated at a slight angle to the vertical, they appeared to be built up of several concentric steps each a few tenths of a micron in height. On many of the larger pyramids ($d > 10\,\mu$), these were accompanied by one, and sometimes two, large concentric steps of height up to $1\,\mu$. A few per cent of these pits exhibited hexagonal spirals of similar step height—see fig. 3.

---

† All figures are shown as plates.

On some of the later replicas from completely etched surfaces, areas of basal surfaces were crossed by lines of hexagonal pyramidal pits forming etched channels. A silvered replica showing an (inverted) line of pyramidal pits is shown in fig. 4. These were formed at a grain boundary, the average-spacing of the pits divided into the intermolecular distance giving 30″ for the angle of misorientation.

Ice crystals were also grown from the melt by slowly cooling a wide shallow dish of water in such a manner that freezing started at the surface to produce large, flat, single crystals. These were removed with tweezers, frozen to a microscope slide, and examined by transmitted light under a microscope in a cold room held at $-8°$c. Etching of the surface with successive applications of Formvar solution was carried out as before but now evaporation proceeded much more rapidly and the etch pits on the basal surface, both large and small, tended to be circular rather than hexagonal. However, concentric rings about $1\,\mu$ in height and occasional spirals with one or two turns were still observed although smaller steps were now not visible.

In an attempt to study the effect of the inclusion of small, insoluble, foreign particles in the ice, the shallow dish of water was allowed to collect dust for a few days. Ice crystals were then formed on the surface as before and silvered replicas of their basal surfaces, taken at 30 min intervals, now revealed many patterns similar to those shown in fig. 5. Radiating from a small pyramidal etch pit are six double etch channels which, having obtained a length of about $10\,\mu$, broaden to about double their original width and finally terminate in either another pyramidal etch pit or in the side of the large, shallow pit which contains them all. Broadening of the channel is sometimes accompanied by a change in direction of about 30°.

§ 4. SURFACE STRUCTURE OF CRYSTALS GROWN FROM THE VAPOUR

Single ice crystals were grown from the vapour, under carefully controlled conditions of temperature and supersaturation, in the diffusion cloud chamber described by Hallett and Mason (1958). The crystals were grown on a fine nylon fibre hanging vertically down the centre of the chamber; the crystal habit varied along the length of the fibre from hexagonal plates→needles→prismatic columns→plates→dendrites→plates →prisms as the temperature varied from 0°c to $-50°$c. Hexagonal plates of up to 5 mm diameter, needles up to 2 cm long × 2 mm wide, and dendrites 3 cm × 1 cm were grown in this way and transferred to the cold room for etching and surface examination by the techniques described above.

Replicas of previously unetched basal faces of plate-like crystals revealed, instead of etch pits, raised hexagonal pyramids, usually less than 10 μ in diameter. Under high magnification these exhibited concentric rings and spirals similar to those observed in etch pits. These hillocks, shown in fig. 6, were eroded by subsequent etching. They were accompanied by numerous smaller, circular imperfections too shallow to be definitely identified as either hills or depressions. Their surface density is about $10^5/\text{cm}^2$.

Replicas of previously unetched prism faces showed a high density, about $10^6/\text{cm}^2$, of features which were rectangular, aligned parallel to the c axis, and had four sloping walls—see fig. 7. Again they were so shallow that it was difficult to determine whether they were hills or depressions.

Etching with Formvar solution produced hexagonal etch pits on the basal surfaces of plate-like ice crystals in concentrations of order $10^4/\text{cm}^2$, the edges of the pits being parallel to the crystallographic $\langle 11\bar{2}0 \rangle$ directions—see fig. 8. Pits formed on the prism $(10\bar{1}0)$ faces of ice needles were rectangular in cross-section and mostly flat at the bottom as shown in fig. 9. Star-shaped etch channels were seen only very rarely in crystals grown from the vapour in virtually dust-free conditions; one such is shown in fig. 10. The channels run parallel to the $\langle 11\bar{2}0 \rangle$ axes of the crystal and are marked all along their length by very small pits less than 1 μ in diameter.

In an attempt to correlate the positions of etch pits arising on opposite sides of a plate crystal, about 100 μ thick, the crystal was suspended from a glass fibre and coated on both sides with Formvar solution. The plastic film was then removed by folding transparent adhesive tape round the crystal, peeling it off, and straightening the tape to obtain replicas of both faces side by side. Although both basal faces showed approximately the same density of etch pits, it was not possible to match their positions. This suggests that, if the pits were formed by the etching of dislocations, the latter followed rather devious paths in traversing the 100 μ thickness of crystal.

§ 5. THE MOVEMENT OF DISLOCATIONS UNDER MECHANICAL STRESS

Replicas of the surfaces of thin sheets of ice, 1–2 mm in thickness, produced by the freezing of water in a refrigerator, revealed large concentrations ($\sim 10^5/\text{cm}^2$) of etch channels oriented along the $\langle 11\bar{2}0 \rangle$ directions as shown in fig. 11. The specimens were subjected, at -20°c, to quite strong vibrations from the compressor of the refrigerator; when similar specimens were mounted on foam rubber, so that the vibrations were greatly damped, the number of etch channels was greatly reduced. We believe that the channels, which were tapered along their length, resulted from the movement of edge dislocations under mechanical stresses induced by the vibrations. During a period of 20 min the etch pit advanced about 15 μ during which time the specimen was subjected to about 30 000 vibrations.

The average movement per vibration was therefore about 5 Å, or about one inter-molecular spacing along the $\langle 11\bar{2}0 \rangle$ direction!

Similar sheets of ice were subjected, again at −20°c, to local stresses by dropping lead shot onto the surface from heights of a few inches. The replicas now revealed rosettes of the type shown in fig. 12 and noted earlier by Gilman and Johnston (1957) on the surfaces of lithium fluoride crystals. Arrays of etch channels, presumably associated with similar arrays of dislocations, radiated from large etch pits along the $\langle 11\bar{2}0 \rangle$ directions which again appear to be preferred glide directions.

§ 6. Discussion

The fact that the surface densities of the smaller etch pits on ice lie in the range 10^5 to $10^6/\text{cm}^2$ and are comparable to the observed densities of dislocations in other materials, suggests that they probably arose by the etching of emergent dislocations. A close association between dislocations and etch pits is also suggested by the latter tending to group preferentially along grain boundaries and slip lines.

The inverted pyramidal shape of the pits on the basal plane may be interpreted in terms of a dislocation being etched at similar rates in directions normal and parallel to the surface, the dislocation following a line drawn from the apex of the pyramid to the centre of the base. Anisotropic lateral etching on the prism faces is revealed by the rectangular shape of the pits.

In the present work it was usually not possible to determine whether the pits were generated about edge or screw dislocations but etching patterns sometimes appeared which indicated the presence of helical dislocations. These were first discovered by Bontinck and Amelinckx (1957), their formation being explained by Amelinckx, Bontinck, Dekeyser and Seitz (1957) who suggested that the condensation of vacancies on to a dislocation possessing a strong screw component could cause it to climb into a helix. Etching of such a dislocation, which may be regarded as an unwinding of the screw component, would then produce a pit in the form of a helical cone. Amelinckx, Bontinck and Dekeyser (1957) further demonstrate that bunching of the unwinding monolayers, caused by the rotation of the centre of etching along the helix, could form visible spiral steps whose spacing would be equal to the pitch of the helix and, in consequence, bear no direct relation to the Burgers vector of the underlying dislocation. This mechanism may well explain the appearance of the spiral steps in fig. 3, the height of which were of order 1 μ, and therefore comparable to the pitch of helical dislocations observed directly in other crystals.

It is also known that two parallel helices of opposite sign may combine to produce a row of closed loops and should this emerge from the etched surface at a slight angle to the vertical, it could give rise to etch pits consisting of a series of closed terraces as shown in fig. 6.

The double rows of symmetrical etch pits seen in fig. 10 may have originated on helical dislocations with axes parallel to the surface. In this and similar cases they may have been initiated by a dust particle in much the same way as Jones and Mitchell (1958) were able to generate helical dislocations and rows of prismatic loops by pressing small glass spheres into crystals of silver chloride.

Our attempts to reveal the three-dimensional structure of dislocations in ice, by adding to the water small quantities of silver nitrate in the hope that the silver ions might migrate preferentially to the dislocations line during the freezing process, have been unsuccessful.

The pyramidal hillocks, which appeared in concentrations of between 10^3 and $10^5/\mathrm{cm}^2$ on the basal surfaces of crystals grown from the vapour in very clean conditions, were not observed on crystals grown from the melt. Although they may have been formed by etching during the preparation of the first replica, the fact that they were eroded and finally removed by subsequent etching leads us to think that they may have been formed by growth rather than by dissolution at preferred sites on the crystal surface. This point is not easy to check but is being investigated further.

The fact that dislocations spreading out from localized regions of high stress and etch pits moving under applied stresses show a very strong tendency to follow the $\langle 11\bar{2}0 \rangle$ directions suggests that these are preferred glide directions.

References

Amelinckx, S., Bontinck, W., and Dekeyser, W., 1957, *Phil. Mag.*, **2,** 1264.

Amelinckx, S., Bontinck, W., Dekeyser, W., and Seitz, F., 1957, *Phil. Mag.*, **2,** 355.

Bontinck, W., and Amelinckx, S., 1957, *Phil. Mag.*, **2,** 94.

Gilman, J. J., and Johnston, W. G., 1957, *Dislocations and Mechanical Properties of Crystals* (New York : Wiley), p. 116.

Hallett, J., and Mason, B. J., 1958, *Proc. roy. Soc.* A, **247,** 440.

Higuchi, K., 1958, *Chamonix Symposium Int. Ass. Sci. Hydrol. Pub.*, No. 47, p. 249.

Johnston, W. G., and Gilman, J. J., 1959, *J. appl. Phys.*, **30,** 129.

Johnston, W. G., Li, C. H., and Knudsen, C. I., 1957, *J. appl. Phys.*, **28,** 746.

Jones, D. A., and Mitchell, J. W., 1957, *Phil. Mag.*, **2,** 1047; 1958, *Ibid.*, **3,** 1.

Muguruma, J., and Higuchi, K., 1959, *J. met. Soc., Japan*, **37,** 71.

Truby, F. R., 1955, *J. appl. Phys.*, **26,** 1416.

Measurement of the Debye–Waller Temperature Factor for Silver and α-iron†

By C. W. Haworth

Department of Metallurgy, Sheffield University; formerly Department of Metallurgy, Oxford University

[Received June 23, 1960]

Abstract

Measurements have been made of the variations with temperature of the intensities of x-ray diffraction lines from silver and iron. For silver the measurements were in the range 286–1100°K, and the Debye–Waller temperature factor corresponded to a characteristic temperature of 197°K at 286°K. For iron the measurements covered the range 286–1190°K, and corresponded to $\Theta = 389$°K, although there was a large scatter in the results due to crystal changes brought about by annealing. The intensity measurements showed no discontinuity at the Curie temperature, nor was there any anomaly in the spacing of the (110) planes.

§ 1. Introduction

The variations with temperature of the integrated intensity and peak height of x-ray diffraction lines 331, 551/333 and 422 for a silver powder specimen and 220 for an iron specimen, were measured at high temperatures. For silver an explicit volume dependence of the characteristic temperature was adequate to give the observed temperature dependence in terms of the Debye–Waller theory, the value $\Theta = 197$°K being obtained at room temperature. This result does not agree with the work of Andriessen whose results give $\Theta = 239$°K when recalculated to allow for lattice expansion, nor with the work of Boskovits *et al.* (1958) who obtained a large deviation from the theoretical intensity variation above 700°K. The present work does agree approximately with that of Spreadborough and Christian (1959 b).

The results for iron showed a much larger scatter than silver, associated with crystal changes brought about by prolonged annealing. No anomaly was observed at the Curie temperature, either in the intensity variations or in the spacing of the 110 planes.

§ 2. Theory

For the Debye–Waller theory, the temperature dependence of the intensity of an x-ray reflection is given by the factor $\exp(-2M)$ (following James 1954, 5.67), where

$$M = \frac{6h^2T}{mk{\Theta_M}^2}\,\frac{\sin^2\theta}{\lambda^2}\cdot\left\{\phi(x)+\frac{x}{4}\right\}. \qquad (1)$$

---

† Communicated by the Author.

The characteristic temperature Θ_M has been regarded as a constant in the above expression: amongst other things this is equivalent to assuming that the volume of the crystal remains constant as the temperature changes. Paskin (1957) has given a thermo-dynamical derivation of the variation of Θ_M (regarded as a temperature dependent parameter $\Theta(T)$) with volume, the relation for an isotropic crystal which obeys Gruneisen's expansion equation being written

$$\frac{\Theta(T)}{\Theta(T_0)}=\left(\frac{a_{T_0}}{a_T}\right)^{3\gamma} \quad . \quad . \quad . \quad . \quad . \quad . \quad . \quad . \quad . \quad . \quad (2)$$

where a_T is the lattice parameter at temperature T°K. The Gruneisen constant γ (following Hume-Rothery 1945) is calculated from the equation

$$\gamma=\frac{V\beta}{C_V k}$$

V being the atomic volume, C_V the atomic specific heat at constant value, β the volume coefficient of expansion and k the compressibility. The values used for the constant γ are 2·40 for silver and 1·6 for iron.

Substituting for $\Theta_M{}^2$ in eqn. (1) we have

$$M=\frac{6h^2T}{mk\,\Theta_{T_0}{}^2}\,\frac{\sin^2\theta}{\lambda^2}\,\Phi\{x\}T' \quad . \quad . \quad . \quad . \quad . \quad . \quad . \quad (3)$$

where $T'=T(a_T/a_{T_0})^{6\gamma}$ the 'adjusted' temperature allowing for the effect of lattice expansion, and

$$\Phi\{x\}=\{\phi(x)+x/4\}$$

is approximately unity and is tabulated by James (1954).

Neglecting the small effect due to change of Bragg angle θ with temperature, the intensity ρ_T of a given reflection at temperature T can be compared with the intensity at a temperature T_0, the relation being

$$\ln\left(\frac{\rho_T}{\rho_{T_0}}\right)=-\frac{12h^2}{mk\,\Theta_{T_0}{}^2}\,\frac{\sin^2\theta}{\lambda^2}\,\Phi\{x_0\}\left[\frac{\Phi\{x\}}{\Phi\{x_0\}}\,T'-T_0{}'\right]. \quad . \quad . \quad (4)$$

Thus a linear relation is expected between the parameter

$$Y=\frac{\lambda^2}{\sin^2\theta}\ln\left(\frac{\rho_T}{\rho_{T_0}}\right)$$

and the variable $T''=(\Phi\{x\}/\Phi\{x_0\}T'$. A very approximate value of Θ_{T_0} is satisfactory for calculating values of $\Phi\{x\}$, since this function is nearly unity for all values of x corresponding to temperatures above Φ_{T_0}. Any departure from a linear relation can be attributed to an additional dependence of Θ_M on temperature, above that related to the coefficient of expansion. From the slope of a linear relation a value of Θ_{T_0} can be obtained.

§ 3. Experimental Measurements and Results

3.1. *Silver*

Filings were prepared from pure (99·99%) silver, carefully cleaned and that portion which passed through a 350 mesh sieve prepared into a flat diffractometer specimen, held in a molybdenum trough.

This was mounted in a furnace built onto a Norelco diffractometer, described by Spreadborough and Christian (1959 a), and the specimen was annealed at 1020°K for ten hours *in vacuo*. It was found that subsequent annealing treatments at temperatures up to 870°K did not alter the room temperature line profiles of the 331, 422 or 511/333 reflections obtained using CuKα or MoKα radiation.

The integrated intensity for a given reflection obtained for a specimen temperature T_0 could then be compared with that obtained for a higher temperature T, using a planimeter to measure the total area under the $\alpha_1\alpha_2$ profile, above the background level in the immediate neighbourhood of the reflection. From these measurements values of Y corresponding to different temperatures could be obtained.

The background intensity in the neighbourhood of the line was observed to increase with increasing temperature of the specimen, but the variation of intensity with angle in the 'wings' of the Bragg peak was small. However, no attempt was made to obtain an absolute value for the Bragg scattering, but the variation with temperature of the intensity, measured over a small fixed angular range, was found.

The error due to including temperature diffuse scattering in the measurement of the integrated intensity has been discussed by Chipman and Paskin (1959), who showed that the error introduced by including all the wings of the lines (a procedure described by Renninger (1952)) would lead to a larger value of the characteristic temperature than the true one. However, if the temperature diffuse scattering over the small angular range measured is calculated, then the error in characteristic temperature caused by including all the temperature diffuse scattering in the measurements is less than 1% for any of the Bragg reflections used. For the experiments where the peak heights were compared, the error could be larger. The correct adjustment of the apparatus and the validity of background level was checked by observing the 2 : 1 intensity ratio of the $\alpha_1\alpha_2$ doublet lines.

Values of Y could also be calculated from variation in peak heights with temperature. The comparison between measurements based on integrated intensity values and on peak heights was made because:

(*a*) The theoretical calculations refer to the integrated values.

(*b*) Peak height measurements can be made more accurately than a complete profile, because small fluctuations in temperature ($\sim \pm 2$°C) during the profile measurements cause change of Bragg angle which result in serious errors. Provided surface effects in the specimen did not produce asymmetry in an X-ray line, then instrumental effects are unlikely to introduce errors when comparing peak heights instead of integrated intensities. However, it was found that changes in crystalline arrangement introduced by annealing treatments produced greater changes in peak heights than in integrated intensities, and great care was necessary in making use of the peak height data. After repeated annealing at 1220°K the measurements were successfully extended up to 1100°K.

The graph of Y against the adjusted temperature T'' is shown in fig. 1, and is seen to be linear up to a specimen temperature of 1100°K, the highest temperature reached. The slope of the linear relation corresponds to a characteristic temperature of 197°K ± 6 at 286°K, whilst the usually accepted specific heat value is 210°K (James 1954). Other X-ray values for the characteristic temperature of silver, taken from the literature, but re-calculated using the method of analysis used in this paper, are:

Andriessen (1935) $\Theta_M = 239°\text{K} \pm 5$,
Boskovits *et al.* (1958) $\Theta_M = 188°\text{K} \pm 12$,

using only data for temperatures above 290°K, and

Spreadborough and Christian (1959 b) $\Theta_M = 191°\text{K} \pm 8$.

Fig. 1

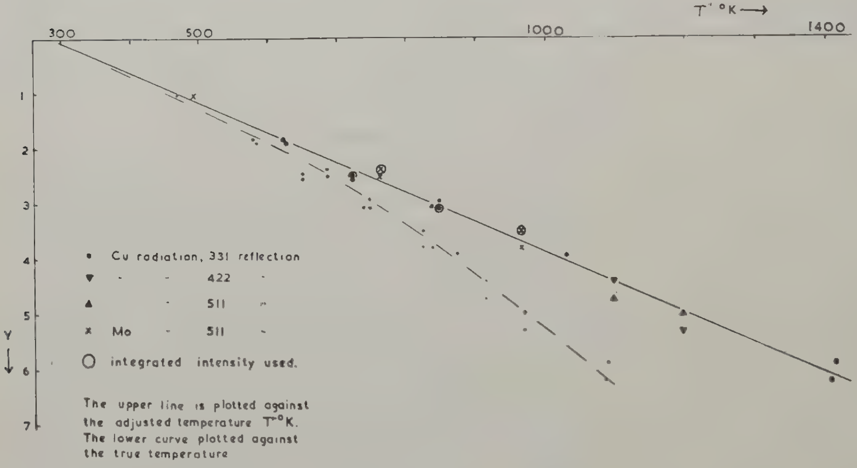

Of these results that of Andriessen gives a nearly linear relation up to 880°K, but the characteristic temperature obtained is much higher than expected. The work of Boskovits *et al.* gives an approximately linear relation from 290°K to 680°K, the slope of the relation agreeing with the present work to within the experimental error. Above 680°K, however, measurements at 780°K showed a more rapid diminution of X-ray intensity than expected, but such a derivation from linearity is not supported by the present work.

The method of correcting for the background used in the present work would tend to give too high a value for Θ_M. The value of the characteristic temperature used in X-ray measurements is expected to be larger than that used in the Debye specific heat theory, owing to different methods of averaging the velocities of longitudinal and transverse elastic waves in the crystal: in the case of silver we expect the X-ray characteristic temperature to be 4% greater than that used in specific heat measurements, from the work of Zener and Bilinsky (1936). The observed characteristic temperature pertaining to the X-ray temperature factor is, however, lower than the specific heat value.

3.2. *Iron*

Two iron specimens were prepared and used: one from Johnson Matthey iron sponge having an analysis 0·0053% Ni, 0·0003% Mn, 0·063% insoluble, and the other by filing B.I.S.R.A. H-iron under cold paraffin. In both cases the powders were carefully cleaned and then passed through a 350 mesh sieve before preparing into a specimen by pressing into a pure iron trough. The second specimen was vacuum-annealed for four hours at 1400°C before placing in the X-ray camera.

Using filtered iron radiation, the 220 reflection at approximately 145° 2θ, was measured. The integrated intensities at different temperatures were compared, the measurements being taken from the trace on an automatic recorder chart, corrected for counter dead-time losses. The results showed a larger scatter than in the case of silver, and a large number of chart recordings were used.

Fig. 2

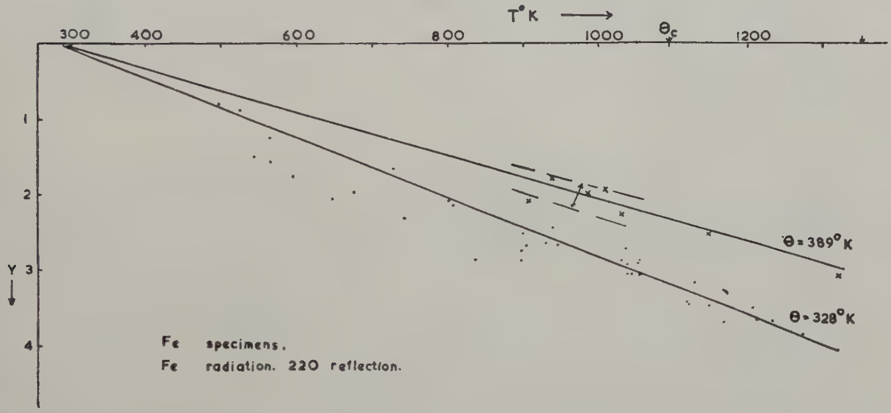

A graph of parameter Y against 'adjusted' temperature T'' was plotted, as in the case of silver, the adjustments to the temperature scale being made using the lattice parameter values of Basinski *et al.* (1955) $\gamma = 1{\cdot}60$ and $\Theta = 430$°K. The value of the characteristic temperature obtained from this graph would depend only to the second order upon the Θ value used in making the temperature adjustment.

The scatter of the results, as presented on this graph is seen to be much larger than in the case of silver, but does show that there is no marked anomaly in the temperature factor at the Curie temperature. This large scatter could have been due to statistical changes in the distribution of reflecting particles, but there was also a time-dependent, partly reversible effect, superimposed on the random variations. This is shown by the measurements represented by crosses on the graph, which were made immediately after heating to a higher temperature, whilst the other points correspond to measurements made after an annealing period of one hour or longer. This effect may be due to extinction variations brought about by polygonization or other changes in the iron crystals.

Fitting a straight line passing through $T_0 = 286°\text{K}$ to these results, and using the same analysis as for silver gives a Θ_M value for the points represented by crosses of 389°K ± 17, and for the other points $\Theta_M = 328°\text{K} \pm 20$. The largest characteristic temperature which can be fitted to any measurement is 403°K, whilst the accepted specific heat value for α-iron is 430°K. It would seem likely that the discrepancy may be associated with changes in extinction brought about by annealing. As in the case of silver, inclusion of temperature diffuse scattering in the measurements would lead to too high a value of Θ_M; although the error due to including all the diffuse scattering, calculated following Chipman and Paskin (but for a b.c.c. lattice) over the range measured of 1·6° 2θ, would lead to an error in Θ_M of less than 0·3%.

The variation in Bragg angle of the α_1 and α_2 peaks with temperature gave a measure of the thermal expansion of the 110 direction in the iron crystal, with a sensitivity of ±0·0002 kx in d value. No anomaly in thermal expansion was observed at the Curie temperature, in agreement with the work of Basinki *et al.* (1955), who used an extrapolation technique such that their lattice parameter results were effectively based upon a study of the 310 direction.

ACKNOWLEDGMENT

This work was carried out while the author held a research grant in the Department of Metallurgy, The University of Oxford. The author would like to thank Professor W. Hume-Rothery for his advice and encouragement.

REFERENCES

ANDRIESSEN, R., 1935, *Physica*, **2,** 417.
BASINSKI, Z. S., HUME-ROTHERY, W., and SUTTON, A. L., 1955, *Proc. roy. Soc.* A, **229,** 459.
BOSKOVITS, J., ROILOS, M., THEODOSSIOU, A., and ALEXOPOULOS, K., 1958, *Acta Cryst.*, **11,** 845.
CHIPMAN, D. R., and PASKIN, A., 1959, *J. appl. Phys.*, **30,** 1992.
HUME-ROTHERY, W., 1945, *Proc. phys. Soc. Lond.* A, **57,** 209.
JAMES, R. W., 1954, *Optical Principles of X-ray Diffraction* (London : Bell).
PASKIN, A., 1957, *Acta Cryst.*, **10,** 667.
RENNINGER, M., 1952, *Acta Cryst.*, **5,** 711.
SPREADBOROUGH, J., and CHRISTIAN, J. W., 1959 a, *J. sci. Instrum.*, **36,** 116 ; 1959 b, *Proc. phys. Soc. Lond.*, **74,** 609.
ZENER, C., and BILINSKY, S., 1936, *Phys. Rev.*, **50,** 101.

The Effect of Lattice Distortion Around Point Defects on the Scattering of Long Wavelength Neutrons†

By D. G. Martin

Metallurgy Division, Atomic Energy Research Establishment, Harwell, Berks

[Received May 13, 1960]

Abstract

In a crystalline element the scattering of long wavelength neutrons by a point defect and an atom are known to be identical. However, when lattice distortion around the point defect is also considered, this is no longer true; in particular the scattering of a point defect is now anisotropic and varies with wavelength. An expression for the cross section of a defect in a relaxed lattice has been derived and applied to f.c.c. and b.c.c. lattices, and in greater detail to copper and molybdenum where the magnitude of the relaxation around defects is known. It has been found that the scattering cross section is appreciably altered by the relaxation of the surrounding atoms, and in particular from those that are nearest neighbours to the defect. A neglect of this relaxation in the interpretation of a neutron scattering experiment could lead to an error of an order of magnitude in an estimate of the number of defects. Also a study of the variation in cross section with wavelength or scattering angle, which is analogous to an x-ray small angle scattering experiment, is incapable of determining uniquely the size of defect agglomerates in solids. However, under favourable circumstances, such experiments could become a useful technique for estimating the lattice distortion around defects.

§ 1. Introduction

Many experiments on solids irradiated by energetic particles have aimed at estimating the numbers and states of agglomeration of the resulting point defects. However, a unique description from experiments observing changes in physical properties has proved very difficult; probably the most unequivocal have been observations under the electron microscope, but unfortunately they are limited to agglomerates larger than about 15 Å.

The scattering of long wavelength neutrons, for which Bragg reflections are absent, is a particularly attractive tool for studying smaller agglomerates and elementary point defects in crystalline solids, because the scattering cross section per point defect is the experimentally known bound atom coherent scattering cross section. Experimentally the main difficulty in the past has been the low flux of long wavelength neutrons available from a reactor; this technique is likely to be exploited more, however, as cooled moderators (Butterworth *et al.* 1957) inside high flux reactors become available as neutron sources.

Initial experiments by Antal *et al.* (1955) were on neutron irradiated graphite. Their estimate of the defect concentration was in good agreement with theoretical predictions. They pointed out, however, that it may be in error for three reasons: (*a*) irradiation may alter the inelastic scattering cross section of the solid, (*b*) defects may be aggregated in pairs or larger defects, (*c*) there may be relaxation of atoms in the neighbourhood of the defect. Changes in the inelastic scattering cross section have been considered negligible because of the small change in Debye temperature after irradiation. Antal and Goland (1958) have discussed the effect of defect pairs on the wavelength dependence of the transmission cross section; they were able to determine the separation of defect pairs in neutron irradiated α–Al_2O_3, although the complexity of the material was an additional difficulty in the interpretation.

---

† Communicated by the Author.

We propose to discuss here the third possible source of error, namely the effect of lattice relaxation about the defect on the scattering cross section. Unfortunately the magnitude of this relaxation is uncertain in those materials that have been studied experimentally. However, it is, known approximately in certain metals, and for two of these, copper and molybdenum, the cross sections are calculated in this paper to illustrate the general principles.

§ 2. THEORY

Let us consider a perfect lattice of N atoms per unit volume to which ν atoms have been introduced randomly on interstitial sites, causing relaxation of μ atoms around each interstitial. We note here that the ensuing treatment is identical for ν vacancies.

The scattering amplitude per unit solid angle for unit incident flux

$$=b\left\{\sum_{p=1}^{N}\exp(-i\boldsymbol{\varkappa}\,.\,\boldsymbol{\rho}_p)+\sum_{q=1}^{\nu}\sum_{r=0}^{\mu}\exp[-i\boldsymbol{\varkappa}\,.\,(\boldsymbol{\xi}_q+\boldsymbol{\psi}_r)]\right.$$
$$\left.-\sum_{q=1}^{\nu}\sum_{s=1}^{\mu}\exp[-i\boldsymbol{\varkappa}\,.\,(\boldsymbol{\xi}_q+\boldsymbol{\varphi}_s)]\right\} \quad . \quad . \quad . \quad . \quad (1)$$

$$\equiv b[A+B-C] \quad . \quad . \quad . \quad . \quad . \quad . \quad . \quad . \quad (1a)$$

where b is the bound atom scattering amplitude per unit solid angle for unit incident flux, $\boldsymbol{\varkappa}$ is the scattering vector, magnitude $(4\pi\sin\theta)/\lambda$ (2θ=scattering angle, λ=neutron wavelength), $\boldsymbol{\rho}_p$ and $\boldsymbol{\xi}_q$ are vector distances from the origin of atoms in lattice and interstitial sites respectively, $\boldsymbol{\psi}_r$ is the vector distance of a relaxed atom from its neighbouring interstitial and $\boldsymbol{\varphi}_s$ is the corresponding distance of a lattice site vacated due to relaxation. The sum over p is for the perfect, unrelaxed lattice; that over r includes a term with $\boldsymbol{\psi}=0$, which corresponds to the contribution made by the interstitials to the scattering amplitude.

The scattering intensity is

$$b^2[AA^*+A(B^*-C^*)+A^*(B-C)+BB^*+CC^*-BC^*-CB^*]. \qquad (2)$$

Beyond the Bragg cut off wavelength

$$AA^*\sim 1,$$
$$A(B^*-C^*)+A^*(B-C)\sim\nu^{1/2},$$

and turn out to be negligible compared with the other terms, which may be expressed thus:

$$b^2 \sum_{q,q'=1}^{\nu} \exp\left[-i\boldsymbol{\kappa}\,.\,(\boldsymbol{\xi}_q-\boldsymbol{\xi}_{q'})\right] \left\{ \sum_{r,r'=0}^{\mu} \exp\left[-i\boldsymbol{\kappa}\,.\,(\boldsymbol{\psi}_r-\boldsymbol{\psi}_{r'})\right] + \sum_{s,s'=1}^{\mu} \exp\left[-i\boldsymbol{\kappa}\,.\,(\boldsymbol{\varphi}_s-\boldsymbol{\varphi}_{s'})\right] - \sum_{r=0,\,s=1}^{\mu} \exp\left[-i\boldsymbol{\kappa}\,.\,(\boldsymbol{\psi}_r-\boldsymbol{\varphi}_s)\right] - \sum_{r=0,\,s=1}^{\mu} \exp\left[-i\boldsymbol{\kappa}\,.\,(\boldsymbol{\varphi}_s-\boldsymbol{\psi}_r)\right] \right\} . \quad . \quad . \quad . \quad (3)$$

The sum outside the brackets is of ν^2 vectors of random phase, apart from the restriction that $\boldsymbol{\xi}_q$, $\boldsymbol{\xi}_{q'}$ must lie on interstitial sites; it may be shown to equal $[\nu(N-\nu)]/N$. Hence in most practical cases, when ν is less than a few per cent of N, the sum equals ν to a good approximation, which is the value for a perfectly random array of ν interstitials.

The four series in brackets, which consist of three sums of the general type $\cos\left[\boldsymbol{\kappa}\,.\,(\mathbf{x}-\mathbf{y})\right]$, are correct for a single crystal, when the orientation of the relaxed zone about each interstitial is identical. For polycrystalline material we must average over all orientations of $(\mathbf{x}-\mathbf{y})$, resulting in a series of terms of the type

$$\frac{\sin\left[|\boldsymbol{\kappa}|\,.\,|\mathbf{x}-\mathbf{y}|\right]}{|\boldsymbol{\kappa}|\,.\,|\mathbf{x}-\mathbf{y}|} .$$

Hence the scattering intensity per unit incident flux, per unit solid angle, which is the differential scattering cross section is

$$\sigma_d = b^2\nu \left[\sum_{r,r'=0}^{\mu} \frac{\sin\left(\dfrac{4\pi\sin\theta}{\lambda}\,|\boldsymbol{\psi}_r-\boldsymbol{\psi}_{r'}|\right)}{\dfrac{4\pi\sin\theta}{\lambda}\,|\boldsymbol{\psi}_r-\boldsymbol{\psi}_{r'}|} + \sum_{s,s'=1}^{\mu} \frac{\sin\left(\dfrac{4\pi\sin\theta}{\lambda}\,|\boldsymbol{\varphi}_s-\boldsymbol{\varphi}_{s'}|\right)}{\dfrac{4\pi\sin\theta}{\lambda}\,|\boldsymbol{\varphi}_s-\boldsymbol{\varphi}_{s'}|} - 2\sum_{r=0,\,s=1}^{\mu} \frac{\sin\left(\dfrac{4\pi\sin\theta}{\lambda}\,|\boldsymbol{\psi}_r-\boldsymbol{\varphi}_s|\right)}{\dfrac{4\pi\sin\theta}{\lambda}\,|\boldsymbol{\psi}_r-\boldsymbol{\varphi}_s|} \right] . \quad . \quad . \quad (4)$$

The moduli represent distances within the relaxed region of the crystal surrounding one interstitial, and the three sums correspond to all distances between atoms, lattice sites, and an atom and lattice site respectively.

Integrating each term of (4) over 4π of solid angle we obtain the total cross section, which is obtained from a transmission experiment:

$$\sigma_t = 4\pi b^2\nu \left[\sum_{r,r'=0}^{\mu} \frac{\sin^2\left(\dfrac{2\pi}{\lambda}\,|\boldsymbol{\psi}_r-\boldsymbol{\psi}_{r'}|\right)}{\left(\dfrac{2\pi}{\lambda}\,|\boldsymbol{\psi}_r-\boldsymbol{\psi}_{r'}|\right)^2} + \sum_{s,s'=1}^{\mu} \frac{\sin^2\left(\dfrac{2\pi}{\lambda}\,|\boldsymbol{\varphi}_s-\boldsymbol{\varphi}_{s'}|\right)}{\left(\dfrac{2\pi}{\lambda}\,|\boldsymbol{\varphi}_s-\boldsymbol{\varphi}_{s'}|\right)^2} - 2\sum_{r=0,\,s=1}^{\mu} \frac{\sin^2\left(\dfrac{2\pi}{\lambda}\,|\boldsymbol{\psi}_r-\boldsymbol{\varphi}_s|\right)}{\left(\dfrac{2\pi}{\lambda}\,|\boldsymbol{\psi}_r-\boldsymbol{\varphi}_s|\right)^2} \right] . \quad . \quad (5)$$

The sums are identical to those in (4).

These summations are similar to those in the diffraction theory of polyatomic molecules (e.g. James 1948), where terms corresponding to all interatomic distances in the molecule are included; in comparison the sums here include vacant lattice sites, and some terms are negative.

Finally we observe that in a lattice containing two sorts of defects, both with relaxed neighbouring atoms, for example interstitials and vacancies, the total scattering is simply the sum of two series such as (4) or (5) to a good approximation, provided that the defect concentration is not greater than a few per cent.

§ 3. APPLICATION TO FACE-CENTRED AND BODY-CENTRED CUBIC METALS

We present here values of the total and differential scattering cross sections for a point defect in a f.c.c. and a b.c.c. metal considering relaxation of nearest neighbours only, the variable parameters being the relaxation ϵ, the wavelength and the scattering angle.

Figure 1 depicts the total cross section of an interstitial in copper as a function of neutron wavelength. Three values of ϵ, the distance that the six nearest neighbours have moved outwards from their lattice sites, are shown; in all cases ϵ is expressed in units of half the lattice spacing, a. For copper Huntington (1953) and Tewordt (1958) find values of ϵ ranging from 0·210 to 0·257. Cross sections are expressed as fractions of the very long wavelength value $4\pi b^2$; this is also the value σ_t that would be observed if the lattice was not relaxed. Values of a/λ on the abscissa enable these results to be applied directly to other f.c.c. lattices.

Figure 2 shows the variation in total cross section with ϵ for three values of a/λ.

The solid lines in fig. 3 depict the differential scattering cross section of an interstitial in copper as a function of angle. They are for a neutron wavelength of 7·6 Å, which corresponds to $a/\lambda = 0{\cdot}475$.

Figures 4–6 are the corresponding curves for a vacancy in copper, where the twelve nearest neighbours are relaxed inwards. Tewordt (1958) has found $\epsilon = 0{\cdot}019\sqrt{2}$ and $0{\cdot}023\sqrt{2}$, using two different potentials.

Figures 7–9 are the corresponding curves for a vacancy in a b.c.c. material with the eight nearest neighbours relaxed and λ and θ values that are applicable to molybdenum. The values of ϵ may be compared with that of $0{\cdot}0505\sqrt{3}$ calculated by Girifalco and Streetman (1958).

§ 4. DISCUSSION

The results of figs. 1–9 show how marked is the influence of reasonably expected values of relaxation on the scattering cross section. A neglect of it in metals could lead to an experimental estimate in the numbers of defects that was in error by a large factor.

It is pertinent to ask how much in error these results are compared with physical reality, when other neighbouring atoms are relaxed as well. Let us consider the 6(1, 0, 0) and 24(2, 1, 0) neighbours about an interstitial in copper relaxed to new positions $(1+\alpha,\ 0,\ 0)$, $(2+\omega,\ 1+\eta,\ 0)$, where coordinates, centred about the interstitial, are in units of $a/2$. Tewordt (1958) has shown that these are the two kinds of atoms most relaxed. Transmission and differential cross sections have been calculated for certain values of λ and θ, for $\alpha=0{\cdot}25$, $\omega=0{\cdot}050$, $\eta=0{\cdot}055$, which are

Fig. 1

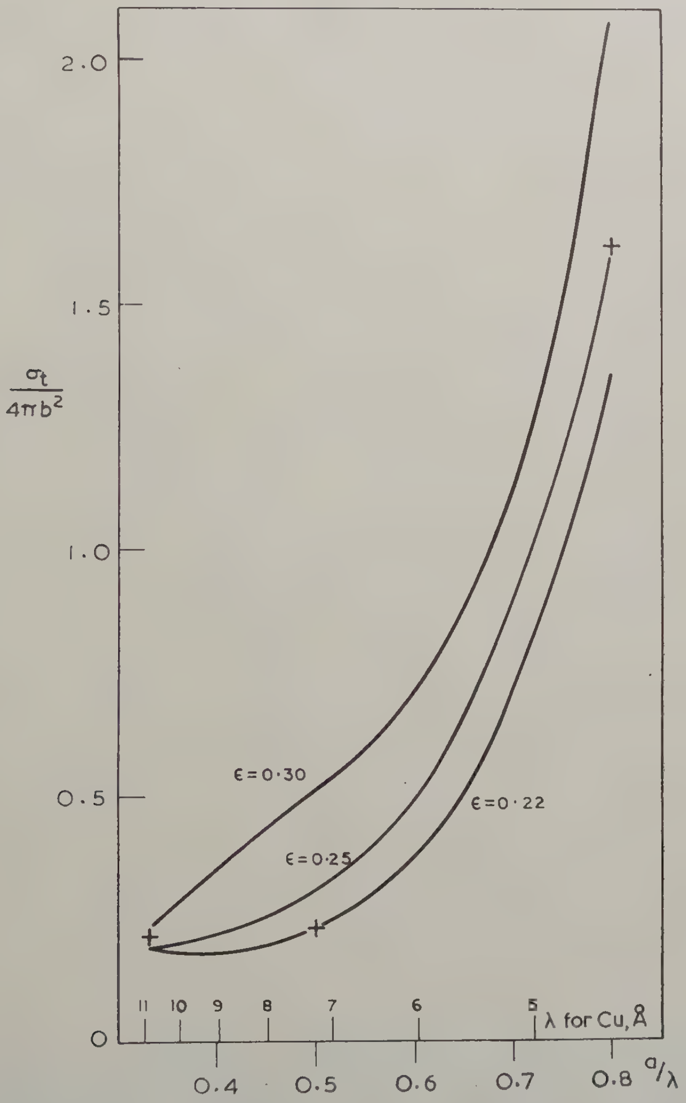

The total cross section σ_t of an interstitial in a f.c.c. lattice plotted as a function of wavelength. σ_t is divided by $4\pi b^2$, which is the total cross section of an interstitial in an unrelaxed lattice. The curves are results of calculations when only nearest neighbours are allowed to relax. The points make allowance for the relaxation of other neighbouring atoms as well, when $\epsilon=0{\cdot}25$. Values of these relaxations which are valid for copper were used.

values lying between those calculated by Tewordt using two different potentials. The results are presented as points on figs. 1 and 3, and may be compared with the curves for $\epsilon = 0{\cdot}25$, when relaxation of (2, 1, 0) atoms is neglected.

Fig. 2

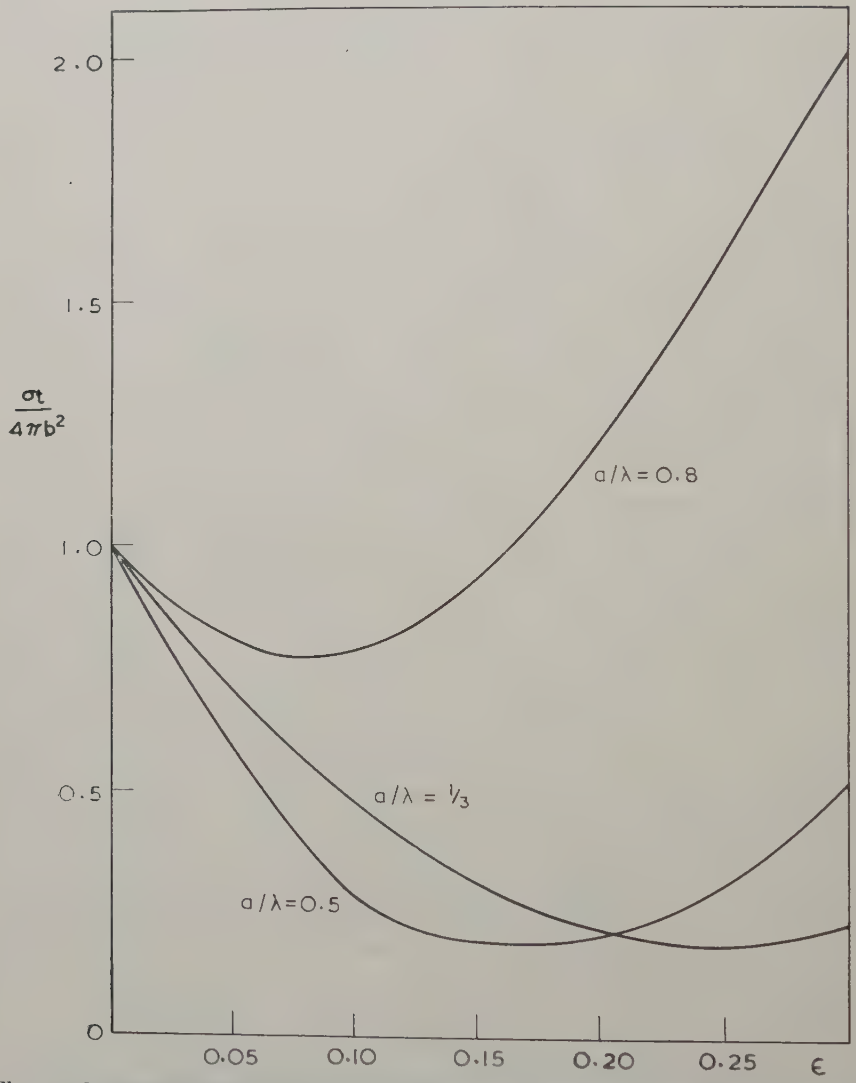

The total cross section of an interstitial in a f.c.c. lattice plotted as a function of the relaxation. The calculations make allowance for the relaxation of nearest neighbours only. For copper $\epsilon \sim 0{\cdot}25$.

Tewordt has also calculated the relaxation of next-nearest neighbours around a vacancy in copper. The nearest and next nearest neighbours, coordinates (1, 1, 0) and (2, 0, 0) are relaxed to $(1-\beta,\ 1-\beta,\ 0)$ and

$(2-\zeta, 0, 0)$ respectively, where $\beta = 0{\cdot}020$ and $\zeta = 0{\cdot}002$. The results are shown on figs. 4 and 6 and are to be compared with $\epsilon = 0{\cdot}02\sqrt{2}$, when relaxation of $(2, 0, 0)$ atoms is neglected.

For a vacancy in molybdenum the coordinates of the relaxed nearest and next-nearest neighbours are $(1-\gamma, 1-\gamma, 1-\gamma)$ and $(2-\chi, 0, 0)$

Fig. 3

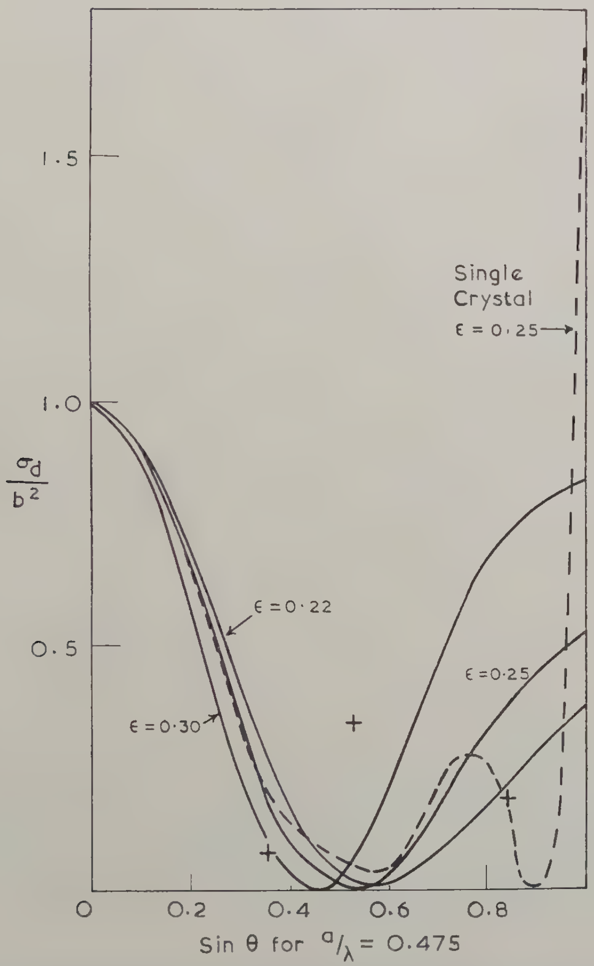

The differential cross section σ_d of an interstitial in copper, plotted as a function of angle. σ_d is divided by b^2, which is the differential cross section of an interstitial in the unrelaxed lattice. The neutron wavelength is 7·6 Å. Solid lines are results of calculations when only nearest neighbours are allowed to relax. The points make allowance for the relaxation of other neighbouring atoms as well, with $\epsilon = 0{\cdot}25$. The broken line is for an interstitial in a copper single crystal for neutrons incident in the [100] direction and scattered in the (001) plane. Relaxation of nearest neighbours only is considered.

respectively, where $\gamma = 0{\cdot}0505$ and $\chi = 0{\cdot}0224$, using the results of Girifalco and Streetman (1958). The results may be compared with the nearest neighbour approximation for $\epsilon = 0{\cdot}05\sqrt{3}$.

These results indicate that the cross section is only slightly in error by neglecting the relaxation of next nearest neighbours. Only certain parts of the curves for an interstitial in copper, when the relaxation is very large, are measurably affected.

Fig. 4

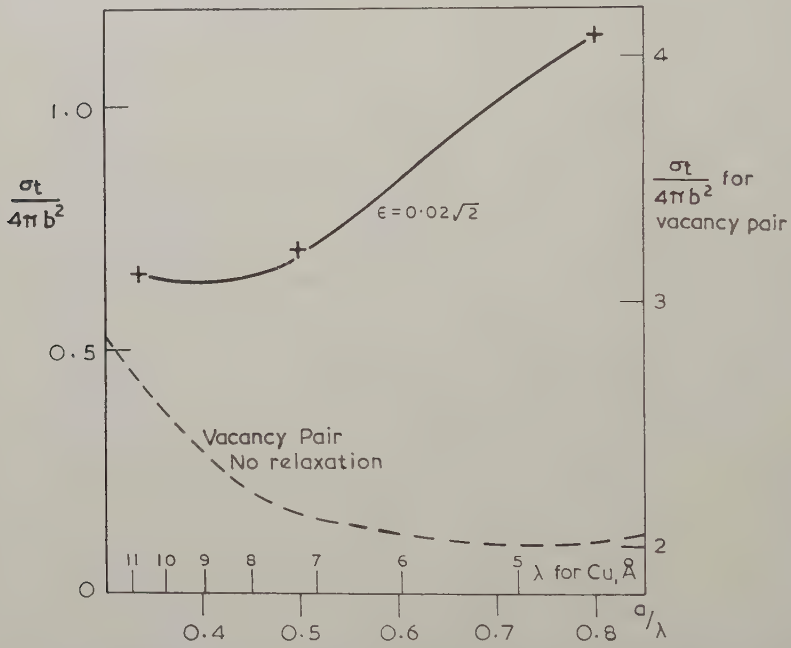

The total cross section σ_t of a vacancy in a f.c.c. lattice plotted as a function of wavelength. The solid line is the result of calculations when only nearest neighbours are allowed to relax. The points make allowance for the relaxation of next-nearest neighbours also, using values which are valid for copper. For comparison the broken line shows the total cross section of a vacancy pair in a f.c.c. lattice, assuming there is no relaxation of the surrounding lattice.

We do not expect the relaxation of atoms a large distance from the point defect to influence these scattering cross sections. This is because in the elastic continuum approximation the density of an infinite medium at any point remains unchanged when a point defect is introduced into it, so that the scattering intensity is zero, as in the perfect lattice.

All the results presented so far have been for randomly oriented polycrystalline solids. To evaluate the differential scattering cross section for a single crystal we must sum terms of the general type

Fig. 5

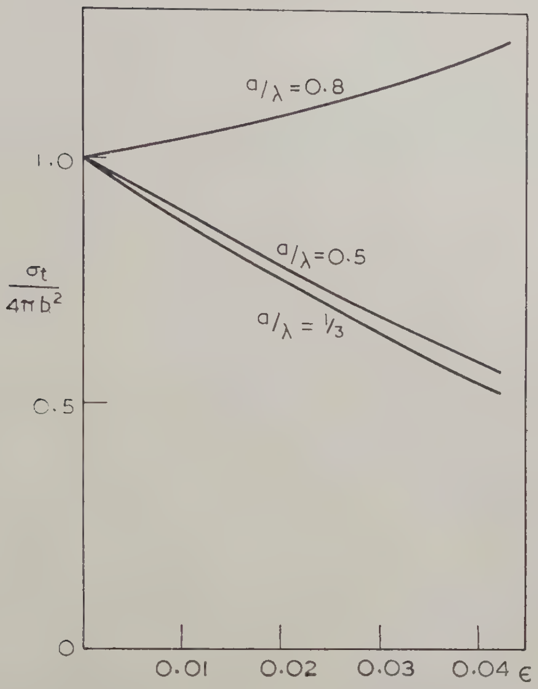

The total cross section of a vacancy in a f.c.c. lattice plotted as a function of the relaxation. The calculations make allowance for the relaxation of nearest neighbours only. For copper $\epsilon \sim 0{\cdot}028$.

Fig. 6

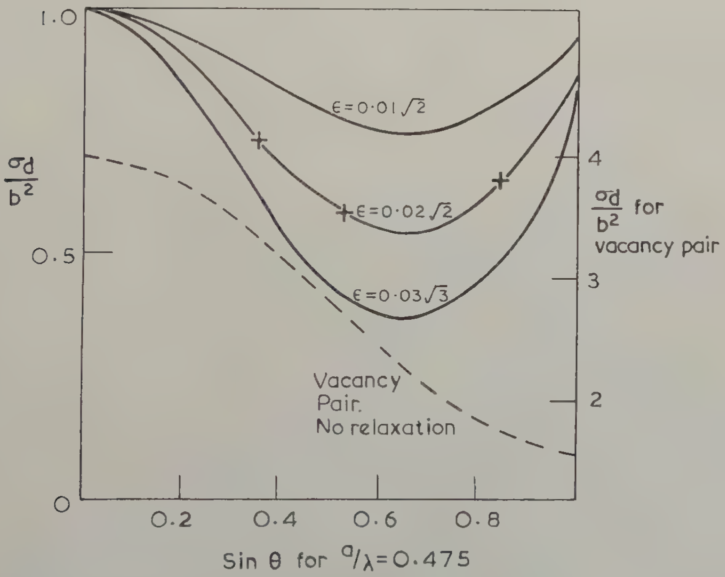

The differential cross section σ_d of a vacancy in copper, plotted as a function of angle. The neutron wavelength is 7·6 Å. Solid lines are results of calculations when only nearest neighbours are allowed to relax. The points make allowance for the relaxation of the next-nearest neighbours as well, with $\epsilon = 0{\cdot}02\sqrt{2}$. For comparison the broken line shows the differential cross section of a vacancy pair in copper, assuming there is no relaxation of the surrounding lattice.

cos [$\boldsymbol{\kappa} . (\mathbf{x} - \mathbf{y})$]. The dashed curve in fig. 3 illustrates the differential cross section of an interstitial in a copper single crystal for $\epsilon = 0{\cdot}25$. The beam is incident along the [100] axis and is scattered in the (001) plane. It is seen that for small phase differences, when θ is small, the scattering is the same as polycrystalline material; only at larger values of θ do the curves diverge.

Fig. 7

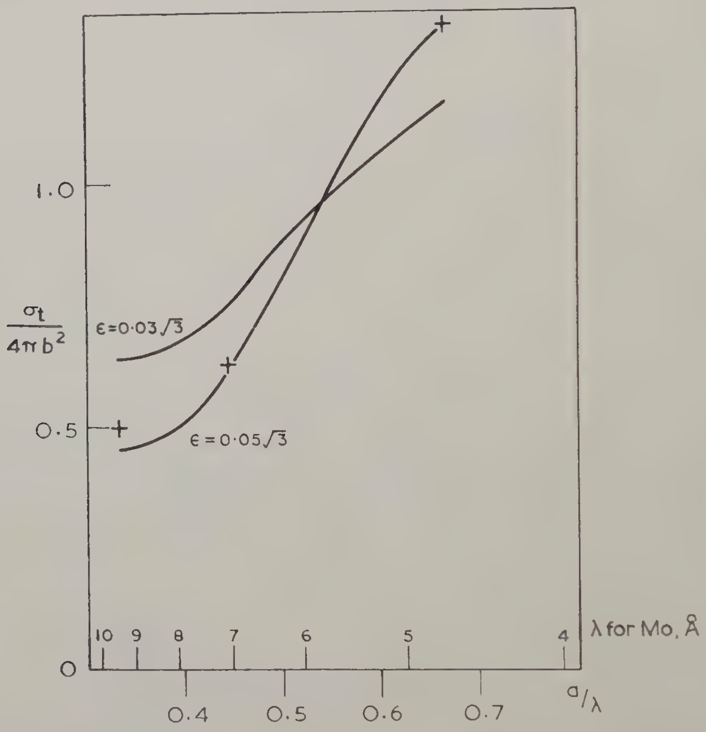

The total cross section σ_t of a vacancy in a b.c.c. lattice, plotted as a function of wavelength. The curves are results of calculations when only nearest neighbours are allowed to relax. The points make allowance for the relaxation of other neighbouring atoms, when $\epsilon = 0{\cdot}05\sqrt{3}$. Values of these relaxations which are valid for molybdenum were used.

It was pointed out above that the cross section of agglomerated defects will depend on wavelength and angle. The scattering from a defect pair (neglecting relaxation) in copper is shown as a function of λ and θ in figs. 4 and 6 respectively, for comparison with relaxation effects. Apart from low scattering angles the curves are quite different, so that in principle the two effects are experimentally separable (but see next paragraph).

The results of this paper show that lattice relaxation and the state of agglomeration of defects influence the scattering cross section to a comparable extent. This is a serious disadvantage when neutron

Fig. 8

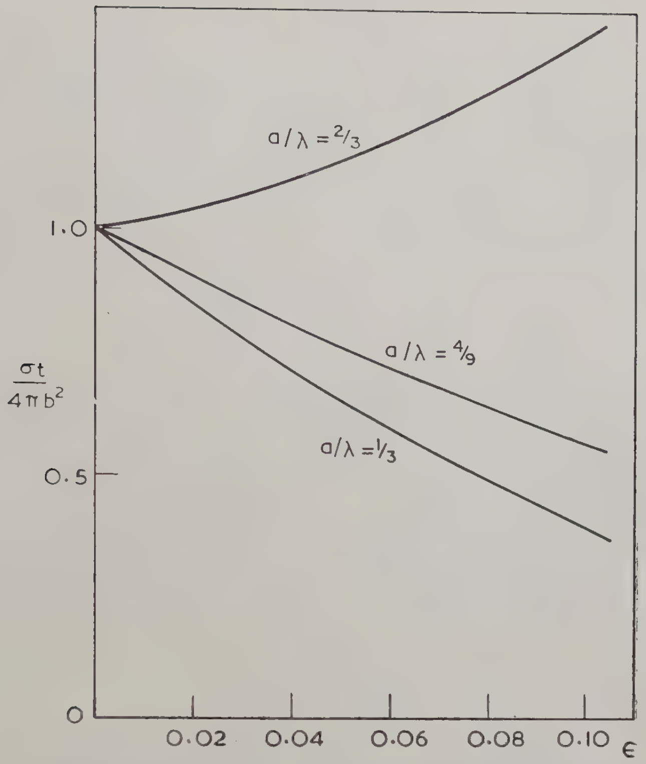

The total cross section of a vacancy in a b.c.c. lattice plotted as a function of the relaxation. The calculations make allowance for the relaxation of nearest neighbours only. For molybdenum $\epsilon \sim 0{\cdot}087$.

Fig. 9

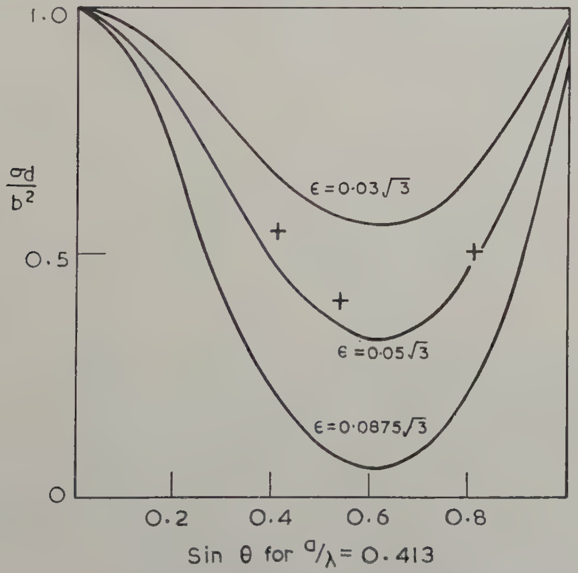

The differential cross section σ_d of a vacancy in molybdenum plotted as a function of angle. The neutron wavelength is 7·6 Å. Solid lines are results of calculations when only nearest neighbours are allowed to relax. The points make allowance for the relaxation of the next-nearest neighbours as well, with $\epsilon = 0{\cdot}05\sqrt{3}$.

scattering experiments are used to study the nature of defects produced after irradiation damage because these two effects cannot be distinguished, since only for certain elementary defects in a limited number of materials is the relaxation known. To illustrate this, fig. 4 depicts the scattering of a vacancy pair, without relaxation, the value of which is unknown. It may be that with relaxation included the curve would become a straight line independent of wavelength, like a defect with no relaxation, or alternatively have the shape like the other curve in fig. 4 which is for a single vacancy with relaxation, so that results would be ambiguous. Perhaps in certain particular cases, for example in materials possessing a more open structure, when relaxation should be less pronounced, or with single crystals, where the cross section fluctuates more rapidly with wavelength and scattering angle there may be less ambiguity.

However, if the size of defect agglomerates is known in a particular solid, measurements of the neutron scattering cross section will yield information about the relaxation of the surrounding lattice. One such example is a very dilute solid solution, when the solute atoms are effectively point singularities randomly dispersed in the solvent lattice : in particular, if this lattice possesses cubic symmetry, the relaxation of nearest neighbours around each solute atom may be determined directly from such an experiment.

References

Antal, J. J., and Goland, A. N., 1958, *Phys. Rev.*, **112,** 103.

Antal, J. J., Weiss, R. J., and Diernes, G. J., 1955, *Phys. Rev.*, **99,** 1081.

Butterworth, I., Egelstaff, P. A., London, H., and Webb, F. J., 1957, *Phil. Mag.*, **2,** 917.

Girifalco, L. A., and Streetman, J. R., 1958, *J. Phys. Chem. Solids*, **4,** 182.

Huntington, H. B., 1953, *Phys. Rev.*, **91,** 1092.

James, R. W., 1948, *The Optical Principles of the Diffraction of X-rays* (London: Bell), p. 482.

Tewordt, L., 1958, *Phys. Rev.*, **109,** 61.

The Nature of Radiation-induced Point Defect Clusters†

By R. S. Barnes and D. J. Mazey
Atomic Energy Research Establishment, Harwell, Didcot, Berks

[Received June 21, 1960]

Abstract

The electron microscope has been used to examine point defect clusters produced in copper and aluminium foils bombarded with $1{\cdot}4\times10^{17}$ alpha-particles cm^{-2}. The foils were bombarded as a stack and, in copper, both those through which the alpha-particles had passed and that in which they came to rest appeared similar, containing dislocation loops ($r\sim200$ Å) and a background of more numerous and smaller dots ($r\sim20$ Å). The behaviour at grain boundaries suggested that these two types of cluster were due to different point defects. Whereas the dislocation loops normally annealed out at about 350°c, in the foil in which the alpha-particles came to rest (containing $\sim10^{15}$ atoms of helium cm^{-2}) they grew to form a dislocation tangle, and eventually small helium bubbles ($r\sim40$ Å) appeared in the same number as the original small dots. These results indicate that the dislocation loops are due to the clustering of *interstitial atoms* and the small dots are clusters formed from *vacancies*. It is also inferred that the helium atoms are in interstitial positions during the bombardment, and form bubbles by nucleating upon the clusters.

§ 1. Introduction

The much smaller energy needed to form a vacancy ensures that the point defect clusters observed in quenched metals are due to precipitation of the excess concentration of vacancies and not interstitial atoms. However, during atomic bombardment vacancies and interstitial atoms must be produced in nearly equal numbers, because they are produced by a collision process, and the effects observed may be due to either type of defect. Bombardment with alpha-particles introduces both point defect clusters and helium atoms, the latter on subsequent heating capture large numbers of vacancies (Barnes *et al.* 1958) and enable the nature of the point defect clusters to be determined.

Thin films of copper extracted from a solid block which had been bombarded with alpha-particles have been examined and helium bubbles observed within them (Barnes 1960). However, the extraction of thin films from a solid block is tedious and wasteful of material. The results described here were obtained by placing stacks of thin sheets of metal in the external beam of a cyclotron accelerating alpha-particles. These were then thinned by normal electrolytic methods until they could be viewed in transmission in the electron microscope. Sheets from various depths beneath the bombarded surface were studied and the effects produced by the passage of the alpha-particles (in the sheets near the surface) compared with those produced where the helium atoms were deposited (in the sheet corresponding to the end of the range of the alpha-particles).

---

† Communicated by the Authors.

Johnson Matthey spectroscopically standardized copper or aluminium was used and the sheets were initially either 0·002 in. or 0·001 in. thick and were vacuum annealed for 2 hours at 650°c before bombardment; during bombardment their temperature did not exceed 250°c. As the range of the 38 Mev alpha-particles from the cylotron was 0·009 in. in copper, about five 0·002 in. or nine 0·001 in. sheets were affected during each bombardment.

However, normally only one of the sheets contained the helium. This was located by observing the helium bubbles after heating a little of a sheet to about 800°c for 2 hours. Figure 1† shows the cross section of a 0·001 in. foil (after electrolytic polishing) containing unresolved helium bubbles near the grain boundaries (Barnes *et al.* 1958). Suitable masking enabled other pieces from this same sheet to be thinned (after the appropriate annealing treatment) leaving the centre of the helium layer within it.

§ 2. Results

The photographs in figs. 2 and 3 were taken from foils, containing no helium, through which $1{\cdot}4 \times 10^{17}$ alpha-particles cm^{-2} ($32\,\mu$ amp hours) had passed. The appearance of the electron micrographs taken from various distances along the alpha-particle tracks showed little variation, each containing a number of relatively large dislocation loops ($r \sim 200$ Å) and a background of much smaller dark dots ($r \sim 20$ Å) (fig. 2). Figures 3 (*a*), (*b*) and (*c*) are successive photographs of a similar foil taken while it was at about 350°c in the 'hot-stage' of the electron microscope. At this temperature the loops disappeared in less than 30 min. Sheets were also annealed in a vacuum furnace at various temperatures. After a 2-hour anneal at 300°c there was little change in the appearance of the films, after the same time at 325°c slight annealing had occurred and after 4 hours at 350°c complete annealing of the loops had occurred.

The thin films in which the helium atoms had come to rest contained both large loops and small dots, which were not significantly different in size from the above (table), but the dots appeared to be localized around the loops (fig. 4). The annealing behaviour was however markedly different and the series of photomicrographs of foils annealed in a vacuum furnace shows this (fig. 5). Instead of the dislocation loops disappearing after 2 hours at 350°c (fig. 5 *a*) they enlarged and after 2 hours at 450°c (fig. 5 *b*) had become a tangle of dislocations. After this anneal there were small bubbles near the grain boundaries (fig. 5 *b*). After 2 hours at 550°c small bubbles pervaded the grains and on further heating for 2 hours at 750°c they became larger (fig. 5 *c* and *d*). At this temperature larger bubbles occurred along the grain boundaries (fig. 5 *e*) consistent with previous observation (Barnes 1960).

---

† All figures are shown as plates.

Aluminium foils through which the alpha-particles had passed contained no observable damage effects, but the foil with helium in, contained a dislocation tangle, and upon heating small helium bubbles appeared.

		Radius (r) cm	Number cm^{-2} (n)	Number of atom spaces cm^{-2} in	
				Loops $(4\pi/3)(r/a)^2 n$	Spheres $(16\pi/3)(r/a)^3 n$
Figure 2 (*a*)	Point defects only	$2{\cdot}2 \times 10^{-6}$	$4{\cdot}2 \times 10^{9}$	$1{\cdot}1 \times 10^{14}$	—
Figure 2 (*b*)	Point defects only	$2{\cdot}2 \times 10^{-6}$	$6{\cdot}4 \times 10^{9}$	$1{\cdot}7 \times 10^{14}$	—
Figure 4	He and point defects	$1{\cdot}6 \times 10^{-6}$	$1{\cdot}4 \times 10^{10}$	$2{\cdot}0 \times 10^{14}$	—
Figure 2 (*a*)	Point defects only	$2{\cdot}5 \times 10^{-7}$	$9{\cdot}0 \times 10^{10}$	$3{\cdot}6 \times 10^{13}$	$5{\cdot}0 \times 10^{14}$
Figure 4	He and point defects	$1{\cdot}9 \times 10^{-7}$	$1{\cdot}2 \times 10^{11}$	$2{\cdot}4 \times 10^{13}$	$3{\cdot}0 \times 10^{14}$
Figure 5 (*d*)	He bubbles	$4{\cdot}0 \times 10^{-7}$	$1{\cdot}4 \times 10^{11}$	—	$3{\cdot}2 \times 10^{15}$

The size and number per unit area of the dislocation loops (the first three rows), the dots (the next two rows) and the bubbles (last row) observed in the thin films. The foil thicknesses were approximately 1000 Å.

§ 3. DISCUSSION

Dislocation loops form in many metals during quenching (Hirsch *et al.* 1958) their number and size depending upon the quenching conditions. These loops which are produced by the precipitation of the highly supersaturated vacancies during the quench, do not normally contain stacking faults and are of dislocations with Burgers vectors $a/2$ [110]. The appearance of the copper sheets through which alpha-particles have passed (fig. 2) resembles that of a quenched foil. Closed loops can be identified but their shapes are less regular than those in quenched metals and in addition there is a very fine background of dots uniformly distributed throughout the foil. The annealing behaviour is similar to that of a quenched metal (Silcox and Whelan 1960) the loops disappearing after several hours at 350°c. The behaviour of the sheets containing the helium upon annealing is notably different and it is this which indicates the nature of the clusters†.

3.1. *Nature of Large Loops*

The larger dislocation loops ($r \sim 200$ Å) which formed in the copper disappeared at about 350°c but at this temperature began to grow when helium was present. As the helium atoms are known to be very effective in capturing vacancies (Barnes *et al.* 1958, Barnes 1960) they will extract vacancies from any nearby dislocation by climb, if the temperature is sufficient for vacancy formation and migration. In copper this temperature is about 350°c. Dislocation loops formed by the clustering of *vacancies* would contract in such a situation. Thus the growth of the large loops at this temperature suggests that they are formed by the clustering of *interstitial atoms.* The anneal also makes the loops more regular which would happen during climb. Their further growth to form a tangle of dislocation lines at 450°c is consistent with this.

The total area of these large loops can be used to estimate the number of agglomerated interstitial atoms. The values given in the table, assuming that the loops lie on $\{111\}$ planes, suggest that there are about $1{\cdot}6 \times 10^{14}$ interstitial atoms cm^{-2} both in those thin films containing helium and those not.

The annealing of the loops in regions containing no helium was such that the loops became smaller and disappeared after 2 hours at 350°c. Presumably the vacancies which were present in equal numbers to the interstitial atoms, annihilated these loops.

Near grain boundaries (fig. 2 *b*) there is a zone ($\sim 8 \times 10^{-5}$ cm wide) which contains none of the larger loops. Presumably the interstitial atoms have been captured by the boundary instead of forming loops, suggesting that they can normally migrate distances of this magnitude during the bombardment.

3.2. *Nature of the Dots*

The background of small dots, seen in fig. 2 (*b*), continues right up to the grain boundary, with no depleted zone, suggesting that they have formed from point defects which can diffuse only $\gtrsim 500$ Å during the bombardment. They must be very different from those producing the large loops and are probably formed from the vacancies which must be present in nearly equal numbers.

It is very difficult to estimate the number of point defects clustered in these small dots which do not appear to be dislocation loops; their size is uncertain and may be determined by a strain field, also their number may be underestimated because many are too small to be resolved. An estimate (table) suggests that if they are dislocation loops there are only about one fifth as many vacancies in them as there are interstitial atoms agglomerated in the larger loops. However, if the same values are used, but it is assumed that they are spherical voids, the number of vacancies agglomerated in them (table) more nearly equals the number of interstitial atoms, as should be the case. Certainly very small vacancy clusters would have a lower energy if arranged as a sphere rather than as a plate (Kuhlman-Wilsdorf and Wilsdorf 1960)†.

---

† A difference in annealing of hardness between regions through which alpha-particles had passed and the region in which they were deposited had been noticed previously (Ghosh *et al.* 1960).

The behaviour of the aluminium foils was similar to that of copper, but presumably in the former the vacancies and interstitial atoms had annihilated during the bombardment except where helium was present, where the appearance of the dislocation tangle and the formation of bubbles was almost the same as in the copper.

3.3. *Helium Bubble Nuclei*

After annealing at 450°C small gas bubbles can be seen as white dots near the grain boundaries on the photomicrographs (fig. 5*b*). Eventually after an anneal of 1 hour at 750°C these bubbles can be seen throughout the film if it is so oriented in the microscope that the dislocation lines do not give a contrast which obscures the bubbles (fig. 5*d*). These spots are 40 Å in radius and have the characteristics of gas bubbles; they are spherical, i.e. they appear round with light centres becoming darker at their edges, with no diffraction contrast. The bubbles appear in rows and lie upon the dislocation lines (Barnes 1959–1960). This can be demonstrated by re-orientating the foil to give contrast effects at the dislocations.

The number of helium bubbles observed once there are sufficient vacancies available is $\sim 10^{11}\,\mathrm{cm}^{-2}$ almost the same as the number of small dots (table). It seems possible that these dots are the nuclei upon which the helium bubbles form.

The number of helium atoms (m) contained in the films can be calculated from the photomicrographs of the bubbles, using the formula (Barnes 1959),

$$(2\gamma/r)\,\tfrac{4}{3}\pi r^3 n = mkT$$

where γ is the surface energy (about $10^3\,\mathrm{ergs\,cm}^{-2}$), r is the bubble radius (40 Å), n is their number in unit area of the film ($1{\cdot}4\times10^{11}\,\mathrm{cm}^{-2}$), k is Boltzmann's constant, and T the absolute temperature (1023°K), therefore $m = 1{\cdot}4\times10^{15}\,\mathrm{cm}^{-2}$ (i.e. an atomic concentration of approximately $1{\cdot}7\times10^{-3}$ in the copper). One concludes that there are approximately nine helium atoms for each interstitial atom in the loops and for each vacancy in the black dots. The small number of interstitial atoms observed in all these films (table) implies that most of the helium atoms were interstitial during the bombardment, because if each helium atom was substitutional $1 \cdot 4 \times 10^{15}$ vacancies cm^{-2} must be provided and $1 \cdot 4 \times 10^{15}$ interstitial atoms cm^{-2} would be left ; only 1/10th this number was observed.

---

† Recent observation of foils annealed for 1 hour at 400°C show that in some grains the remaining dots become triangular. This implies that the clusters are tetrahedra of stacking fault (Silcox and Hirsch 1959) both because of their shape and their stability above the self-diffusion temperature.

The clusters would capture helium atoms during irradiation and gas bubbles would form upon them. However, presumably because of the shortage of vacancies these bubbles do not grow and thus cannot accommodate further helium atoms. It can be estimated from the gas laws that only a fraction of the helium atoms reside in the vacancy clusters, during bombardment. Subsequent heating permits the acquisition of vacancies from the interstitial atom agglomerates, which grow. The number of vacancies these loops (radius ~ 200 Å) produce during their climb to form the tangle of dislocations (equivalent to a radius of about 1000 Å) is such that approximately two vacancies are provided per helium atom. This would be sufficient to enable each helium atom to become substitutional. The process ceases either because the helium bubbles eventually lock the dislocations and prevent their further climb, or because the dislocations become locked by mutual interaction. Whichever the reason, the structure remains stable until vacancies are provided from the grain boundaries (fig. 5 *e*) and then the helium atoms produce observable bubbles as described previously (Barnes 1960). The dislocation tangle also enlarges with further heating and continues to enlarge as the bubbles grow larger and reduce in number.

§ 4. CONCLUSIONS

Copper bombarded with $1 \cdot 4 \times 10^{17}$ alpha-particles cm^{-2} at about 200°c contains both dislocation loops $r \sim 200$ Å formed by the clustering of interstitial atoms, and much smaller and more numerous dots ($r \sim 20$ Å) which are probably clusters formed from the less mobile vacancies. On annealing at about 350°c the clusters annihilate one another by the generation and diffusion of single vacancies so that the material reverts much to its original state. However, when the material contains large numbers of helium atoms these stabilize the vacancy clusters, and at about 350°c they are able to grow by taking vacancies from the dislocation loops which, because they are formed from interstitial atoms grow, eventually becoming a tangle. The steady acquisition of vacancies by the small bubbles enables them to accommodate more helium atoms until eventually they can be clearly resolved in the electron microscope.

Thus it appears that the vacancies produced by irradiation provide some space for the helium atoms to form bubbles. However, more vacancies are supplied from the dislocation loops which climb, but the total number is limited as suggested previously (Barnes 1960) so that the size of the bubbles which form is too small to be detected using the normal optical microscope until large numbers of vacancies have been supplied from the grain boundaries.

ACKNOWLEDGMENTS

We are grateful to Mr. W. Hardy and his team at Birmingham University for conducting the cyclotron bombardments, and Mr. C. K. Jackson for his assistance with the electron microscopy, and in particular with the 'hot-stage' experiment.

REFERENCES

BARNES, R. S., 1959, *Nuclear Metallurgy*, **6,** 21 ; 1959–1960, *J. Inst. Met.*, **88,** 13 ; 1960, *Phil. Mag.*, **5,** 635.
BARNES, R. S., REDDING, G. B., and COTTRELL, A. H., 1958, *Phil. Mag.*, **3,** 97.
GHOSH, T. K., BEAVERS, J., and BARNES, R. S., 1960, *J. Inst. Met.* (in the press).
HIRSCH, P. B., SILCOX, J., SMALLMAN, R. E., and WESTMACOTT, K. H., 1958, *Phil. Mag.*, **3,** 897.
KUHLMANN-WILDORF, D., and WILSDORF, H. G. F., 1960, *J. appl. Phys.*, **31,** 516.
SILCOX, J., and HIRSCH, P. B., 1959, *Phil. Mag.*, **4,** 72.
SILCOX, J., and WHELAN, M. J., 1960, *Phil. Mag.*, **5,** 1.

The Growth of Prismatic Dislocation Loops during Annealing[†]

By C. A. Johnson[‡]
Materials Research Laboratory, University of California,
Berkeley, California

[Received June 20, 1960]

Abstract

Recent observations of the growth of quenched-in dislocation loops during annealing are discussed. A mechanism for the coalescence of loops is proposed. The mechanism depends on short-circuit diffusion around the periphery of prismatic dislocation loops. This mechanism is contrasted with the theory of loop coalescence by vacancy diffusion through the matrix. It is shown that the experimental observations are in better accord with the short-circuit diffusion theory.

Interpretation of the experimental observations on the basis of the short-circuit mechanism leads to a value for the activation energy for diffusion along a dislocation line. For aluminium this value is calculated to be 0·7 ev.

§ 1. Introduction

In recent electron-micrographic experiments on the annealing of quenched aluminium, Silcox and Whelan (1960) and Vandervoort and Washburn (1960) have observed that the density of dislocation loops present in the as-quenched material decreased markedly upon annealing. In the experiments of Silcox and Whelan, annealing was carried out in two distinct ways: annealing of the foil *in situ* within the microscope so that the details could be observed as annealing proceeded, and annealing of the bulk material before thinning, in which case the progress of annealing could not be followed continuously.

It was found that the annealing of loops in foil became noticeable at a temperature of 170°c and proceeded by the shrinking of all loops, and that there was no tendency for any of the loops to grow at the expense of the others. Silcox and Whelan have accounted for these observations by proposing that vacancies are evaporated from the periphery of each loop and that these vacancies then diffuse to the surface of the foil. Since the free surfaces of the foil provide a nearby sink for vacancies, this process can occur rapidly at moderate temperatures.

In specimens prepared from material annealed in bulk, however, they found that the decrease in loop density was accompanied by the growth of some loops. This agrees with the observations of Vandervoort and Washburn, who found that considerable loop growth occurred in samples prepared from bulk material which had been annealed for ten minutes at 150°c. In samples which had been annealed for ten minutes at 125°c little loop growth was observed, but after ten minutes at 200°c annealing of the loops seemed to be essentially complete, with only a very few large loops remaining.

[†] Communicated by the Author.

[‡] Graduate Physicist, Materials Research Laboratory, University of California, Berkeley 4, California.

That the growth of the loops must involve vacancy diffusion follows from the generally accepted view that the loops have originated by the collapse of vacancy precipitates. Accordingly, Silcox and Whelan have interpreted their observations on material annealed in bulk form in terms of the evaporation of vacancies from the periphery of a small loop, and the subsequent diffusion of these vacancies through the matrix to precipitate on a larger loop. The purpose of this paper is threefold: to propose a mechanism by which loop growth can occur without employing diffusion through the matrix between two loops, to contrast this process with the vacancy diffusion process proposed by Silcox and Whelan, and to interpret the experimental results in terms of both processes.

The diffusion of vacancies through the matrix (bulk self-diffusion) is not the only means by which loops could coalesce. It is proposed that an effective mechanism for the coalescence of loops involves a diffusion short-circuit process. This is illustrated in fig. 1, in which atoms diffuse rapidly along the periphery of the loop. The rate at which diffusion can take place along this short-circuiting path is determined by the activation energy for diffusion along a dislocation line. The activation energy for diffusion along dislocation lines has been determined for various metals (Hoffman and Turnbull 1951, Hendrickson and Machlin 1954, Turnbull and Hoffman 1954); the values obtained range between one-half and two-thirds of the activation energy for bulk diffusion. The activation energy for diffusion along dislocation lines in aluminium has not been measured, but it would be expected that it is appreciably lower than the activation energy for bulk self-diffusion.

The elastic interaction between two nearby loops provides a driving force tending to create a net flow of diffusing atoms from the closest to the more distant edges of both loops†. As shown in fig. 2, this short-circuit diffusion around the periphery of the loops caused the two loops to move together. For convenience this process will be called 'self-climb'. However, self-climb alone can only account for the coalescence of coplanar loops. Loops can, in principle, also move by prismatic glide along a cylindrical surface inclined to the plane of the loop and containing the Burgers vector of the loop. The combination of self-climb and prismatic glide would therefore permit the motion of loops in any direction. The limitations on prismatic glide of loops have been discussed by Kuhlmann-Wilsdorf (1958), and will also be discussed below.

---

† The elastic interactions providing this driving force will be smaller in the foil due to the fact that a thin film of material can relieve these stresses by buckling. A comprehensive treatment of the limitations on dislocation interactions imposed by the thinness of foils used in electron microscopy is to be published separately.

Examination of the micrographs published by Vandervoort and Washburn (1960) shows that, in specimens prepared from material annealed at 150°C, the loop density is considerably smaller than the loop density in as-quenched material and, moreover, that the loops which remain after annealing are often considerably larger than those found, on the average, in the as-quenched material. In particular, a number of pairs of loops are observed. The distance between the members of such a pair is commonly smaller than the diameter of either loop. This effect is particularly evident in fig. 7 of Vandervoort and Washburn's paper. From these observations the following conclusions have been drawn.

Fig. 1

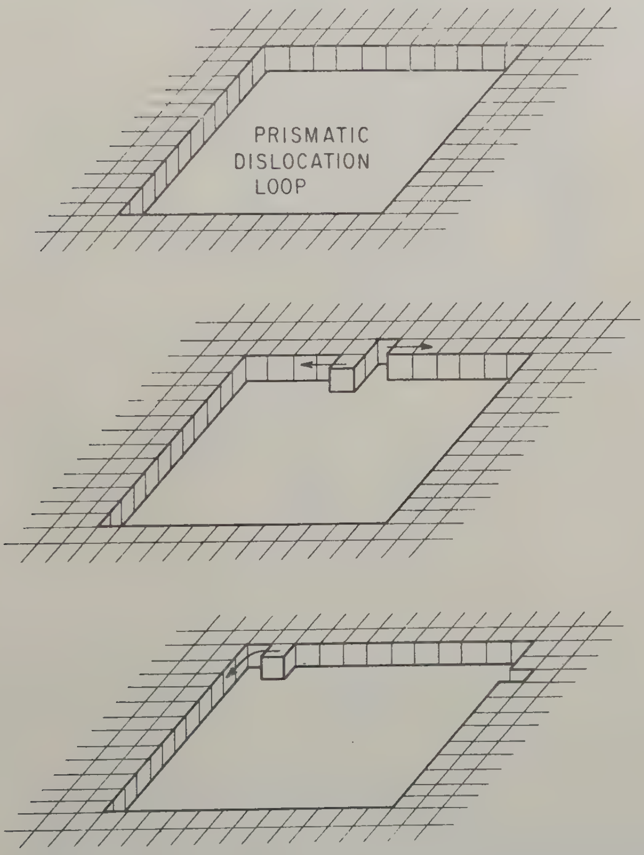

Formation and migration of defects involved in self-climb.

1. The coalescence of loops does not seem to be due to vacancy diffusion through the matrix. It is extremely difficult, for example, to understand how loops which are separated by distances such as those observed in the as-quenched material could have coalesced by diffusion through the matrix while some loops which are very near one another remained intact.

2. The self-climb mechanism can satisfactorily explain these observations. If this process controls the behaviour of loops during annealing, loops remain substantially intact until they finally merge, and this is consistent with the microscopic evidence.

Fig. 2

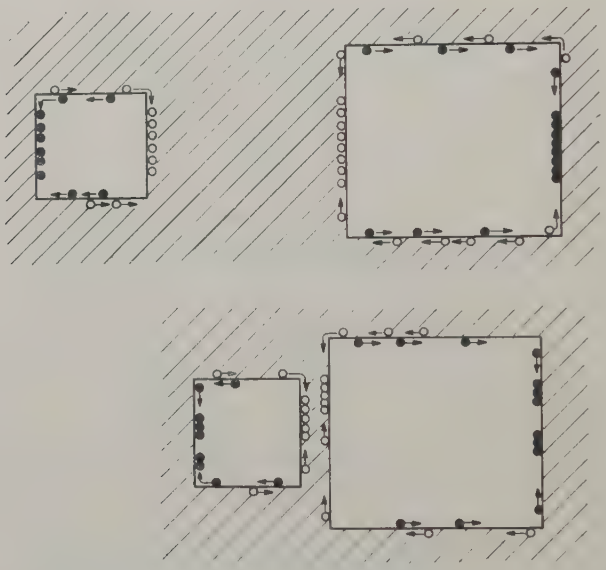

Successive stages in the coalescence of two coplanar loops by self-climb. The filled circles represent diffusing atoms and the open circles diffusing vacancies.

However, another point must be considered, namely, whether the closely coupled pairs observed were just about to coalesce, or whether there are cogent reasons why they could not merge completely.

It is possible for a vacancy plate on the (111) plane in a face-centred cubic metal to collapse in two different ways, depending on whether or not the atom planes above and below the plane of the plate are sheared along a direction lying in the plane of the plate as they come together. If no shear takes place, then Burgers vector of the resultant dislocation loop will be $(a/3)[111]$ and the loop will contain a stacking fault since the stacking sequence normal to the plane of the loop is ABCACABC.... No stacking faults were observed in the specimens examined by Vandervoort and

Washburn or by Silcox and Whelan. If, on the other hand, the atom planes above and below the plane of the vacancy plate are displaced with respect to one another as they come together by one of the shears $(a/6)[11\bar{2}]$, $(a/6)[\bar{2}11]$, $(a/6)[1\bar{2}1]$, then the stacking sequence will be the normal ABCABCA . . . so that the loop will not contain a fault, and the slip vector of the resulting loop will be $(a/2)[110]$, $(a/2)[011]$, or $(a/2)[101]$.

These slip vectors are translation vectors of the face-centred cubic lattice so that a dislocation loop having any of these three slip vectors can glide on a cylindrical surface inclined to the plane of the loop and containing (as the generators of the cylinder) the slip vector of the loop. However, in general not all parts of such a loop will be able to slip easily on this cylindrical surface since the surface will not be entirely composed of close-packed $\{111\}$ planes. Such a situation is shown in fig. 4 (*a*), in which the $[1\bar{1}0]$ segments of the loops can only slip on (001), while the segments oriented along $[\bar{1}01]$ and $[0\bar{1}1]$ slip readily on the close-packed $\{111\}$ planes. Since hexagonal loops corresponding to the configuration of fig. 4 (*a*) have often been found in foils, it is of interest to examine the possibility of slip on (001). Boas and Schmid (1931) have observed that macroscopic slip can occur on $\{100\}$ planes in aluminium at temperatures above 400°C. It is possible that the attractive force between the neighbouring $[1\bar{1}0]$ segments might be high enough to cause them to combine by slip on (001) even at temperatures as low as 150°C.

Fig. 3

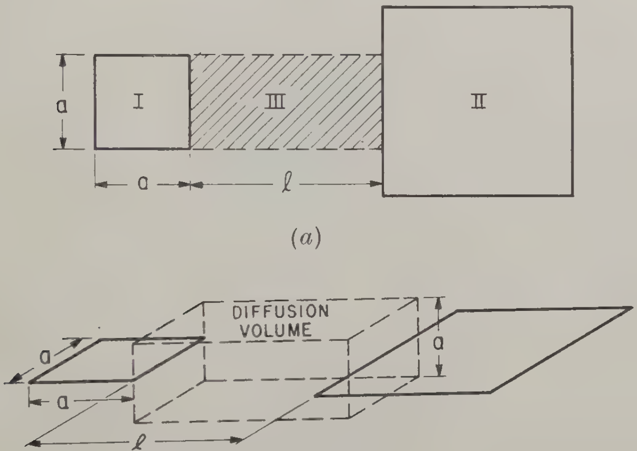

(*a*)

(*b*)

Geometries for calculating rates of loop coalescence.

(*a*) Geometry for coalescence of coplanar loops by self-climb. The areas I and II are the interiors of the loops.
(*b*) Geometry for coalescence of loops by bulk diffusion.

For the geometry of fig. 4 (*a*), where both loops have the same Burgers vector, the stress between the neighbouring $[1\bar{1}0]$ segments of the loops is

$$\sigma = \frac{\mu|b|}{2\pi(1-\nu)}\left(\frac{1}{\sqrt{2}d}\right)$$

where μ is the shear modulus, ν is Poisson's ratio, $|b|$ is the magnitude of the slip vector, and d is the distance between the respective (111) planes on which the loops lie. To estimate the magnitude of this stress it is necessary to make some estimate of the value of d. Bearing in mind that the foils used by Vandervoort and Washburn and Silcox and Whelan were of the order of 1000 Å thick it seems reasonable to choose $d \sim 200$ Å. Then $\sigma \sim 5 \times 10^8$ dynes/cm^2; this is roughly one hundred times as great as the macroscopic shear stress at which glide begins on {111} in aluminium. Since Boas and Schmid (1931) found {100} slip at 400°c under conditions for which the shear stress on planes of the {100} type was only slightly larger than the shear stress acting on planes of the {111} type, the possibility of inducing {100} slip at 150°c by a stress one hundred times higher than that required for {111} slip cannot be discounted.

Fig. 4

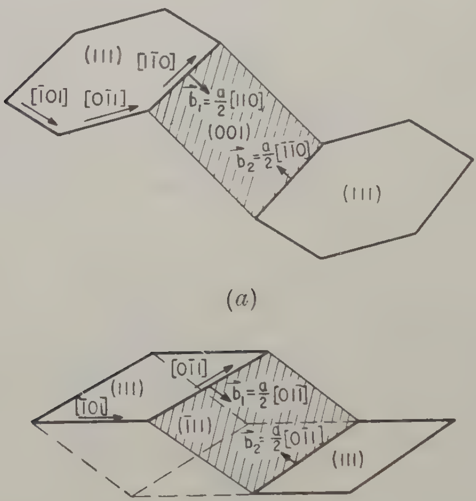
(111)
$[1\bar{1}0]$
$[\bar{1}01]$
$[0\bar{1}1]$
$\vec{b}_1 = \frac{a}{2}[110]$
(001)
$\vec{b}_2 = \frac{a}{2}[\bar{1}\bar{1}0]$
(111)
$[0\bar{1}1]$
(111)
$[\bar{1}01]$
$\vec{b}_1 = \frac{a}{2}[01\bar{1}]$
$(\bar{1}11)$
$\vec{b}_2 = \frac{a}{2}[0\bar{1}1]$
(111)

(*a*)

(*b*)

Coalescence of loops on parallel (111) planes by prismatic glide.

(*a*) Combination of non-coplanar hexagonal loops.
(*b*) Combination of loops capable of easy prismatic glide.

Prismatic glide of hexagonal dislocation loops has been observed by Hirsch *et al.* (1958). The observations were made on thin foils of quenched aluminium at temperatures lower than 100°c and provide strong experimental evidence for glide on {100} planes at ordinary temperatures.

As shown in fig. 4 (*b*), it is possible to construct a loop all parts of which are oriented for easy slip on close-packed planes. Non-coplanar loops of this type can readily coalesce by self-climb followed by prismatic glide on {111} planes.

Fig. 5

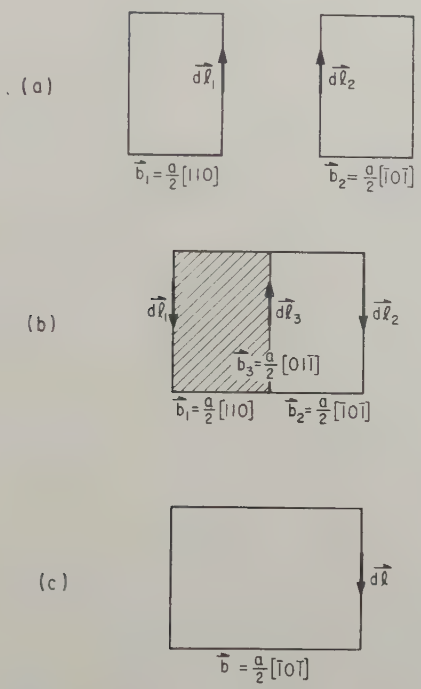
(a)
$\vec{d\ell}_1$
$\vec{d\ell}_2$
$\vec{b}_1=\frac{a}{2}[110]$
$\vec{b}_2=\frac{a}{2}[\bar{1}0\bar{1}]$
(b)
$\vec{d\ell}_1$
$\vec{d\ell}_3$
$\vec{d\ell}_2$
$\vec{b}_3=\frac{a}{2}[01\bar{1}]$
$\vec{b}_1=\frac{a}{2}[110]$
$\vec{b}_2=\frac{a}{2}[\bar{1}0\bar{1}]$
(c)
$\vec{d\ell}$
$\vec{b}=\frac{a}{2}[\bar{1}0\bar{1}]$

Successive stages in the coalescence of coplanar loops on (111) with different Burgers vectors. The dislocation segment formed at the intersection of the loops sweeps over the shaded area in (*b*).

Coplanar loops having different slip vectors combine as shown in fig. 5. A segment of total dislocation is formed by the reaction

$$(a/2)[110]+(a/2)[\bar{1}0\bar{1}]\rightarrow(a/2)[01\bar{1}]$$

where the loops join. The glide plane of this segment is the plane of the loops themselves. The segment sweeps over the interior of one or the other of the two loops and combines with the dislocation bounding this loop according to the reaction

$$(a/2)[01\bar{1}]+(a/2)[\bar{1}\bar{1}0]\rightarrow(a/2)[\bar{1}0\bar{1}],$$

so that the slip vector of the resulting large loop is the slip vector of the 'unswept' small loop.

§ 2. KINETICS OF LOOP COMBINATION

In the following section the kinetics of loop coalescence by bulk diffusion and by self-climb will be examined and compared. Rates of coalescence for loops having the size and separation typical of as-quenched aluminium will be estimated, and the observations of Vandervoort and Washburn (1960) will be used to derive an approximate value of the activation energy for diffusion along a dislocation line in aluminium.

Figure 1 shows that the creation of an atom capable of diffusing rapidly in the core of the dislocation loop is accompanied by the creation of a vacancy on the periphery of the loop. Coalescence of neighbouring loops by self-climb requires the diffusion of atoms along the loop cores to the farther edges of the loops and the diffusion of vacancies along the loops to the closer edges; thus, the loops approach one another by the transport of material around each loop from the closer to the farther edge. Although a diffusing atom is effectively constrained to remain in the core of a loop by its strong repulsive interaction with the atoms surrounding the core, a vacancy can diffuse away from the periphery of the loop into the matrix. It is this possibility of evaporation of vacancies from a loop which leads to the coalescence of loops by bulk self-diffusion.

There are, however, two factors which argue against the evaporation of vacancies from the periphery of the loop. The first is that a vacancy created on the periphery of a dislocation loop must acquire an additional increment of energy to escape from the stress field of the loop. The second is that the rate of migration of a vacancy along the periphery of a dislocation loop should be much more rapid than the rate of migration away from the loop. In the absence of experimental values for the energy binding a vacancy to the compression side of a dislocation, and the activation energy for migration along a dislocation line, it is not possible to calculate the probability that a vacancy will escape from the periphery of a dislocation loop before it can diffuse along the loop and add to an incomplete row of vacancies. However, since the energy barrier a vacancy must surmount in diffusing away from the loop is an appreciable fraction of the difference between the activation energies for bulk diffusion and diffusion along a dislocation line, the probability of evaporation from the loop is small at temperatures below about 150°c.

The rate of transport of material from a source to a sink by means of diffusion is determined by the rate at which an individual carrier moves from source to sink and the number of carriers in the region in which diffusion is taking place. If it is assumed that the number of vacancies in the diffusion region is fixed (e.g. by requiring that thermodynamic equilibrium be maintained) then the number of vacancies diffusing from source to sink in time τ is

$$n = N(\tau/t) \qquad . \quad . \quad . \quad . \quad . \quad . \quad . \quad . \quad (1)$$

where N is the number of vacancies in the diffusion region and t is the average time required for a vacancy to diffuse from source to sink.

In calculating the rate of coalescence of two neighbouring loops by either the bulk self-diffusion process or the self-climb process, it will be assumed that the initial concentration of vacancies is the concentration present in thermodynamic equilibrium at the annealing temperature, and that this concentration is maintained as the loops coalesce.

If

U_{f} = the formation energy of a vacancy in perfect crystal,

U_{m} = the activation energy for migration of a vacancy in perfect crystal,

U_{f}' = the formation energy of a vacancy-atom defect pair capable of diffusing along a dislocation line,

U_{m}' = the activation energy for migration along a dislocation line,

then $U=U_{\mathrm{f}}+U_{\mathrm{m}}$ is the activation energy for bulk self-diffusion and $U'=U_{\mathrm{f}}'+U_{\mathrm{m}}'$ is the activation energy for self-diffusion along a dislocation line.

The time required for the coalescence of the two loops shown in fig. 3 will be calculated for the bulk diffusion process and for self-climb. For convenience one of the loops has been assumed to be much larger than the other, with the smaller loop having side a and the separation of the loops being l.

§ 3. BULK DIFFUSION

On the basis of the bulk diffusion process it is to be expected that the smaller loop will shrink by evaporation of the $(a/a_0)^2$ vacancies from which it was formed, a_0 being the lattice constant of the crystal. These vacancies diffuse to the larger loop, causing to it grow. Referring to fig. 3, the distance these vacancies must diffuse is approximately l. Assuming a random walk, the average time taken for a vacancy to diffuse from the smaller to the larger loop is therefore

$$t \simeq \frac{l^2}{a_0{}^2\,\nu_0} \exp\left\{\frac{U_{\mathrm{m}}}{kT}\right\}. \qquad (2)$$

where ν_0 is the vibrational frequency of the lattice. The volume in which diffusion is taking place is assumed to be approximately a^2l, so that the number of vacancies in the diffusion region is

$$N \simeq \frac{a^2 l}{a_0{}^3} \exp\left\{-\frac{U_{\mathrm{f}}}{kT}\right\}. \qquad (3)$$

Substituting t from eqn. (2) and N from eqn. (3) in eqn. (1) yields, for the time τ required for the loops to coalesce,

$$\tau = \frac{N}{nt} \simeq \frac{l}{a_0\nu_0} \exp\left\{\frac{U_{\mathrm{f}}+U_{\mathrm{m}}}{kT}\right\} = \frac{l}{a_0\nu_0} \exp\left\{\frac{U}{kT}\right\}. \qquad (4)$$

§ 4. Self-climb

If the loops of fig. 3 coalesce by self-climb then both will move; however, due to the longer diffusion path around the larger of the two loops and the greater amount of material which must be transported around it, this loop will move much more slowly than the small one. Motion of the larger loop will therefore be neglected.

The diffusion path around the periphery of the small loop is approximately $2a$ in length. Assuming random walk and the same value ν_0 for the atomic vibration frequency, the average time required for the transport of an atom from the near to the far side of the loop is

$$t' \simeq \frac{4a^2}{4\nu_0 a^2} \exp\left\{\frac{U_{\mathrm{m}}'}{kT}\right\}. \qquad (5)$$

In order for the loops to coalesce, all the material in region III of fig. 3 must be transported around the loop so that if the quantities important in the self-climb process are denoted by affixing primes to the corresponding symbols in eqn. (1), then $n' \simeq al/a_0^2$. The number of atom-vacancy pairs present on the loop in thermodynamic equilibrium is

$$N' \simeq \frac{4a}{a_0} \exp\left\{-\frac{U_{\mathrm{f}}'}{kT}\right\} \qquad (6)$$

so that from (1), (5) and (6), the time required for the loops to coalesce is

$$\tau' = \frac{n't'}{N'} \simeq \frac{a^2 l}{a_0^3 \nu_0} \exp\left\{\frac{U_{\mathrm{f}}' + U_{\mathrm{m}}'}{kT}\right\} = \frac{a^2 l}{a_0^3 \nu_0} \exp\left\{\frac{U'}{kT}\right\}. \qquad (7)$$

§ 5. Comparison with Experimental Results

In the as-quenched material studied by Vandervoort and Washburn, the dislocation loops found were about 200–500 Å in size, and were separated by distances ranging from 1000 Å to 5000 Å. Bradshaw and Pearson (1957) have found $U = 1{\cdot}20$ ev for aluminium; the value of U' is not known. A reasonable estimate for the atomic vibration frequency is $\nu_0 \simeq 10^{13}$/sec.

Using the values $a = 300$ Å, $l = 3000$ Å, $\nu_0 \simeq 10^{13}$/sec, $U = 1{\cdot}20$ ev, $a_0 = 2{\cdot}86$ Å, and various values of U', the times τ and τ' have been calculated according to eqns. (4) and (7) for the temperature range of interest. These values are listed in the table.

Since Vandervoort and Washburn found considerable loop growth following ten minute (6×10^2 sec) anneals at 150°c, inspection of the times listed in the table shows that:

1. Bulk diffusion cannot account for the loop growth observed.

2. Self-climb occurring with an activation energy of about 0·7 ev does account for the observations.

3. Since the time τ' is much more sensitive to the value of U' than it is to the geometrical factors in eqn. (7), the uncertainty in the value of U' thus determined is relatively small.

4. This value of U' is consistent with the lowering of the activation energy for short-circuit diffusion processes that has been observed in other metals.

Approximate time required for combination of dislocation loops of diameter 300 Å, separated by 3000 Å

Temperature (°c)	Time required for combination of loops			
	Bulk diffusion ($U = 1{\cdot}20$ ev)	Self-climb		
		$U' = 0{\cdot}6$ ev	0·7 ev	0·8 ev
	Seconds			
100	$1{\cdot}6 \times 10^6$	125	2900	$6{\cdot}5 \times 10^4$
125	$1{\cdot}6 \times 10^5$	40	740	$1{\cdot}4 \times 10^4$
150	$2{\cdot}0 \times 10^4$	14	220	3400
175	3200	5·6	75	1000
200	620	2·5	29	340

§ 6. CONCLUSIONS

1. The coalescence of quenched-in dislocation loops in aluminium takes place by short-circuit diffusion around the periphery of each loop.
2. The activation energy for this short-circuit diffusion process is about 0·7 ev. (The measured value for the activation energy for diffusion through the aluminium lattice is 1·20 ev.)

ACKNOWLEDGMENTS

The author wishes to express his appreciation to the Office of Naval Research for financial support, and to Professor E. R. Parker and Dr. L. Himmel for invaluable assistance in the presentation of the material. He would also like to thank Drs. G. Thomas, R. de Wit and J. Nadeau for many very helpful discussions.

REFERENCES

BOAS, W., and SCHMID, E., 1931, *Z. Phys.*, **71,** 703.
BRADSHAW, F. J., and PEARSON, S., 1957, *Phil. Mag.*, **2,** 570.
HENDRICKSON, A., and MACHLIN, E. S., 1954, *Trans. Amer. Inst. min. (metall.) Engrs*, **156,** 82.
HIRSCH, P. B., SILCOX, J., SMALLMAN, R. E., and WESTMACOTT, K. H., 1958, *Phil. Mag.*, **3,** 897.
HOFFMAN, R. E., and TURNBULL, D., 1951, *J. appl. Phys.*, **22,** 634.
KUHLMANN-WILSDORF, D., 1958, *Phil. Mag.*, **3,** 125.
SILCOX, J., and WHELAN, M. J., 1960, *Phil. Mag.*, **5,** 1.
TURNBULL, D., and HOFFMAN, R. E., 1954, *Acta Met.*, **2,** 419.
VANDERVOORT, R., and WASHBURN, J., 1960, *Phil. Mag.*, **5,** 24.

The Magnetic Susceptibility of Vanadium–Chromium Solid Solutions†

By B. G. Childs, W. E. Gardner and J. Penfold
Atomic Energy Research Establishment, Harwell, Berks

[Received July 7, 1960]

Abstract

The magnetic susceptibilities of a number of solid solutions of chromium in vanadium have been measured at 20°, 77° and 293°K. The susceptibility at 20°K decreases with concentration from a value of 300×10^{-6} e.m.u./g atom for pure vanadium to 159×10^{-6} e.m.u./g atom for pure chromium. Fine structure is observed in several regions of the susceptibility–composition curve. The temperature dependence of the susceptibility of all the alloys investigated was small.

An interpretation of the susceptibility behaviour is given in terms of the collective electron model.

§ 1. Introduction

Magnetic susceptibility measurements can increase our understanding of the electronic band structure of metals and alloys. This applies especially to non-ferromagnetic transition metals—from which we have chosen vanadium—since a large part of their susceptibility is determined by the density of states of the conduction electrons at the Fermi level.

The most important property of vanadium, however, which led to its selection for the present investigation is its ability to dissolve appreciable amounts of the majority of the transition elements in its own period. The concentration ranges (in atomic per cent) over which these elements form stable primary solutions with vanadium are (Rostoker 1958): titanium 0–70, chromium 0–100, manganese 0–50, iron 0–30, cobalt 0–8, nickel 0–8 and copper 0–7. A comparison of the results for such vanadium alloys should, in principle, distinguish the effects of atomic concentration and electron transfer on the Fermi level and the shape of the conduction band.

In this paper we report the results of magnetic susceptibility measurements for solid solutions of chromium in vanadium. Subsequently we will compare these results with those for the other alloy systems.

§ 2. Preparation of the Specimens

The vanadium and chromium used for the alloys were obtained from a number of sources, purer materials being used during the course of the work as they became available. No systematic dependence of susceptibility upon the purities of these source materials was found for vanadium or the vanadium-rich alloys containing up to about 30 at. % chromium. This was not the case, however, for chromium and so the chromium-rich alloys, which were all prepared towards the end of the investigation, were made using only the purest materials.

---

† Communicated by the Authors.

The suppliers of the vanadium were Johnson, Matthey and Company (J.M.), the Battelle Memorial Institute (B.M.I.) and the U.S. Bureau of Mines (U.S.B.M.). The methods of preparation and the purities (non-metallic elements being included in the analyses), were:

J.M.:	calcium reduction of vanadium pentoxide (99·63 weight %),
U.S.B.M.:	electrolytic refinement of vanadium metal (99·85 weight %),
B.M.I.:	Van Arkel process from vanadium iodide (99·92 weight %).

Detailed analyses have been given in an earlier paper (Childs *et al.* 1959 referred to henceforth as I).

The chromium was provided by Johnson, Matthey and Company (99·65 weight %) and the Fulmer Research Institute (99·99 weight %). The latter material (F.R.I.) had been hydrogen-reduced to lower its oxygen content to 0·0032 weight %.

Alloy buttons of about 3 g weight were prepared by melting together appropriate amounts of vanadium and chromium in an argon-arc furnace. The buttons, which were supported on a water-cooled copper hearth, were inverted and remelted a number of times so as to ensure adequate mixing of the two components. Contamination by oxygen or nitrogen during these melting operations was minimized by frequent gettering of the argon atmosphere with molten zirconium. A leak test on the apparatus was made before melting was begun.

After melting, the buttons were annealed, both to reduce small-scale concentration fluctuations caused by segregation on solidification of chromium-rich material, and to promote the formation of a random solid solution. Each button, supported on a plate of purified thoria, was sealed in an argon-filled silica tube and heated by high-frequency induction for one hour at 1600°c. A leak test and argon gettering operation was performed before the annealing.

The density and hardness (§ 3) of the button were then measured, after which susceptibility specimens approximately $8 \times 1{\cdot}5 \times 1{\cdot}5$ mm in size were cut from its centre using a clean Carborundum slitting wheel. A stream of coolant liquid (a water-oil emulsion) prevented excessive heating and oxidation of the specimens during this process. The specimens were finally degreased in alcohol, cleaned in dilute hydrochloric acid and washed in distilled water.

§ 3. Examination of the Alloys

Before a specimen was accepted for susceptibility measurement it was carefully examined in order to determine whether its composition, homogeneity and purity were satisfactory. This involved the following procedure.

3.1. *Composition*

The composition of each alloy button was determined from the initial weights of its constituents after correcting for the loss in weight which occurred on melting. The loss in weight, which was usually small, was assumed to be due almost entirely to chromium evaporation since the vapour pressure of chromium below 2000°c is more than one thousand times that of vanadium.

These composition values were confirmed for certain selected specimens by direct chemical analysis.

Fig. 1

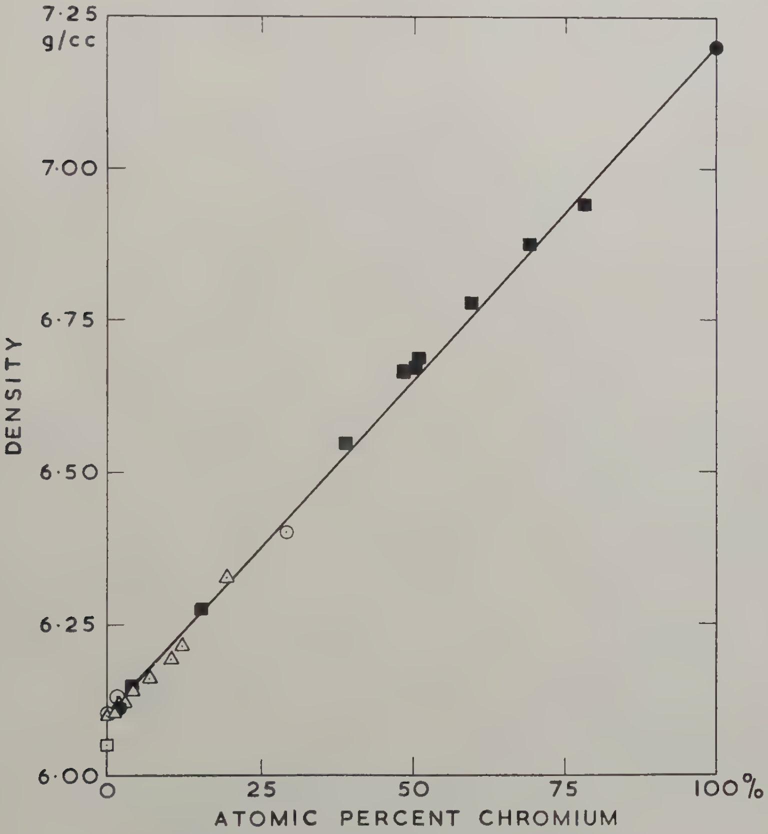

Variation in density with composition for the vanadium–chromium system.

- △ alloys of J.M. vanadium and J.M. chromium;
- ○ alloys of B.M.I. vanadium and J.M. chromium;
- ● alloys of B.M.I. vanadium and F.R.I. chromium;
- ■ alloys of U.S.B.M. vanadium and F.R.I. chromium.

The final composition values are estimated to be correct to within either ±0·5 at. % chromium or ±2% of the quoted chromium content, whichever is the lesser.

3.2. *Density*

The density of each annealed button was measured at room temperature using the standard water displacement method. The variation in density with composition for the vanadium–chromium solutions is shown in fig. 1. Within the accuracy of measurement the density values for all the specimens fall on a common curve.

The density values served as a further check on composition. They were also used (§ 6.3) in estimating the effects on the susceptibility values of changes in the interatomic spacing.

Fig. 2

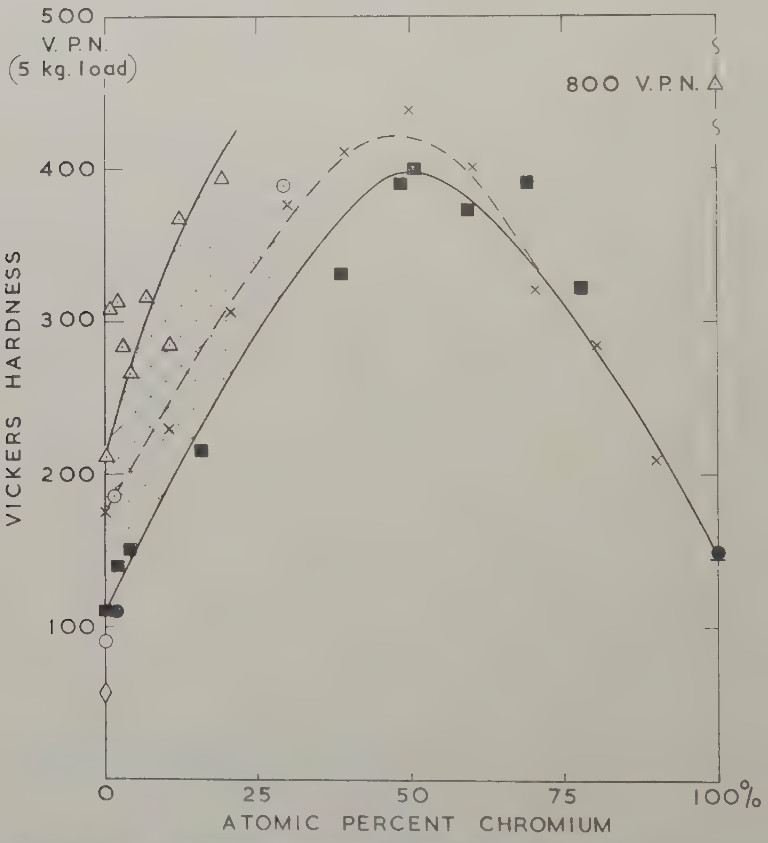

Hardness of the vanadium chromium alloys as a function of composition.

△ alloys of J.M. vanadium and J.M. chromium;
○ alloys of B.M.I. vanadium and J.M. chromium;
● alloys of B.M.I. vanadium and F.R.I. chromium;
■ alloys of U.S.B.M. vanadium and F.R.I. chromium.
◇ S.E.R.L., Baldock, vanadium.
× Aeronautical Research Laboratories, Melbourne, chromium.
×– – –× Carlson and Eustice (1959).

3.3. *Hardness*

After measuring its density the button was cut in half and the cut surface of one piece polished. The Vickers hardness of this piece was then measured at a number of points across the surface.

Any large-scale variation in concentration across the specimen (which was never found) would have produced a corresponding variation in hardness, whereas excessive contamination throughout the specimen (for example by oxygen) could be detected by the resulting high average hardness.

Figure 2 shows the hardness of a number of specimens as a function of their chromium concentration. Also plotted in this figure are hardnesses for vanadium, reported in I, and some additional values obtained from the results of Carlson and Eustice (1959). Their published results have been converted from Rockwell A to Vickers hardness values by Dr. O. N. Carlson (private communication).

The hardness of alloys prepared from the purest material—B.M.I. or U.S.B.M. vanadium and F.R.I. chromium—increased from about 90 VPN for pure vanadium to 400 VPN for 50% chromium. It then fell to 150 VPN for pure chromium. The hardness values of the alloys prepared from the less pure materials occupied a band approximately 150 VPN wide above the base curve.

3.4. *Microstructure*

The polished and etched surfaces of the buttons were examined at high magnification (× 500) for traces of foreign material dispersed as a precipitate or in other form. Most of the specimens, in fact, contained such a dispersion usually as a fine filamentary network within the grains with, in some cases, isolated particles distributed at intervals along the grain boundaries. Typical micrographs (× 250) of the alloys are reproduced in fig. 3 (Pl. 165).

The precipitate is presumably associated with the impurities initially present in the alloy constituents since its volume was generally much less for alloys made from the purest materials. Experiments with aged specimens (see § 5) showed, at least for the vanadium-rich alloys, that the susceptibility was not significantly altered unless the precipitate occupied more than one volume percent of the specimen. Such specimens were therefore rejected.

§ 4. SUSCEPTIBILITY MEASUREMENT

The method used to measure the susceptibility of the specimens has been described previously (Childs and Penfold 1957). The measurements were made using a Sucksmith ring balance to an estimated accuracy of ± 1% relative to the susceptibility of tantalum ($0{\cdot}849 \times 10^{-6}$ e.mu./g) as standard. The apparatus was frequently re-calibrated during the course of the work. The measurements were made at three temperatures, 20°, 77° and 293°K.

§ 5. Results

The mass susceptibility values are given in full in the table. This table includes some results for a pure vanadium sample (S.E.R.L.) which were not reported in I. This specimen was produced by the Van Arkel process and further refined by zone-melting at S.E.R.L. Baldock. The exceptionally low hardness of the specimen (57 VPN) indicated that its purity was greater than that of any other vanadium sample investigated.

The mass susceptibilities of vanadium–chromium solid solutions

Chromium concentration	Source		$\chi_m \times 10^6$ e.m.u./g at		
at. %	Vanadium	Chromium	20°K	77°K	293°K
0	J.M.	—	5·94	5·96	5·83
0	U.S.B.M.	—	5·83	5·86	5·77
0	B.M.I.	—	5·89	5·88	5·81
0	S.E.R.L.	—	5·92	5·95	5·86
1·00	J.M.	J.M.	5·87	5·83	5·63
1·57	B.M.I.	J.M.	5·64	5·67	5·55
1·91	B.M.I.	F.R.I.	5·59	5·62	5·51
1·96	J.M.	J.M.	5·64	5·63	5·57
1·96	U.S.B.M.	F.R.I.	5·46	5·50	5·37
2·84	J.M.	J.M.	5·64	5·64	5·57
3·90	U.S.B.M.	F.R.I.	5·82	5·72	5·64
4·00	J.M.	J.M.	5·74	5·68	5·75
6·9	J.M.	J.M.	5·62	5·63	5·54
10·5	J.M.	J.M.	5·65	5·63	5·57
12·2	J.M.	J.M.	5·30	5·30	5·27
15·3	U.S.B.M.	F.R.I.	5·27	5·28	5·26
19·2	J.M.	J.M.	5·49	5·45	5·43
29·1	B.M.I.	J.M.	5·05	5·04	5·02
38·5	U.S.B.M.	F.R.I.	4·84	4·79	4·79
48·8	U.S.B.M.	F.R.I.	4·88	4·90	4·76
50·0	U.S.B.M.	F.R.I.	4·79	4·81	4·73
50·5	U.S.B.M.	F.R.I.	4·91	4·89	4·76
59·5	U.S.B.M.	F.R.I.	4·04	4·04	4·04
69·2	U.S.B.M.	F.R.I.	3·51	3·51	3·58
77·8	U.S.B.M.	F.R.I.	3·27	3·17	3·23
100·0	—	J.M.	3·38	3·47	3·40
100·0	—	F.R.I.	3·01	2·99	3·19
100·0	—	A.R.L.	2·99	2·98	3·17

The estimated absolute accuracy of χ_m is $\pm 0{\cdot}10 \times 10^{-6}$ e.m.u./g.

The atomic susceptibilities at 20°K are shown as a function of the chromium concentration in fig. 4. Also included in this figure are some results obtained by Lingelbach (1958) at 100°K for alloys of high chromium concentration.

The suceptibility at 20°K decreases with concentration in an oscillatory manner up to 50 at. % of chromium and then falls sharply. Thus there are small minima at 2 and 15 at. %, with maxima at 6 and 20 at. % chromium. In addition there is a broad minimum at 32 at. % and a relatively broad maximum at 50 at. % chromium.

Fig. 4

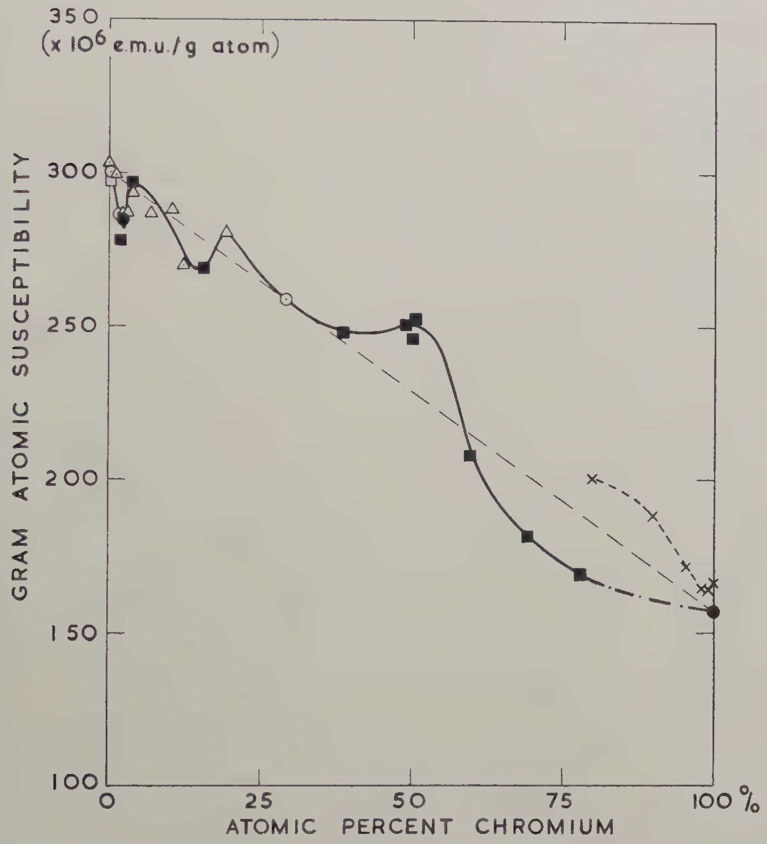

Atomic susceptibility at 20°K for the vanadium-chromium system as a function of composition.

- △ alloys of J.M. vanadium and J.M. chromium;
- ⊙ alloys of B.M.I. vanadium and J.M. chromium;
- ● alloys of B.M.I. vanadium and F.R.I. chromium;
- ■ alloys of U.S.B.M. vanadium and F.R.I. chromium.
- × Lingelbach (1958) 100°K.

In order to confirm this fine structure several alloys were investigated having compositions of about 2 at. % chromium and 50 at. % chromium. Four separate specimens having a nominal 2 at. % were prepared from various combinations of the vanadium and chromium source materials to determine whether this minimum was a genuine alloy effect unconnected with the presence of small amounts of impurites. The hardnesses of these specimens ranged from 110-314 VPN yet, as shown in the figure, their susceptibility values are grouped closely together and show no systematic dependence on hardness or on the purity of the source material. This satisfactory agreement suggested that it was not unreasonable to continue the curve through all our observed points and so obtain the rest of the fine structure.

The relatively broad maximum at 50 at. % chromium may be associated with the development of long-range order in this alloy. To test this possibility two specimens were prepared from buttons which were quenched rapidly from 1900°c to room temperature—the normal 1600°c annealing stage, followed by a relatively slow cooling of the alloy, being omitted. The susceptibility of these quenched specimens was the same, within experimental error, as that of the annealed and slowly cooled specimen. Thus ordering, if it occurs, must reach equilibrium in a period of less than a few seconds.

Some further evidence on this point was provided by a neutron diffraction study of the annealed specimen. No significant superlattice line (100) associated with the ordered state was detected. From an estimate of the errors of measurement it was concluded that the amount of long-range order present must be less than 10%. This result is expected since the proximity of vanadium and chromium in the electrochemical series and their similar atomic sizes do not energetically favour ordering.

Since the major emphasis in this work was on the behaviour of vanadium as a solvent metal no attempt was made to investigate the susceptibility variation for concentrations above 78 at. % chromium. However Lingelbach's (1958) results, some recent resistivity data (§ 6) and electronic specific heat measurements of Wei, Cheng and Beck (private communication) show that further fine structure in this region of the susceptibility curve may be expected.

The variation in susceptibility (table) between 20° and 293°K for all the alloys was very small and not appreciably dependent on concentration. On the average the susceptibility decreased by 1% over this temperature range. The absence of any strong temperature dependence for the 78 at. % chromium alloy is noteworthy since, for an 80 at. % chromium specimen, Lingelbach found the susceptibility to drop from 227×10^{-6} e.m.u./g atom at 66°K to 180×10^{-6} e.m.u./g atom at 293°K—a 20% variation. In view of the lack, in our results, of any systematic trend in the temperature coefficient of susceptibility between 0 and 78% chromium, it seems likely that this particular specimen of Lingelbach's was impure.

As mentioned earlier, the susceptibility of the J.M. chromium differed appreciably from that of the F.R.I. material, the values at 293°K being 177 and 166×10^{-6} e.m.u./g atom respectively. A third chromium sample, obtained from the Aeronautical Research Laboratories, Melbourne, which also contained only 0·003 weight % oxygen, had a susceptibility (165×10^{-6} e.m.u./g atom at 293°K) close to that of the F.R.I. sample. The higher value for the J.M. specimen is presumably due to the 0·37 weight % of impurity—mostly oxygen—contained in it.

In the case of vanadium and of the alloys with up to 30 at. % chromium, excessive contamination by oxygen and nitrogen (introduced either deliberately or by accidental mishandling during preparation) caused the susceptibility to decrease. This behaviour, which is opposite to that shown by chromium, has been mentioned in I for a sample of pure vanadium. This specimen decreased in susceptibility from 296 to 244×10^{-6} e.m.u./g atom on solution of 7 weight % of oxygen.

No significant difference was found between the susceptibility values for specimens prepared from the different source materials and having hardness values between the two curves shown in fig. 2. Samples with hardnesses much above the upper curve gave anomalously low susceptibility values and were rejected.

Some specimens which had, after the initial measurements, been allowed to stand at room temperature for more than one year showed an ageing effect whereby the susceptibility decreased with time. One such specimen—the 10·5 at. % chromium sample—decreased in susceptibility from 284 to 273×10^{-6} e.m.u./g atom at 293°K after 28 months. Removal, by etching, of a surface layer $1{\cdot}4 \times 10^{-3}$ cm thick did not affect the susceptibility of the specimen, thus indicating that the ageing process is a volume rather than a surface effect. This was confirmed by cutting a new specimen from the middle of one of the halves of the original alloy button. This new specimen had, within experimental error, the same diminished susceptibility.

This effect is presumably connected with impurity precipitation since, while the 10·5 at. % alloy originally appeared on metallographic examination perfectly free from inclusions—the grain boundaries being sharp and fine—re-examination after ageing revealed the presence of a substantial quantity of precipitate distributed preferentially along the grain boundaries but also throughout the grains.

§ 6. Discussion

Before attempting to explain the variation with composition of the alloy susceptibilities, it is necessary to consider which of many conceivable magnetic processes contribute appreciably to the susceptibilities of the pure component metals.

6.1. *Vanadium Metal*

For vanadium the major contribution to the susceptibility most probably comes from the spin paramagnetism of the outer electrons (five per atom). If any of these electrons were in localized atomic-like orbitals then, from Hund's rule, their spins would necessarily be parallel. In consequence each atom would show a permanent magnetic moment, However, the results of neutron diffraction measurements made at 20°K by Shull and Wilkinson (1953) show that, within the limits of experimental error (0·1 Bohr magneton), there are no such moments, aligned or unaligned, on the vanadium atoms. All the outer electrons must therefore be in non-localized states in the conduction band of the metal where they will give rise to a Pauli-type paramagnetism.

Conduction electrons, if mutally non-interacting, contribute a term to the susceptibility per gram atom (Pauli 1927) given by

$$\chi_p = 2\beta^2 N n(E_0)$$

where N is Avogadro's number and β the Bohr magneton. $n(E_0)$, the density of states for one direction of spin per unit energy range per atom at the Fermi surface, may also be expressed by the relation (Mott and Jones 1936)

$$n(E_0) = \frac{3\gamma}{2\pi^2 k^2 N}$$

where k is Boltzmann's constant and γ is the temperature coefficient of the electronic specific heat per gram atom. Substituting for γ the value $8{\cdot}8 \times 10^{-3}$ J/g atom deg^2 obtained by Corak *et al.* (1954), we find that for vanadium $n(E_0) = 1{\cdot}86$ states/ev atom. The Pauli susceptibility for vanadium is thus 122×10^{-6} e.m.u./g atom. The observed value (χ_0) at 20°K, corrected (see later) for diamagnetic terms is 308×10^{-6} e.m.u./g atom.

Such a large difference between χ_0 and χ_p is not peculiar to vanadium but is observed in all transition metals. It has been attributed (e.g. Mott 1935) to a spin-interaction of a ferromagnetic nature between the conduction electrons. This 'exchange interaction' tends to increase the unbalance produced by the field in the number of parallel and anti-parallel electron spins and hence to increase the induced moment.

If we write (Stoner 1936)

$$\frac{1}{\chi_0} = \frac{1}{\chi_p} - K$$

then K, which is proportional to the exchange interaction, has a value for vanadium of 5000 g atom/e.m.u.

There are two small diamagnetic susceptibility contributions to be considered. The first of these, which is associated with the orbital motion of the tightly bound electrons on the vanadium ions, has a value (Van Vleck 1932) of $7{\cdot}7 \times 10^{-6}$ e.m.u./g atom, i.e. 2·5% of the susceptibility at room temperature. The second term arises from the curvature imposed by the magnetic field on the paths of the conduction electrons. This term cannot be calculated exactly but is probably negligibly small as the following rough argument shows.

The value for γ appropriate to a free electron gas containing five electrons per atom is $0{\cdot}94 \times 10^{-3}$ J/g atom deg^2 (Mott and Jones 1936). Vanadium metal, as mentioned however, has a γ of $8{\cdot}8 \times 10^{-3}$ J/g atom deg^2 so that the effective thermal mass, m_t, of the electrons at the Fermi surface is about nine times the normal electronic mass, m. We shall take m_t equal to m_a, the effective mass of the electrons accelerated by the magnetic field (Cohen 1958). Then, since the conduction electron diamagnetism (Landau 1930) is associated with the electronic orbits in momentum space it is inversely proportional to m_a^2 and not m^2. Thus, instead of being one-third of the paramagnetic susceptibility, as is the case for free electrons, this diamagnetic component for vanadium is only 0·4% of the paramagnetism.

6.2. *Chromium Metal*

Chromium is much more complex than vanadium in its magnetic behaviour. Shull and Wilkinson (1953) and later Corliss *et al.* (1959) found the metal to be antiferromagnetic with a mean moment per atom of $0{\cdot}4 \pm 0{\cdot}05\beta$. The magnetic susceptibility of an oxygen and nitgrogen-free polycrystalline specimen was measured over the temperature range 66° to 805°K by Lingelbach (1958). His graph shows a marked kink at a temperature (310°K) significantly close to the Néel temperature (T_N) of 308°K observed by Corliss *et al.* for a single crystal.

However, these results disagree with the value of T_N observed by Shull and Wilkinson, namely 475°K, on a polycrystalline specimen. This suggests that T_N may well depend on either the preparation or the impurity content of the sample. However it is difficult to reconcile this result with the fact that several of the properties of chromium show an anomaly only at about 310°K (Sully 1954). In particular, the heat capacity of a polycrystalline sample shows a lambda-type anomaly at 311·5°K (Beaumont *et al.* 1960). We shall therefore assume in our subsequent discussion of chromium that T_N is 310°K.

In contrast with the usual behaviour of antiferromagnetic materials the susceptibility above T_N does not decrease according to a Curie–Weiss law. Instead a progressive increase occurs, the value changing from 166×10^{-6} e.m.u./g atom at 310°K to 177×10^{-6} e.m.u./g atom at 800°K.

The electronic specific heat measurements made by Estermann *et al.* (1952) show that γ for pure chromium is $1{\cdot}54 \times 10^{-3}$ J/g atom deg^2. The density of states at the Fermi level calculated from this value is 0·33 states/ev atom—considerably less than that for vanadium. Wei *et al.* (1959) have found that γ increases rapidly as manganese and iron are dissolved in chromium. It seems likely therefore that the Fermi level for this metal falls just above a minimum in the density of states curve. This suggestion is well-supported by the measurements of soft X-ray absorption in thin films of chromium by Agarwal and Givens (1957).

The Pauli susceptibility of chromium at 0°K calculated from the above density of states value is 21×10^{-6} e.m.u./g atom. If we assume that the mean moment of each chromium atom above the Néel point is $0{\cdot}4\beta$ and the Curie–Weiss θ, like T_N, is 310°K, then the corresponding Curie–Weiss susceptibility at the Néel point is 194×10^{-6} e.m.u./g atom.

The sum of the Curie-Weiss and Pauli terms at 310°K (215×10^{-6} e.m.u./g atom) does not agree with the measured susceptibility value (173×10^{-6} e.m.u./g atom), corrected for the ion core diamagnetism ($6{\cdot}6 \times 10^{-6}$ e.m.u./g atom—Van Vleck 1932). This is not particularly significant since a slight increase in the value of θ could produce agreement. However, no change in θ or the mean moment per atom can account for an increase in the susceptibility of chromium above the Néel temperature. Thus according to the above figures the susceptibility should *decrease* by 87×10^{-6} e.m.u./g atom between 310° and 800°K instead of increasing by 11×10^{-6} e.m.u./g atom as observed.

It thus seems possible that, above the Néel temperature, there are no spins in chromium obeying a simple Curie Weiss law and that a collective electron model, such as the one developed by Lidiard (1954), is more appropriate.

Assuming this to be the case, and extrapolating to 0°K the susceptibility values observed for temperatures above T_N, then the corrected value of the susceptibility (χ_0) in the absence of antiferromagnetism is 170×10^{-6} e.m.u./g atom. Taking χ_p as 21×10^{-6} e.m.u./g atom the value obtained for K is 42000 g atom/e.m.u. The exchange interaction parameter is thus about eight times as large for chromium as for vanadium.

The calculated K values for 12 other transition metals for which the appropriate experimental data are available are less than 20000 g atom/e.m.u., except for tungsten (24000) and molybdenum (37000). The fact that the interaction parameter is large for these other two group VI metals, lends support to the idea that it should also be large for chromium.

As we have implied the two diamagnetic contributions to the susceptibility of chromium are, as for vanadium, both small. Thus the effective thermal mass of the electrons at the Fermi surface in chromium, calculated in a similar way to that described for vanadium, is about 1·6 times the electronic mass. The Landau diamagnetic component is therefore about 13% of the Pauli paramagnetism and less than 2% of the observed paramagnetism at room temperature. The core diamagnetism is about 4% of this observed figure.

6.3. *Vanadium–Chromium Solid Solutions*

The fall in susceptibility with composition for the alloys up to 80 at. % chromium is most simply explained in terms of a collective electron model. Thus the fact that the susceptibilities of all the alloys, like that of vanadium, are only weakly temperature dependent is evidence that no free permanent moments appear on either the vanadium or the chromium atoms. This is supported by some resistivity measurements (De Vries 1959) which show that the Néel temperature of chromium is very dependent on small alloying additions. De Vries found, for example, that the addition of 1 at. % of vanadium decreases T_N by 85°K, which suggests that there should be no moments present on the chromium atoms in an 80 at. % chromium alloy.

If the structure of the vanadium conduction band is assumed to remain essentially unchanged on adding chromium, then the major effect of alloying will be to produce an increase in the Fermi energy as electrons from the chromium atoms enter the common band. The Fermi level for vanadium comes at a point where the density of states is high but decreasing (Kriessman and Callen 1954) while, as mentioned, that of chromium probably occurs just above a minimum in the band. Thus, on alloying, the Pauli paramagnetism should initially decrease and then, finally, increase slightly.

On the basis of this model the observed susceptibility curve would represent the density of states curve as modified by the exchange interaction effect. The exchange parameter also will vary with composition. A possible relationship involving K is suggested by its behaviour, mentioned previously, for a number of transition metals. K for these metals is roughly inversely proportional to χ_p. If this were also true for these alloys then the observed susceptibility–concentration curve would be a direct representation of the density of states curve. All the observed oscillations would then be reflections of fine structure in this curve.

Such oscillations would not produce a temperature variation in susceptibility greater than that observed between 20 and 300°K. In this temperature range the edge of the Fermi distribution is sufficiently smeared out so that only an average of the sharp oscillation at 2 at. %, for instance, will be observed. However, by assuming that K is temperature independent a simple calculation shows that below 20°K the susceptibility of the 2 at. % alloy may further decrease by about 3%.

A small correction to the above model is necessary to allow for the increase in width of the band which must occur as a result of the decrease in interatomic spacing on alloying (§ 3.2). For example, if the lattice parameter of vanadium were reduced from 3·03 Å to 2·88 Å (the value for chromium) then the Pauli susceptibility, assuming a parabolic density of states curve, would decrease by 10%. The effect accounts for about one tenth of the observed susceptibility decrease between vanadium and chromium.

A confirmation of some of these ideas must await measurements of the electronic specific heat of all these alloys. It is gratifying that the results obtained at a few concentrations for the vanadium–chromium system by Wei, Cheng and Beck (private communication) qualitatively support our conclusions.

ACKNOWLEDGMENTS

We wish to thank Mr. A. D. Le Claire, Dr. W. M. Lomer, Dr. W. Marshall and Dr. P. C. L. Pfeil for helpful discussions. We are also indebted to Mr. C. E. Austing for chemical analysis and members of the Alloys Section of the Metallurgy Division, Harwell for assistance in the preparation and examination of the specimens. Dr. D. H. Baker of the U.S. Bureau of Mines and Dr. A. Wexler of the Westinghouse Research Laboratories kindly supplied us with some of the vanadium used. Mr. A. Calverley kindly supplied us with the zone-refined vanadium specimen. Finally we should like to thank Professor P. A. Beck for communicating his results prior to publication.

REFERENCES

AGARWAL, B. K., and GIVENS, M. P., 1957, *Phys. Rev.*, **107,** 62.

BEAUMONT, R. H., CHIHARA, H., and MORRISON, J. A., 1960, *Phil. Mag.*, **5,** 188.

CARLSON, O. N., and EUSTICE, A. L., 1959, U.S.A.E.C. Report IS-47.

CHILDS, B. G., GARDNER, W. E., and PENFOLD, J., 1959, *Phil. Mag.*, **4,** 1126.

CHILDS, B. G., and PENFOLD, J., 1957, *Phil. Mag.*, **2,** 389.

COHEN, M. H., 1958, *Phil. Mag.*, **31,** 762.

CORAK, W. S., GOODMAN, B. B., SATTERTHWAITE, C. B., and WEXLER, A., 1954, *Phys. Rev.*, **96,** 1442.

CORLISS, L. M., HASTINGS, J. M., and WEISS, R. J., 1959, *Phys. Rev. Letters*, **3,** 211.

DE VRIES, G., 1959, *J. Phys. Radium*, **20,** 438.

ESTERMANN, I., FRIEDBERG, S. A., and GOLDMAN, J. E., 1952, *Phys. Rev.*, **87,** 582.

KRIESSMAN, C. J., and CALLEN, H. B., 1954, *Phys. Rev.*, **94,** 837.

LANDAU, L., 1930, *Z. Phys.*, **64,** 629.

LIDIARD, A. B., 1954, *Proc. roy. Soc.* A, **224,** 161.

LINGELBACH, R., 1958, *Z. phys. Chem.* (Neue Folge), **14,** 1.

MOTT, N. F., 1935, *Proc. phys. Soc. Lond.*, **47,** 571.

MOTT, N. F., and JONES, H., 1936, *The Theory of the Properties of Metals and Alloys* (Oxford: University Press).

PAULI, W., 1927, *Z. Phys.*, **41,** 81.

ROSTOKER, W., 1958, *The Metallurgy of Vanadium* (London: Chapman and Hall).

SHULL, C. G., and WILKINSON, M. K., 1953, *Rev. mod. Phys.*, **25,** 100.

STONER, E. C., 1936, *Proc. roy. Soc.* A, **154,** 656.

SULLY, A. H., 1954, *Chromium* (London : Butterworths Scientific Publications), Chap. 3.

VAN VLECK, J. H., 1932, *Electric and Magnetic Susceptibilities* (Oxford: University Press).

WEI, C. T., CHENG, C. H., and BECK, P. A., 1959, *Phys. Rev. Letters*, **2,** 95.

The Hyperfine Structure of ^{209}Bi†

By R. S. Title‡ and K. F. Smith
Cavendish Laboratory, Cambridge

[Received August 19, 1960]

Abstract

The hyperfine structure (H.F.S.) of the $J=3/2$ ground state of ^{209}Bi has been found by the atomic beam magnetic resonance method. Two of the three H.F.S. intervals were measured directly, giving

$$(W_{50}-W_{60})/h=2884\cdot 7\pm 0\cdot 2\ \mathrm{Mc/s}$$

and $(W_{40}-W_{50})/h=2171\cdot 5\pm 0\cdot 1$ Mc/s. These results are consistent with a magnetic dipole interaction constant A of $-446\cdot 97\pm 0\cdot 04$ Mc/s and an electric quadruple interaction constant B of $-303\cdot 3\pm 0\cdot 3$ Mc/s. The latter yields an uncorrected nuclear electric quadrupole moment of $-0\cdot 34$ barns, and the field dependence of $\Delta F=0$ transitions gives $-1\cdot 6433\pm 0\cdot 0002$ for the ground state g_J value. The results are discussed in terms of the intermediate coupling theory of Breit and Wills (1933).

§ 1. Introduction

Goudsmith and Back (1927) studied the H.F.S. of the ^{209}Bi ground state by optical means and showed that the ground state has a total width of about $0\cdot 08\ \mathrm{cm}^{-1}$, or 2400 Mc/s, but they were unable to resolve the structure. Later Mrozowski (1942) resolved the largest of the three H.F.S. intervals and estimated a total width of about 6750 Mc/s; he also showed that the H.F.S. is inverted, i.e. the energy level with the smallest value of F has the largest energy and A is negative (see fig. 1). We have measured two of these intervals directly and the results are consistent with a total width of $6641\cdot 2\pm 0\cdot 7$ Mc/s. Rochester (1960) has confirmed that the sign of A is negative by the method described in the following paper on ^{121}Sb.

The principles of the method, which was first applied to atoms by Kellog *et al.* (1939), are given in detail in the book by Ramsey (1956). The atomic beam passes in turn through an inhomogeneous deflecting field H_a, a homogeneous field H_c and a second inhomogeneous deflecting field H_b before falling on the detector (fig. 2). A weak oscillating magnetic field H_ν superimposed on the steady field H_c induces transitions between certain states W_1 and W_2 with greatest probability when $h\nu=|W_1-W_2|$. The deflecting fields are arranged so that only atoms which undergo suitable transitions in the C field, the 'flopped' atoms, are refocused on the detector, the others being deflected away from the axis. An increase in detected beam then indicates the resonance condition and thus allows measurement of the energy interval.

---

† Communicated by the Authors.

‡ Now at I.B.M. Poughkeepsie, New York, U.S.A.

§ 2. Energy Levels

The energy levels expected for ^{209}Bi ($J=3/2$, $I=9/2$) in a steady magnetic field H_c are shown schematically in fig. 1, which applies when the H.F.S. is inverted. The general way in which the energy of any level $W(F, m_F)$ varies with H_c and depends on the constants I, J, F, m_F, g_J, A and B can be calculated by methods described by Ramsey (1956). Perturbation theory, for example, yields the following expressions for frequencies associated with the $\Delta F=0$ transitions marked by arrows in fig. 1:

$$\nu_\alpha=\frac{1}{4}x+\frac{3}{4}y-\frac{27}{176\nu_1}x^2+\frac{15}{352\nu_1}x^3, \qquad (1)$$

$$\nu_\beta=\frac{3}{20}x+\frac{51}{60}y+\left[\frac{21}{176\nu_1}-\frac{224}{822\nu_2}\right]x^2 -\left[\frac{3}{1760\nu_1}-\frac{112}{1375\nu_2}\right]x^3 \qquad (2)$$

Fig. 1

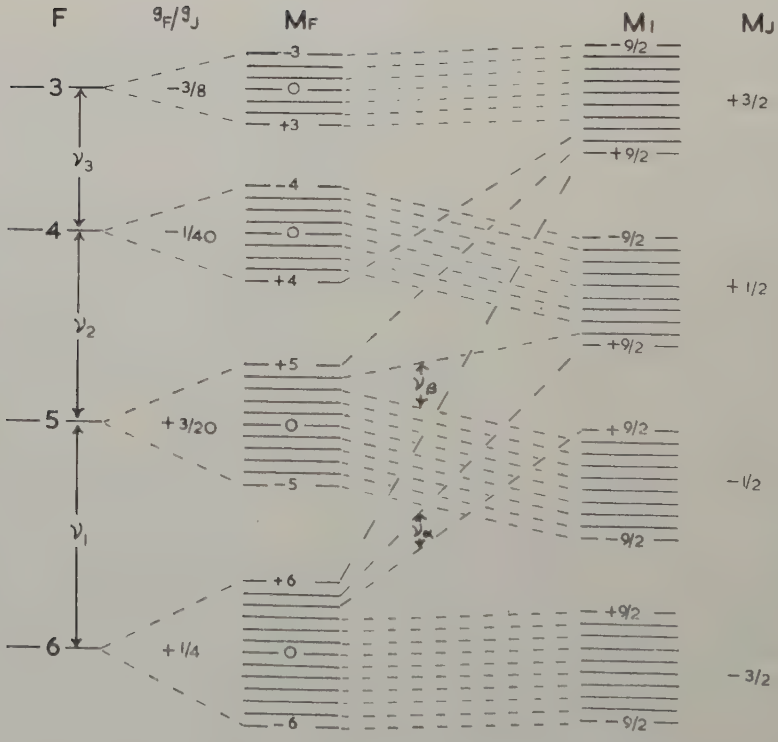

The hyperfine structure of ^{209}Bi in weak and strong fields (schematic).

where $x = g_J \mu_0 H_c / h$ and $y = g_I \mu_0 H_c / h$. The interaction constants A and B are related to the zero field intervals by

$$\left.\begin{aligned} \nu_1 &= 6A + 2B/3, \\ \nu_2 &= 5A - 5B/23, \\ \nu_3 &= 4A - 2B/3, \end{aligned}\right\} \text{Mc/s.} \qquad (3)$$

Fig. 2

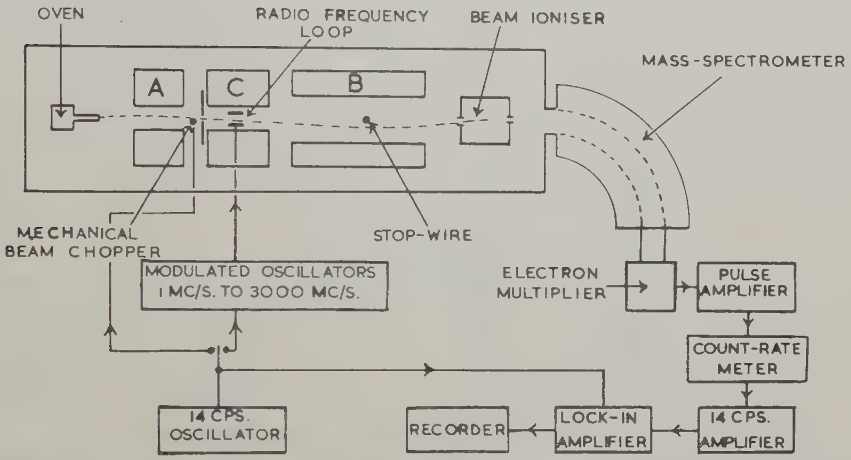

Schematic arrangement of the atomic beam magnetic resonance apparatus.

§ 3. Apparatus

The apparatus used by Bellamy and Smith (1953) for radioactive alkalis was modified so that an atomic bismuth beam could be produced and detected. The 'flop-in' magnet system was arranged to refocus on the detector only those atoms in which the oscillating field caused transitions such that the sign of m_J was changed and the selection rules for magnetic dipole transitions $\Delta F = 0$, $\Delta m_F = \pm 1$ or $\Delta F = \pm 1$, $\Delta m_F = 0$ or ± 1 were satisfied. The transitions marked in fig. 1 are suitable and these were studied in some detail.

The atomic bismuth beam was produced in the oven shown in fig. 3, which is similar to that used by Leu and Fraser (1928). Electron bombardment of the molybdenum snout by a current of 100 mA at 1400 v produced a snout temperature of 200°K, sufficient to cause almost complete dissociation of the molecules coming from the oven cavity, which remained at a temperature nearer 1000°K. A 0·004 in. wide oven slit was machined in the end of the snout.

The beam was detected with an electron bombardment detector (Wessel and Lew 1953). Positive ions produced by an electron current of 4 mA were analysed and counted by the mass-spectrometer and electron-multiplier used earlier by Bellamy and Smith (1953). The count-rate increase on resonance was only about 3% because of a large ionizer background so it was advantageous to amplitude modulate the beam or the radio-frequency field and use a phase-sensitive detector. Total beam intensities normally used were estimated to be about 10^{10} atoms per second at the detector.

The homogeneous field H_c was calibrated as required by observing resonances with a potassium beam from a separate resistance heated oven mounted beside the bismuth oven, and this beam was detected by surface ionization. Data published by Kusch and Taub (1949) were used to calculate the magnitude of H_c for a given ^{39}K resonance frequency.

Fig. 3

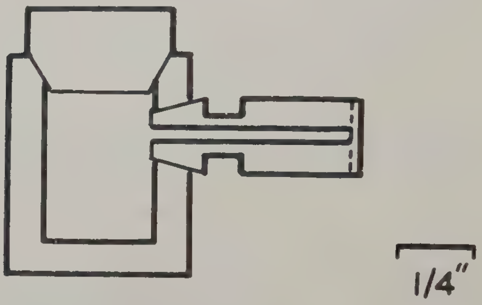

The bismuth oven.

The oscillating field was produced by a simple slotted hairpin in the C magnet gap. It could be positioned to stimulate σ transitions ($\Delta m_F = 0$, H_ν parallel to H_c) or π transitions ($\Delta m_F = \pm 1$, H_ν perpendicular to H_c) as required. Typical resonances were about 0·15 Mc/s wide and they were not broadened significantly by C field inhomogeneity. The σ resonances were double peaked, as one expects with this type of loop (Woodgate and Hellwarth 1956). Normal heterodyne methods were used to set the oscillator frequencies to about 2 parts in 10^6.

§ 4. RESULTS

The $\Delta F = 0$ transitions ν_α and ν_β indicated in fig. 1 were observed at each of the magnetic fields shown in the table. Insertion of these frequencies and fields into eqns. (1) and (2) then gave the values of ν_1 and ν_2 shown in the table, where it is seen that their accuracy increased rapidly with the magnitude of H_c. The nuclear magnetic resonance value of $+4{\cdot}0797$ NM obtained by Protor and Yu (1950) was used for μ_I.

Having determined the H.F.S. intervals to about ±20 Mc/s it was then possible to look for $\Delta F = \pm 1$ transitions and so determine the intervals with greater accuracy. Microwave triode oscillators were used to provide r.f. power in the frequency range required. Fifteen π transitions and nine σ transitions satisfy both the selection rules and the refocusing conditions in the apparatus, and all of these were observed in a field of 3·5 gauss.

Only the four transitions shown in fig. 1 were studied in detail, however, and the H.F.S. intervals and interaction constants which resulted after allowing for the field dependence were

$$\nu_1 = 2884{\cdot}7 \pm 0{\cdot}2\,\mathrm{Mc/s},$$
$$\nu_2 = 2171{\cdot}5 \pm 0{\cdot}1\,\mathrm{Mc/s}.$$

The interaction constants A and B with these intervals are

$$A = -446{\cdot}97 \pm 0{\cdot}04\,\mathrm{Mc/s},$$
$$B = -304{\cdot}25 \pm 0{\cdot}83\,\mathrm{Mc/s}.$$

Substitution of these intervals and the $\Delta F = 0$ frequencies ν_α and ν_β into eqns. (1) and (2) gives $1{\cdot}6433 \pm 0{\cdot}0002$ as an accurate value for g_J. The same result was obtained from both eqns. (1) and (2), thus showing that third-order perturbation theory yields a sufficiently accurate expression for the energy levels in this case. No direct measurement of ν_3 was carried out.

The observed frequencies ν_α and ν_β for the $\Delta F = 0$ transitions in different fields H_c, and the energy intervals ν_1 and ν_2 calculated using eqns. (1) and (2)

(^{39}K) (Mc/s)	H_c (gauss)	Observed frequencies		Calculated intervals	
		α (Mc/s)	β (Mc/s)	1 (Mc/s)	2 (Mc/s)
20·00	25·385	14·77 (5)	—	2909 (1100)	—
30·00	36·192	21·18 (5)	13·05 (3)	2800 (425)	2446 (170)
40·00	46·069	—	16·83 (2)	—	2198 (48)
60·00	63·665	37·76 (2)	23·78 (1)	2864 (51)	2191 (16)
120·00	105·768	64·00 (2)	41·64 (1)	2914 (20)	2184 (9)

§ 5. HYPERFINE STRUCTURE IN INTERMEDIATE COUPLING

Atomic bismuth has three electrons missing from the nearest closed shell and the five states of lowest energy belong to the p^3 configuration, for which the terms allowed by the Pauli principle are $^2P_{3/2}$, $^2P_{1/2}$, $^2D_{5/2}$, $^2D_{3/2}$ and $^4S_{3/2}$ in pure LS coupling. The coupling is intermediate between LS and jj for $J = 3/2$ states as indicated in fig. 4, so we represent the wavefunctions of these three states as linear combinations of the form

$$\psi(J=3/2) = c_1u_1 + c_2u_2 + c_3u_3 = d_1v_1 + d_2v_2 + d_3v_3 \quad . \quad . \quad . \quad (4)$$

where the v_k are the wavefunctions associated with the states $k = 1$, 2 and 3 in pure LS coupling and the u_k are the corresponding wave functions for pure jj coupling. The magnitudes of the c_k and the d_k depend on relative strengths for the Coulomb-repulsion and spin–orbit terms in the Hamiltonian, and there is a different set for each of the $J = 3/2$ states.

The wavefunctions for the $J=1/2$ and $J=5/3$ states are independent of coupling. The state of coupling is described by a parameter β, which can be determined by comparing the observed fine-structure with the theory, and the coefficients in eqn. (4) depend only on the energy W_k for each state k, and β. Formulae for the calculation of the c's are given by Breit and Wills (1933), Inglis and Johnson (1931) deal with the d's, and the general theory of intermediate coupling is discussed by Condon and Shortley (1931).

For the ground state of bismuth, one finds that $X=3111{\cdot}7\ \mathrm{cm}^{-1}$, $\beta=3{\cdot}10$, $c_1=-0{\cdot}188$, $c_2=+0{\cdot}345$, $c_3=+0{\cdot}918$, $d_1=-0{\cdot}354$, $d_2=-0{\cdot}515$ and $d_3=+0{\cdot}779$. The extent to which which the parameters β and X

Fig. 4

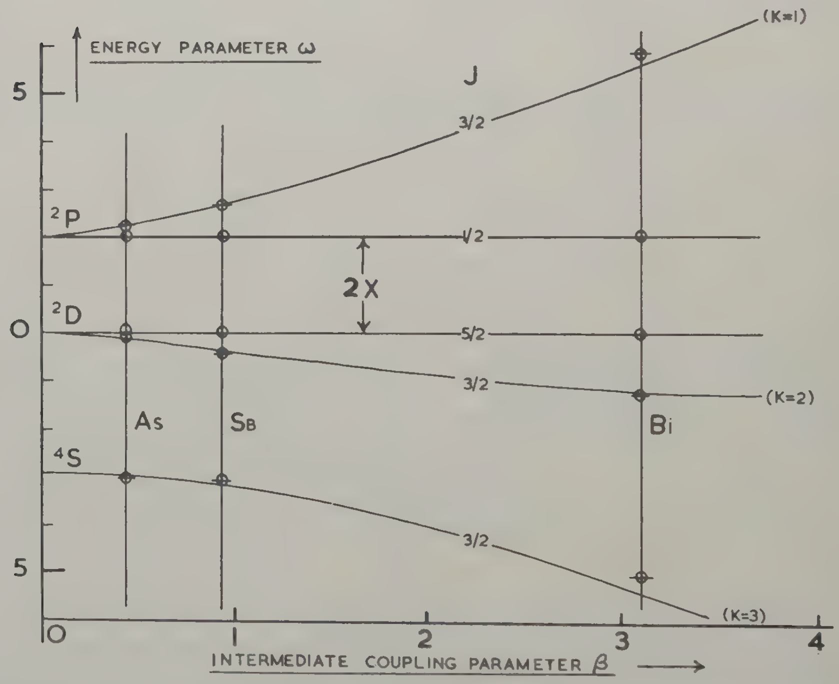

Atomic fine structure due to three p electrons in a state of intermediate coupling. The parameter β, defined by

$$\beta^2=\frac{4w_k(w_k+3)(w_k-2)}{9(w_k+3/5)},$$

is a measure of the coupling, the value being 0 for pure LS coupling and ∞ for pure jj coupling. The ordinate $w=2\,\frac{w_k-w_5}{w_4-w_5}$, a convenient function of energy, is plotted for the range $\beta=0$ to 4. The points represent optical results plotted at the value of the abscissa which affords the best fit to the theory. The states $J=1/2$ and $5/2$ have g_J, A and B values which are independent of β, although they may be perturbed by configuration interactions.

describe the energy levels is shown in fig. 4; the deviations may be due to the admixture of other configurations.

5.1. *Calculation of* g_J

The operator $g_J=(g_L L_Z+g_S S_Z)$ is diagonal in an LS$JM$ representation and the values of $\langle \mathrm{LS}J|g_J|\mathrm{LS}J\rangle$ are well known, so it is convenient to use the LS wavefunctions u_k for the calculation of g_J. First order theory gives

$$\left.\begin{aligned} g_J&=d_1^2\langle u_1|g_J|u_1\rangle+d_2^2\langle u_2|g_J|u_2\rangle+d_3^2\langle u_3|g_J|u_3\rangle,\\ g_J(J=3/2)&=d_1^2 g_J(^2\mathrm{P}_{3/2})+d_2^2 g_J(^2\mathrm{D}_{3/2})+d_3^2 g_J(^4\mathrm{S}_{3/2}).\end{aligned}\right\} \quad . \quad . \quad (5)$$

Substituting $g_J(^2\mathrm{D}_{3/2})=-0{\cdot}799$, $g_J(^2\mathrm{P}_{3/2})=-1{\cdot}334$, $g_J(^4\mathrm{S}_{3/2})=2{\cdot}002$ and the d values already listed into (5) gives $g_J=1{\cdot}651$ for the bismuth ground state, in reasonable agreement with the experimental result $-1{\cdot}6533(2)$.

5.2. *Calculation of A*

In order to calculate the expectation value of any operator $V=\sum V(\mathbf{r}_j)$, $\mathbf{r}_j$ being the position vector of the jth electron, one can use the jj wavefunctions v_k reduced to the form of sums and products of the single-electron wavefunctions (l, j, m), since the matrix elements $\langle l,j,m|V|l',j',m'\rangle$ can be calculated using the Dirac equation. Combining results for the p^3 configuration with (4) gives the magnitude of $\langle V\rangle$ for the state $J=3/2$, $M=3/2$ in terms of the single-electron matrix elements.

$$\begin{aligned}\langle V\rangle_{\frac{3}{2}\frac{3}{2}}=\langle \tfrac{3}{2}\tfrac{3}{2}|V|\tfrac{3}{2}\tfrac{3}{2}\rangle&+(c_1^2+\tfrac{4}{5}c_2^2)\langle \tfrac{3}{2}\tfrac{1}{2}|V|\tfrac{3}{2}\tfrac{1}{2}\rangle+(c_1^2+\tfrac{1}{5}c_2^2)\langle \tfrac{3}{2}-\tfrac{1}{2}|V|\tfrac{3}{2}-\tfrac{1}{2}\rangle\\ &+(\tfrac{1}{5}c_2^2+c_3^2)\langle \tfrac{1}{2}\tfrac{1}{2}|V|\tfrac{1}{2}\tfrac{1}{2}\rangle+(2/\sqrt{5})c_2(c_3-2c_1)\\ &\times(\tfrac{3}{2}-\tfrac{1}{2}|V|\tfrac{1}{2}-\tfrac{1}{2}\rangle+(2/\sqrt{5})\,c_2(2c_3-c_1)\langle \tfrac{3}{2}\tfrac{1}{2}|V|\tfrac{1}{2}\tfrac{1}{2}\rangle\\ &+(\tfrac{4}{5}c_2^2+c_3^2)\langle \tfrac{1}{2}-\tfrac{1}{2}|V|\tfrac{1}{2}-\tfrac{1}{2}\rangle. \quad . \quad . \quad . \quad . \quad . \quad . \quad (6)\end{aligned}$$

The single-electron matrix elements of $hA=\sum_j(\mu_I\,.\,\mathbf{H}_j)$, where $\mathbf{H}_j$ is the magnetic field at the nucleus due to the jth electron, have been calculated by Breit and Wills (1931), who show that

$$\left.\begin{aligned} ha'&=+2\mu_0^2 g_I\langle r^{-3}\rangle_{\mathrm{av}}\tfrac{8}{15}F_r'(lZ_i)=h\tfrac{3}{2}\langle \tfrac{3}{2}\tfrac{3}{2}|A|\tfrac{3}{2}\tfrac{3}{2}\rangle,\\ ha''&=+2\mu_0^2 g_I\langle r^{-3}\rangle_{\mathrm{av}}\tfrac{8}{3}F_r''(lZ_i)=h\tfrac{1}{2}\langle \tfrac{1}{2}\tfrac{1}{2}|A|\tfrac{1}{2}\tfrac{1}{2}\rangle,\\ ha'''&=-2\mu_0^2 g_I\langle r^{-3}\rangle_{\mathrm{av}}\tfrac{1}{6}G_r(lZ_i)\ =h\sqrt{2}\langle \tfrac{3}{2}\tfrac{1}{2}|A|\tfrac{1}{2}\tfrac{1}{2}\rangle,\\ A(J=\tfrac{3}{2})&=(c_1^2+\tfrac{6}{5}c_2^2+c_3^2)a'-\tfrac{1}{5}c_2^2a''-4\sqrt{\tfrac{2}{5}}c_2(c_1-c_3)a''',\\ A(J=\tfrac{5}{2})&=0{\cdot}8a'+0{\cdot}2a'',\\ A(J=\tfrac{1}{2})&=a'',\end{aligned}\right\} \quad . \quad (7)$$

where $F_r'(lZ_i)$, $F_r''(lZ_i)$ and $G_r(lZ_i)$ are relativistic factors of the order unity which are tabulated conveniently by Kopfermann (1958), page 445.

One way of estimating $\langle r^{-3}\rangle_{\mathrm{av}}$ is to make use of the expression

$$\tilde{a}=\beta X=2\mu_0^2 Z_i\langle r^{-3}\rangle_{\mathrm{av}}H(lZ_i) \quad . \quad . \quad . \quad . \quad (8)$$

where $\tilde{a}$ is the fine-structure interaction constant, which depends on the energy separation between two states independent of coupling, and the coupling parameter β (fig. 4). The effective atomic number Z_i is approximately equal to $Z-4$ for p electrons. Taking $X=3111\cdot7$ cm^{-1}, $\beta=3\cdot10$, the constants c already listed and the nuclear magnetic resonance value for g_I we get $+456$ Mc/s for $A(J=\frac{3}{2})$. This is opposite in sign to the experimental result $-446\cdot97\pm0\cdot04$ Mc/s. The eqns. (7) also predict a value wrong by a factor of five for the ratio a''/a', which can be deduced from the optical measurements of $A(J=\frac{5}{2})$ and $A(J=\frac{1}{2})$ made by Zeeman *et al.* (1930).

Breit and Wills (1933) suggested that such discrepancies might be due to interactions with other electronic configurations. Similar inconsistencies in the ratios of parameters have been found in the case of the 4s^{2}4p configuration of gallium (Koster 1952) and the 5p configuration of rubidium (Phillips 1956) and these have been explained in terms of s electron excitation. Koster (1952) showed that to a first-order approximation the fine structure is not affected by the admixture of excited s states, though it may have a significant effect on the H.F.S., so it may still be possible to use eqn. (6) to estimate $A(J=\frac{3}{2})$ if the a's are treated as parameters to be found by experiment. If a' and a'' are deduced from the optical H.F.S. measurement of $A(J=\frac{1}{2})$ and $A(J=\frac{5}{2})$, thus making first-order correcting for the configuration effects, and a''' is estimated from a'', the more accurately known parameter, $A(J=\frac{3}{2})$ comes to -413 ± 90 Mc/s, where the error reflects the uncertainty in the optical measurements. This result is in reasonable agreement with the experimental value. Further evidence for such configuration interactions in similar atoms is given in the following paper on the antimony isotopes.

5.3. *Nuclear Quadrupole Moment*

In order to calculate Q from the measured quadrupole interaction constant B it is necessary to estimate q_J, which is defined by

$$q_J=\langle-\sum r_j^{-3}(3\cos^2\theta-1)\rangle_{JJ}$$

and then use $hB=e^2q_JQ$. Schuler and Schmidt (1936) calculated the single-electron matrix elements of q_J and substituted them into (6) to get

$$q_J(J=\tfrac{3}{2})=-\tfrac{2}{5}\langle r^{-3}\rangle_{\text{av}}[R_r'(lZ_i)(c_1{}^2-c_3{}^2)+\sqrt{\tfrac{8}{5}}S_r(lZ_i)c_2(c_1+c_3)]. \qquad (9)$$

The relativity correction factors $R(lZ_i)$ and $S(lZ_i)$ are listed in Kopfermann (1958, p. 448) and the c's have already been given. Koster (1952) showed that the admixture of some excited s state does not affect the fine structure, and likewise, it should not contribute to the quadrupole interaction, so eqn. (9) may give a reasonable value for q when $\langle r^{-3}\rangle_{\text{av}}$ is estimated from fine-structure data and eqn. (8). When this is done one finds $Q=-0\cdot34b$. After making a Sternheimer (1952) correction, the result is increased slightly to $-0\cdot35b$. The error in Q due to the uncertainty in B is $\pm0\cdot001b$, but a much larger error is expected in Q because of the effects of other configuration interactions on the estimation of q_J and the uncertainty in the Sternheimer correction.

Acknowledgments

The authors wish to thank Mr. P. C. B. Fernando for the construction of the high-frequency oscillator in these experiments and Mr. G. K. Rochester for the measurement of the sign of A.

Dr. R. S. Title wishes to acknowledge the scholarships awarded by the Royal Commission for the Exhibition of 1851 and by the National Research Council of Canada.

References

Bellamy, E. H., and Smith, K., 1953, *Phil. Mag.*, **44,** 33.
Breit, G., and Wills, L., 1933, *Phys. Rev.*, **44,** 470.
Condon, E. U., and Shortley, G. H., 1951, *The Theory of Atomic Spectra* (Cambridge: University Press), p. 276.
Goudsmit, S., and Back, E., 1927, *Z. Phys.*, **43,** 321.
Inglis, D. R., and Johnson, M. H., 1931, *Phys. Rev.*, **38,** 1642.
Kellog, J. M. B., Rabi, I. I., Ramsey, N. F., and Zacharias, J. R., 1939, *Phys. Rev.*, **56,** 728.
Kopfermann, H., 1958, *Nuclear Moments.* English Edition (New York: Academic Press Inc.).
Koster, G. F., 1952, *Phys. Rev.*, **86,** 148.
Kusch, P., and Taub, H., 1949, *Phys. Rev.*, **75,** 1477.
Leu, A., and Fraser, R. G. J., 1928, *Z. Phys.*, **49,** 498.
Mrozowski, S., 1942, *Phys. Rev.*, **62,** 526.
Phillips, M., 1956, *Phys. Rev.*, **103,** 322.
Proctor, W. G., and Yu, F. C., 1950, *Phys. Rev.*, **78,** 471.
Ramsey, N. F., 1956, *Molecular Beams* (Oxford: University Press).
Schuler, H., and Schmidt, T., 1936, *Z. Phys.*, **99,** 717.
Sternheimer, R., 1952, *Phys. Rev.*, **86,** 316.
Wessel, G., and Lew, H., 1953, *Phys. Rev.*, **92,** 641.
Woodgate, G. K., and Hellwarth, R. W., 1956, *Proc. phys. Soc. Lond.* A, **69,** 588.
Zeeman, P., Back, E., and Goudsmit, S., 1930, *Z. Phys.*, **66,** 1.

The Hyperfine Structure of ^{121}Sb and ^{123}Sb†

By P. C. B. Fernando‡, G. K. Rochester, I. J. Spalding§
and K. F. Smith
Cavendish Laboratory, Cambridge

[Received August 19, 1960]

Abstract

The hyperfine structure of the $J=3/2$ ground state of ^{121}Sb and ^{123}Sb has been studied by the atomic beam magnetic resonance method, and the results are consistent with the following values for the interaction constants:

$$g_J=-1{\cdot}9705\pm0{\cdot}0002,\qquad A_{121}=-(299{\cdot}034\pm0{\cdot}004)\ \text{Mc/s},$$
$$A_{123}=-(162{\cdot}451\pm0{\cdot}003)\ \text{Mc/s},\quad B_{121}=-(3{\cdot}68\pm0{\cdot}02)\ \text{Mc/s},$$
and
$$B_{123}=-(4{\cdot}67\pm0{\cdot}03)\ \text{Mc/s}.$$

To the accuracy of the measurements there was no evidence for an octupole interaction.

From the B values one obtains $Q_{121}=-(0{\cdot}20\pm0{\cdot}03)\times10^{-24}\ \text{cm}^2$ and $Q_{123}=-(0{\cdot}26\pm0{\cdot}04)\times10^{-24}\ \text{cm}^2$, and comparison of A_{121}/A_{123} with the ratio of g_{121}/g_{123} already published gives $-0{\cdot}318\pm0{\cdot}003\%$ for the hyperfine structure anomaly. Intermediate coupling theory accounts satisfactorily for g_J, but an admixture of excited s states is necessary to explain the observed magnetic interaction and anomaly.

§ 1. Introduction

Lowenthal (1929) investigated the optical Zeeman effect of the Sb I fine structure and showed that Russell–Saunders coupling of the valence electrons was not complete. He assigned an experimental value to the ground state g_J. Crawford and Bateson (1934) studied the optical H.F.S. of Sb IV and assigned nuclear spin (I) and nuclear magnetic moment (μ_I) values to the stable ^{121}Sb and ^{123}Sb isotopes. Loomis and Strandberg (1951) used the microwave resonance method to obtain an accurate value for the ratio of the quadrupole moments of these two isotopes and so stimulated further experiments on the optical hyperfine structure of Sb II by Sprague and Tomboulian (1953). Murakawa (1955) using separated isotopes, and Gordy (1955), obtained results for the ratio of the quadrupole moments somewhat different from those of Sprague. No direct optical observation of the atomic ground state H.F.S. has yet been made.

Dehmelt and Krüger (1951), and Wang (1955), measured the ratio Q_{121}/Q_{123} to about 1 in 6000 using pure nuclear quadrupole resonance techniques, and the ratio μ_{121}/μ_{123} has been measured accurately in nuclear resonance experiments by Cohen *et al.* (1950), Collins (1950) and Proctor and Yu (1950). Eisinger and Feher (1958) have recently re-measured μ_{121}/μ_{123} and used the Electron Nuclear Double Resonance (ENDOR) technique to measure the ratio A_{121}/A_{123} for the simpler $s_{1/2}$-like electronic configuration of Sb in silicon.

---

† Communicated by the Authors.

‡ Now at Physics Department, University of Columbo, Columbo, Ceylon.

§ Now at A.E.R.E. Harwell, Didcot, Berks.

We have used an atomic beam magnetic resonance apparatus to investigate the H.F.S. of the ground states of ^{121}Sb and ^{123}Sb. The field-dependent $\Delta F=0$ transitions and all the $\Delta F=1$ transitions were observed with both isotopes and from the results we deduce values of g_J, Q_{121} and Q_{123}, and also the H.F.S. anomaly, which is defined by ${}_{121}\Delta_{123}=(a_{121}/a_{123})(g_{123}/g_{121})-1$.

§ 2. APPARATUS

The apparatus for this experiment was the same as that used in the study of ^{209}Bi by Title and Smith (1960) (see preceding paper, which will be referred to as I).

Antimony dissociates at a higher temperature than bismuth so the oven snout was lengthened and made of tungsten instead of molybdenum. With this modification a convenient beam intensity was obtained when the end of the snout was hot enough to bring about a high degree of dissociation. Residual molecules were intercepted with a stop wire, and the signal-to-noise ratio was further improved by modulating the beam at 14 c.p.s. instead of 25 c.p.s. The output from the phase-sensitive detector was fed into a pen recorder which traced the resonance as the oscillator was scanned through the resonant frequency.

§ 3. PROCEDURE

The energy level diagrams for ^{121}Sb ($J=3/2$, $I=5/2$) and ^{123}Sb ($J=3/2$, $I=7/2$) are shown in fig. 1. The levels are inverted because A is negative. The interaction constants are related to the zero field intervals as follows:

^{121}Sb	^{123}Sb
$\nu_1=4A+4B/5+32C/5$	$\nu_1=5A+5B/7+40C/7$
$\nu_2=3A-9B/20-84C/5$	$\nu_2=4A-2B/7-88C/7$
$\nu_3=2A-4B/5+96C/5$	$\nu_3=3A-5B/7+88C/7$

where C is a possible magnetic octupole interaction constant.

ν_α and ν_β are the only two $\Delta F=0$ transitions which satisfy the refocusing conditions of the machine. They were followed up to fields of 100 gauss, and the magnitudes of the constants g_J, A and B deduced therefrom were used to calculate the approximate frequencies of the $\Delta F=1$ transitions. These were then measured directly to give more accurate values for A and B.

Since $m_F=0$ levels are field independent to the first order, it is desirable to observe $\Delta F=1$ transitions involving these levels because small fluctuations in magnetic field during the experiment are less important, the field correction to the final result is smaller, and small field inhomogeneities in the C magnet do not deform the line shape. All the refocused $\Delta F=1$ transitions were scanned at C fields of about 1 gauss, and ν_2, the only field independent resonance which satisfied the refocusing conditions, was measured accurately. A double resonance technique introduced by Davis *et al.* (1949) was used to observe the field independent transitions ν_1 and ν_3. Two triode cavity oscillators were coupled to the same r.f. loop, the first was set on one of the two maxima associated with the ν_2 σ-transition (Woodgate and Hellwarth 1956), while the second was scanned through the frequencies expected for ν_1 and ν_3. The refocused beam intensity was reduced on resonance because of transitions to the upper or lower level and the double-humped ν_1 and ν_3 resonances traced by the recorder thus appeared inverted. Careful adjustment of both power levels was essential. The procedure was then repeated with the first oscillator set on the other maximum of the ν_2 resonance, but no shifts of frequency were found. From the three zero-field H.F.S. intervals measured in this way we deduced A and B and showed that C is zero within the accuracy of the measurements. The results are given in table 1.

Fig. 1

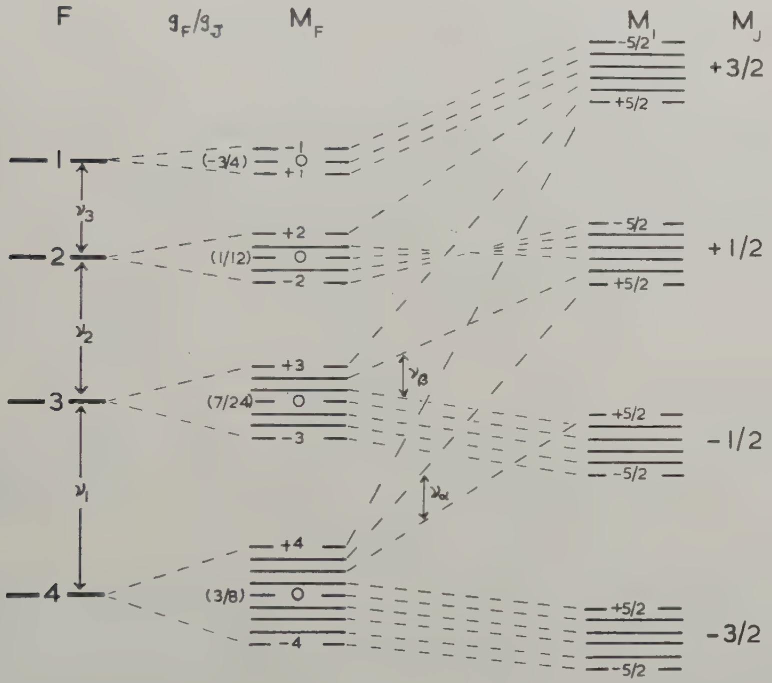

The sign of A_{121} was determined by a method used previously by King and Jaccarino (1954). Atoms with one sign of m_J, say $m_J=+\frac{1}{2}$, were removed by a stop wire in the A magnet and the low frequency $\Delta F=0$ transition ν_β was used to refocus the $m_J=-\frac{1}{2}$ atoms on to the detector. A second frequency ν_F (fig. 2) was then applied to a separate r.f. loop some two inches nearer the detector, and the refocused beam decreased in intensity, showing that A is negative; had A been positive there would have been no change in intensity. A similar effect was obtained when the frequencies ν_β and ν_F were used in the reverse order and the atoms with $m_J=-\frac{1}{2}$ were suppressed instead of those with $m_J=+\frac{1}{2}$.

Table 1. Zero field intervals and interaction constants for ^{121}Sb and ^{123}Sb

^{121}Sb (Mc/s)	^{123}Sb (Mc/s)
$\nu_3=595{\cdot}12\pm0{\cdot}01$ $\nu_2=819{\cdot}45\pm0{\cdot}01$ $\nu_1=1199{\cdot}08\pm0{\cdot}01$ $A=-299{\cdot}034\pm0{\cdot}004$ $B=-3{\cdot}68\pm0{\cdot}02$	$\nu_3=484{\cdot}02\pm0{\cdot}01$ $\nu_2=648{\cdot}46\pm0{\cdot}01$ $\nu_1=815{\cdot}60\pm0{\cdot}01$ $A=-162{\cdot}451\pm0{\cdot}003$ $B=-4{\cdot}67\pm0{\cdot}03$
$g_J=-1{\cdot}9705\pm0{\cdot}0002$	

Fig. 2

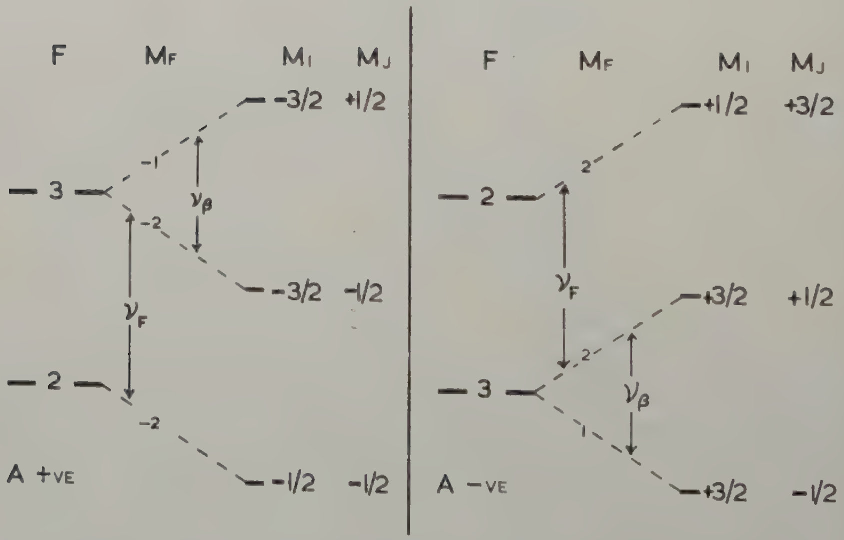

An accurate value of g_J can usually be obtained by substituting the H.F.S. intervals in the perturbation theory equations for the $\Delta F=0$ transitions. However, the g_J's deduced from ν_α and ν_β differed by more than the probable error when perturbation theory up to the third order was used, so the secular equation was solved numerically using a digital computer. The values of g_J deduced from each transition were then identical over a wide range of C fields.

§ 4. Discussion of Results

4.1. *Fine Structure and g_J*

Atomic antimony has two 5s electrons and three 5p electrons outside a closed sub-shell and the coupling of the p electrons is intermediate between LS and jj. The ground state wave function can be written in the form of eqn. (4) of I with

$$c_1=0{\cdot}361\pm0{\cdot}002,\qquad c_2=-0{\cdot}689\pm0{\cdot}004,\qquad c_3=-0{\cdot}628\pm0{\cdot}006,$$
$$d_1=-0{\cdot}188\pm0{\cdot}005,\quad d_2=+0{\cdot}057\pm0{\cdot}004,\qquad d_3=0{\cdot}980\pm0{\cdot}002,$$
$$a=3270{\cdot}5\ \text{cm}^{-1},\qquad \beta=0{\cdot}93\pm0{\cdot}02.$$

This value of β, which is slightly different from that obtained by Inglis and Johnson (1931) using the same theory, was estimated by making a simplified least squares fit of the theory to the fine structure measured optically by Lowenthal (1929). The error in β gives an indication of the closeness of the fit of the intermediate-coupling theory to the fine structure and the quoted errors in the c's and the d's are those which arise only from the uncertainty in β. It will be noted that the state is almost entirely LS coupled, being 98% $^4S_{3/2}$.

The theoretical estimate, neglecting relativistic effects, of

$$g_J=-1{\cdot}971\pm0{\cdot}004$$

is obtained by substituting the above values of d_i in eqn. (5) of I. This is in good agreement with the experimental $g_J=1{\cdot}9705\pm0{\cdot}0002$.

4.2. *Comparison of A with Theory*

The intermediate-coupling theory fits the five fine-structure levels with only two parameters β and $\tilde{a}$, and the experimental agreement is quite good, so one might expect this theory to account for the observed hyperfine structure in a satisfactory manner. However, the calculation of A_{121} using this theory (eqn. (7)) gives $A_{121}=-15\pm5$ Mc/s, where the error is due to the uncertainty in β. For this calculation we used the g_I measured by Eisinger and Feher (1958), and the values $\tilde{a}=3041{\cdot}6\ \text{cm}^{-1}$ and $\langle r^{-3}\rangle_{\text{av}}=70{\cdot}8\ \text{Å}^{-3}$, which were obtained by substituting $\beta=0{\cdot}93$ and $X=3270{\cdot}4\ \text{cm}^{-1}$ in (8). The experimental value of A_{121} is $-299{\cdot}032$ Mc/s. It is possible that the discrepancy is due to configuration interactions which do not alter either g_J or the form of the fine structure. In addition, the ratio a'/a'' deduced from (7) should be 0·17 for a pure p^3 configuration, whereas optical measurements of $A(P_{1/2})$ and $A(D_{5/2})$ by Badami (1932) yield 0·22. If we try to allow for the effect of any admixed configurations by treating the optical results $a' = 1068 \pm 350$ Mc/s and $a'' = 4740 + 140$ Mc/s as experimental parameters in the intermediate-coupling theory, a method which gave a reasonable fit in the case of Bi, we obtain

$$A(J=5/2) = +274 \pm 400 \text{ Mc/s}.$$

The error here is associated with the optical measurements and the corresponding error due to the uncertainty in β is only 7 Mc/s. No conclusion about the validity of this procedure can be drawn because of the large error in the predicted value of $A(J=3/2)$.

4.3. *Hyperfine Structure Anomaly*

The ratio g_{121}/g_{123} has been measured by Eisinger and Feher (1958) and this may be combined with our measurement of A_{121}/A_{123} to give $(-0{\cdot}317 \pm 0{\cdot}003)\%$ for the H.F.S. anomaly ${}_{121}\Delta_{123}$. Eisinger and Feher have also measured ${}_{121}\Delta_{123}$ for an atomic configuration which is essentially a pure s state and they obtained $(-0{\cdot}352 \pm 0{\cdot}005)\%$, which is only slightly larger than that measured for the intermediately-coupled p^3 configuration. They have considered several nuclear models and conclude that the model which gives the best result for μ_{121}, Q_{121} and $\Delta(s)$ is the configuration mixing model, for which $\Delta(s) = -0{\cdot}365\%$.

The Breit Rosenthal contribution to Δ is $\sim 10^{-2}\%$ for the atomic s state and is much smaller for p states. We have estimated the Bohr–Weisskopf anomaly for the configuration mixing model, using (6), and conclude that $\Delta(p^3)$ is probably smaller than $-0{\cdot}08\%$ if off-diagonal terms are neglected. The anomaly we have measured is typically that expected for an s state, and a small s state admixture could also account for the magnitude of A.

4.4. *Configuration Interactions*

The only configurations which can be mixed with the antimony ground state to produce a large hyperfine anomaly and almost no change of g_J are those in which s electrons are excited to higher s states. Koster (1952) and Phillips (1956) accounted for inconsistent values of a'/a'' in Ga and Rb, similar to those which we now find in Sb, by means of outer s electron excitation. Abragam (1955), Heine (1957), Sternheimer (1957), Cohen *et al.* (1959) and Blinder (1960) considered the exchange interactions between the aligned valence electrons and s electrons in different shells, and showed that different spin-up and spin-down electron densities at the nucleus are associated with each of the s shells. The contact term in the expression for A is then a sum of several terms, each with a sign and magnitude dependent on the overlap of the s and valency electron wave functions, and the resultant A is sensitive to the s wave functions used. No detailed calculation of this sort has been carried out for antimony.

The breakdown of LS coupling contributes only -15 Mc/s out of the total observed value of -299 Mc/s to A_{121}. If we assume then that most of the magnetic interaction is due to s electron excitation, any s state admixture which satisfactorily accounts for A gives automatically an

H.F.S. anomaly of the right sign and magnitude, irrespective of the detailed form of the calculations. In addition, excitation of s electrons to higher s states does not alter g_J, since the contribution from these electrons remains zero.

Table 2. Values for Q_{121}, Q_{123} and Q_{121}/Q_{123} reported in the literature

Method	Q_{121} $\times 10^{-24}$ cm^2	Q_{123} $\times 10^{-24}$ cm^2	Q_{121}/Q_{123}
Dehmelt and Krüger (1951) nuclear quadrupole resonance	—	—	0·7843 $\pm$0·0001
Loomis and Strandberg (1951), microwave spectrum of Sb H_2D	$-0·35$ to $-0·50$	$-0·45$ to $-0·62$	0·791
Sprague and Tomboulian (1953), optical H.F.S.	$-1·2$	$-1·6$	—
Murakawa (1955), optical H.F.S.	$-0·52 \pm 0·1$	$-0·67 \pm 0·1$	0·73 $\pm$0·06
Wang (1955), nuclear quadrupole resonance in crystals	—	—	0·7844 $\pm$0·0001
Gordy (1955), microwave absorption	$-0·8$	$-1·0$	0·784 $\pm$0·002
As reported in this paper	$-0·20 \pm 0·03$	$-0·26 \pm 0·04$	0·784 $\pm$0·008

4.5. *Quadrupole Moments*

Sternheimer (1957) has published a general discussion of the effects of core excitation with particular reference to the calculation of quadrupole moments. He has shown that the corrections can be quite large even when fine or hyperfine structure data are used to calculate $\langle r^{-3}\rangle_{\text{av}}$, and that they are sensitive to the wave functions used for the core and valence electrons. If the excitation of s electrons to higher s states is the predominant effect, however, both the quadrupole interaction and the fine structure remain almost unchanged and we can use eqn. (9) of I to estimate Q. Quadrupole moments calculated in this way are compared with results obtained by other methods in table 2. The errors assigned to our Q values are those associated with the uncertainty in β, and no Sternheimer corrections have been made. Although there is some considerable disagreement about the magnitudes of the quadrupole moments, the signs are all negative and our value for Q_{121}/Q_{123} agrees with the quadrupole resonance results.

ACKNOWLEDGMENTS

The authors wish to thank Dr. Heine and Professor Bleaney for useful discussions about electron configuration interactions. They would also like to thank Dr. Oxley for devising a programme for the calculation of g_J, and the Director of the Mathematical Laboratory for the use of the electronc computer Edsac II.

REFERENCES

ABRAGAM, A., HOROWITZ, J., and PRYCE, M. H. L., 1955, *Proc. roy. Soc.* A, **230,** 169.

BADAMI, J. S., 1932, *Z. Phys.*, **79,** 230.

BLINDER, S. M., 1960, *Bull. Amer. phys. Soc.*, **5,** 14.

COHEN, M. H., GOODINGS, D. A., and HEINE, V., 1959, *Proc. phys. Soc. Lond.*, **73,** 811.

COHEN, V. W., KNIGHT, W. D., WENTINK, T., and KOSKI, 1950, *Phys. Rev.*, **79,** 191.

COLLINS, T. L., 1950, *Phys. Rev.*, **79,** 226.

CRAWFORD, M. F., and BATESON, S., 1934, *Canad. J. Res.* A, **10,** 693.

DAVIS, L., FELD, B., ZABEL, C., and ZACHARIAS, J., 1949, *Phys. Rev.*, **76,** 1082.

DEHMELT, H. G., and KRÜGER, H., 1951, *Z. Phys.*, **130,** 385.

EISINGER, J., and FEHER, G., 1958, *Phys. Rev.*, **109,** 1172.

GORDY, W., 1955, *Phys. Rev.*, **97,** 680.

GOUDSMIT, S., 1933, *Phys. Rev.*, **43,** 636.

HEINE, V., 1957, *Phys. Rev.*, **107,** 1002.

KING, J. G., and JACCARINO, V., 1954, *Phys. Rev.*, **94,** 1610.

KOSTER, G. F., 1952, *Phys. Rev.*, **86,** 148.

LOOMIS, G. C., and STRANDBERG, M. W. P., 1951, *Phys. Rev.*, **81,** 798.

LOWENTHAL, H., 1929, *Z. Phys.*, **57,** 828.

MURAKAWA, K., 1955, *Phys. Rev.*, **100,** 1371.

PHILLIPS, M., 1956, *Phys. Rev.*, **103,** 322.

PROCTOR, W. G., and YU, F. C., 1950, *Phys. Rev.*, **81,** 20.

SCHWARTZ, C., 1955, *Phys. Rev.*, **99,** 1035.

SPRAGUE, G. and TOMBOULIAN, D. H., 1953, *Phys. Rev.*, **92,** 105.

STERNHEIMER, R. M., 1957, *Phys. Rev.*, **105,** 168.

TITLE, R. S., and SMITH, K. F., 1960, *Phil. Mag.*, **5,** 1281.

WANG, C., 1955, *Phys. Rev.*, **99,** 566.

WOODGATE, G. K., and HELLWARTH, R. W., 1956, *Proc. phys. Soc. Lond.* A, **69,** 588.

CORRESPONDENCE

On the Scattering of Phonons by Spins at Low Temperatures
Experimental

By H. M. Rosenberg and B. Sujak†
The Clarendon Laboratory, Oxford

[Received August 29, 1960]

This paper reports some preliminary experiments which show how the heat conductivity of a dielectric crystal may be profoundly influenced by the presence of a small number of paramagnetic ions. Measurements of the thermal conductivity between 2 and 20°K have been made on crystals of Analar grade zinc sulphate, $ZnSO_4.7H_2O$ (maximum impurity 0·006%) and also on zinc sulphate crystals which contained 0·25, 1 and 5·6 at. % of $FeSO_4.7H_2O$. These measurements were compared with those on crystals of zinc sulphate which contained 5·7 at. % of a non-paramagnetic impurity, $MgSO_4.7H_2O$. All the crystals were 2 to 3 cm long and had a square cross section with a side of 3 to 4 mm. The measurements were made in a manner similar to that described by Rosenberg (1955).

Some of the results are shown in the figure (*a*). The curves for the pure material are on the whole of the usual type which one expects for the thermal conductivity of a dielectric crystal (see Berman 1953, Klemens 1956, or Ziman 1960, for general reviews). The rapid rise in conductivity on the high temperature side of the maximum is due to the decrease in the effectiveness of the scattering of the phonons by impurities or isotopes, and the decrease in conductivity at temperatures below the maximum is caused by the scattering of the phonons by the boundaries of the specimen or of small crystallites. It is unfortunate that it is not easy to grow very perfect crystals from a saturated aqueous solution and there is considerable scatter (from 25 to 50%) in the data from different crystals of the same composition.

The main interest lies in the measurements taken above the conductivity maximum. The extra thermal resistance in the specimens containing Fe^{2+} is shown in the figure (*b*). It will be noted that the addition of 5·6% Fe^{2+} decreases the conductivity and completely changes the temperature dependence from $T^{-1\cdot5}$ to about $T^{-0\cdot5}$. This change cannot be ascribed merely to an impurity scattering effect, because as the figure (*a*) shows, the conductivity of a specimen containing 5·7% Mg is very much closer to that of the pure material. This can be emphasized still further when we note that the thermal resistance due to impurity scattering is proportional to the *square* of the mass difference between the impurity and the other atoms (see Ziman 1960). Since the mass difference between Mg and Zn is about 41, whereas between Fe and Zn it is only 9·5, the effect of the Mg impurity should be very much greater than the Fe impurity instead of being much less.

---

† On leave from Zaklad Niskich Temperatur Instytutu Fizyki Polskiej, Akademii Nauk, Wrocław, Poland.

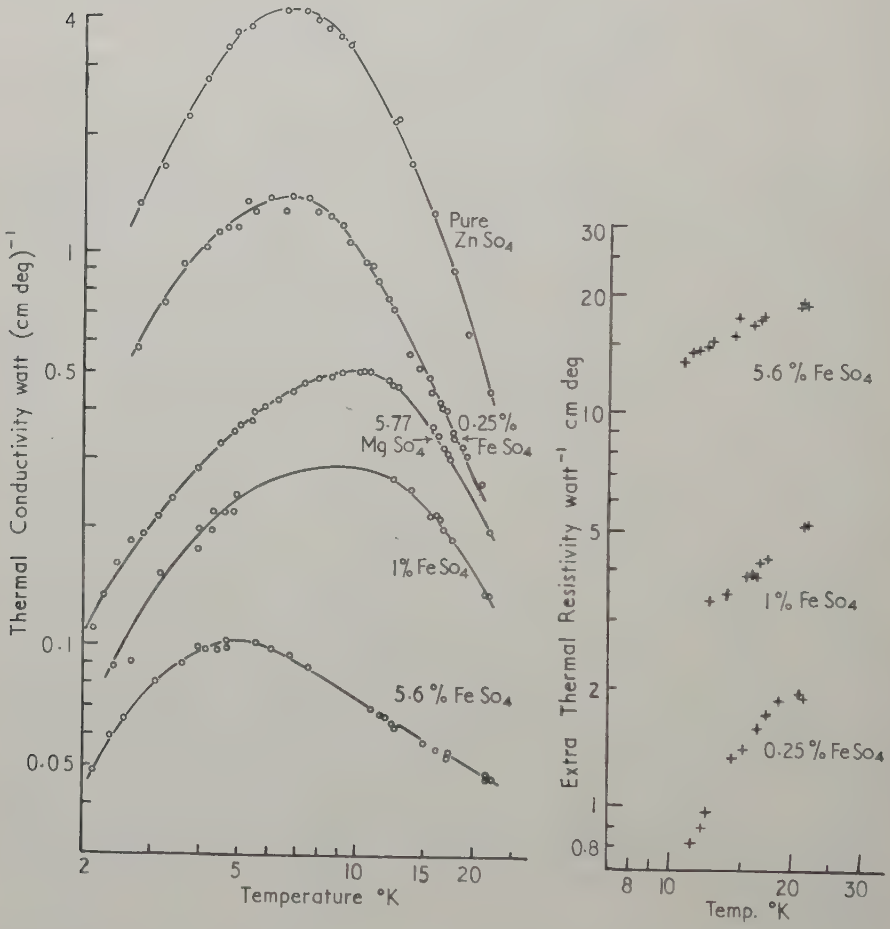

(*a*) (*b*)

(*a*) The thermal conductivity of pure hydrated zinc sulphate crystals and of zinc sulphate with 0·25, 1 and 5·6 at. % $FeSO_4 . 7H_2O$, and 5·7 at. % $MgSO_4 . 7H_2O$. (*b*) The extra thermal resistance in the zinc sulphate crystals which have additions of Fe^{2+}.

DISCUSSION

We suggest that the large decrease in conductivity which is observed for the specimens containing 5·6% Fe^{2+} is due to Raman type interactions between the phonons and the low-lying spin levels of the ferrous ion. By this we mean that a phonon interacts with a spin, flips it to another level and another phonon is emitted. Since, for the Fe^{2+} ion, the spin–lattice relaxation time is thought to be very short (see, for example, Tinkham 1956), the probability for this mechanism will be high. The theory of these processes has been given by Orbach (1960) and is presented in the following letter. He has also calculated the scattering due to direct processes, i.e. those in which a phonon of just the right energy is absorbed so that a spin may be flipped without the need for the emission of another phonon to maintain the energy balance, but he finds that the probability of such processes is much lower in the temperature region of our experiments than are the Raman processes.

Unfortunately a detailed calculation of the effect is not possible because the splitting of the lowest levels of the Fe^{2+} ion is not known. Some specific heat measurements have been made on the 5·6% Fe^{2+} crystal, however, and these have an anomaly with a peak at about 1·8°K, which can be ascribed to a splitting of $4{\cdot}3 \pm 0{\cdot}2$ degrees. If such a splitting is assumed, then Orbach's calculations yield an additional thermal resistivity of about the order of magnitude which we observe and with a temperature dependence which seems to vary with concentration as in fig. 1 (*b*) (see figure in following letter).

It is clear that more experiments must be made using other types of crystal (preferably without water of crystallization, because these are usually much more perfect). It is just possible that the difference in the curves which we observed are due to the fact that some specimens are not very perfect. It is known that some hexahydrate can co-exist with the heptahydrate and that there are in fact two crystallographic forms for the heptahydrate (Giauque *et al.* 1950). It does not seem likely, however, that the large change observed for the specimens containing 5·6% Fe^{2+} can be due entirely to defective crystals. Other types of spin–phonon interaction in heat conduction experiments have in fact been observed in ferrites (Friedberg and Douthett, 1958) and antiferromagnetics (Slack and Newman 1958) and these give further grounds for confidence in our results.

ACKNOWLEDGMENTS

We should like to thank Dr. R. Orbach for the very valuable discussions which led to the interpretation of the results and we are very grateful to Dr. P. D. F. Shaw for analysing the specimens and to Dr. C. A. Bailey for making the specific heat measurements.

REFERENCES

BERMAN, R., 1953, *Advanc. Phys.*, **2,** 103.
FRIEDBERG, S. A., and DOUTHETT, D., 1958, *Physica*, **24,** S 176.
GIAUQUE, W. F., BARIEAU, R. E., and KUNZLER, J. E., 1950, *J. Amer. chem. Soc.*, **72,** 5685.
KLEMENS, P. G., 1956, *Handb. der Phys.*, **14,** 198.
ORBACH, R., 1960, *Phil. Mag.*, **5,** 1303.
ROSENBERG, H. M., 1955, *Phil. Trans.* A, **247,** 441.
SLACK, G. L., and NEWMAN, R., 1958, *Phys. Rev. Letters*, **1,** 359.
TINKHAM, M., 1956, *Proc. roy. Soc.* A, **236,** 535.
ZIMAN, J. M., 1960, *Electrons and Phonons* (Oxford: Clarendon Press).

On the Scattering of Phonons by Spins at Low Temperatures Theoretical

By R. Orbach
University of California, Department of Physics, Berkeley, California
and
Clarendon Laboratory, Oxford

The previous paper (Rosenberg and Sujak 1960) has described the observed effects of paramagnetic impurities on the thermal conductivity of a dielectric salt: $FeSO_4 . 7H_2O$ in $ZnSO_4 . 7H_2O$. It is the purpose of this letter to briefly analyse their results in terms of a theoretical model.

In the usual treatment of spin–lattice relaxation in paramagnetic salts (Van Vleck 1940) there are two important relaxation processes which are considered. The first, the so-called 'direct' process, involves the emission or absorption of a single phonon of the energy corresponding to the splitting $k\Delta$ (whether due to Zeeman or crystalline field effects) between the spin states of the ion. For Zeeman splittings the phonon energy is small in moderate fields, $\sim 0{\cdot}1\,^{\circ}\mathrm{K}$ for a $g=2$ and a field of 1000 gauss. There is, however, a second relaxation process, the so-called 'Raman' process, wherein a phonon is inelastically scattered by the spin and it is the *difference* between the initial and final state phonon energies which is equal to the splitting of the spin states $k\Delta$. The latter process involves all phonons, but primarily those at energy $\sim kT$ because they are most abundant. If $kT \gg$ the splitting, then the Raman process is usually dominant in spin–lattice relaxation.

We now reverse the tables and ask how the thermal resistance of a dielectric salt will be affected by paramagnetic impurities. That is, we must calculate the scattering cross section for phonons in the presence of spin–phonon interactions. We can then find the expected thermal resistance.

It is evident that if the splittings of the spin states $\Delta \ll T$, the direct process will lead to a negligible thermal resistance as the great bulk of phonons which carry the heat will have energy $\sim kT$ and could not be scattered by processes which are limited to phonons of the splitting energy. Thus, thermal resistance due to direct processes will be important for small splittings only at very low temperatures, on the order of $\leqslant \Delta$. However, as Raman process scattering affects all phonons, it can be expected to be the dominant mechanism for providing a significant thermal resistance at higher temperatures.

To gain a semi-quantitative estimate of the effects of Raman processes, we construct a phenomenological Hamiltonian $\mathscr{H}$ coupling the spin system to the lattice (Orbach 1960),

$$\mathscr{H}' = \Gamma \textstyle\sum_{l,j,m}[S_l^z S_l^j + S_l^j S_l^z]\, \epsilon_{zm}{}^{(1)} \epsilon_{mj}{}^{(2)}, \quad . \quad . \quad . \quad . \quad (1)$$

where Γ is a phenomenological coupling constant, S_l^i is the ith component of the spin at the lth lattice site measured in units of $\hbar$, we sum over all spin sites l, and $\epsilon_{ij}^{(\alpha)}$ is i, jth component of strain for the phonon (α). We restrict j to equal either x or y in order that $\mathscr{H}'$ can 'flip' a spin. Equation (1) is then an expression for a Hamiltonian which annihilates or creates phonon (1), flips a spin, and creates or annihilates phonon (2). It applies to spin states which are not Kramer's degenerate in that it predicts a seventh power temperature dependence for the relaxation time.

If we consider Fe^{2+} in $ZnSO_4 . 7H_2O$, the Fe^{2+} will be in a predominantly tetragonal crystalline field with a slight orthorhombic distortion. Together with the spin–orbit coupling, this results in the removal of all orbital and spin degeneracy as the number of electrons is even. Normally, with only a tetragonal field, one would expect a doublet lowest, but the presence of the small orthorhombic term will slightly split the doublet levels. The specific heat measurements of Bailey (unpublished) show that under these considerations, the splitting of the lowest levels (presumably here the doublet levels) is $\Delta \approx 4{\cdot}3$°K. Such a level scheme implies that eqn. (1) has the proper form.

We compute the spin–lattice relaxation time T_1 from eqn. (1) by standard means (Orbach, *loc. cit.*)

$$1/T_1 \cong 90 S^4 \Gamma^2/(\pi^3 \rho^2 v^{10}) \times (kT/\hbar)^7. \qquad \dots\dots \quad (2)$$

Here, ρ is the density, v the phonon velocity (assumed the same for all modes for simplicity), and S the spin value. Likewise, one can easily compute the relaxation time for phonons via the interaction Hamiltonian (1) (Orbach, *loc. cit.*),

$$1/\tau = S^4 \Gamma^2 N_v/(12\pi\rho^2 v^7) \times \{\omega^2[\omega^2 + (k\Delta/\hbar)^2]\} \qquad \dots \quad (3)$$

where there are N_v spin impurities per unit volume, Δ is the splitting between the spin states in °K and ω is the phonon frequency. From a comparison of (3) and (2), it is clear that a short spin–lattice relaxation time T_1 implies a short phonon mean free path $= v\tau$.

If we compute the thermal resistance due to eqn. (3) by the usual methods (Klemens 1958) neglecting questions of thermal equilibrium within the phonon spectrum, we find a thermal resistance W given by,

$$1/W = 4v^6 k\rho^2/(\pi S^4 \Gamma^2 N_v) \times (\hbar/kT)^2$$

$$\times \int \omega^2 \, d\omega \exp(\hbar\omega/kT)/\{[\omega^2 + (k\Delta/\hbar)^2][\exp(\hbar\omega/kT) - 1]^2\}. \qquad (4)$$

For $\Delta \ll T$, this reduces to,

$$1/W \approx 4\rho^2 k v^6/(\pi S^4 \Gamma^2 N_v) \times (\hbar/k\Delta). \qquad \dots\dots \quad (5)$$

From paramagnetic resonance line broadening due to spin–lattice interactions for Fe^{2+} in ZnF_2, Tinkham (1956) found that $T_1 \sim 5 \times 10^{-9}$ sec at

$T=20°\mathrm{K}$. We correct for the difference in sound velocities between ZnF_2 and $ZnSO_4.7H_2O$ and, though the crystalline field effects are quite different, for an order of magnitude estimate we assume the spin–lattice coupling constant Γ stays roughly the same. Then, from (3), we estimate Γ^2, using $\rho=2\,\mathrm{g/cm^3}$, $v=2{\cdot}1\times10^5\,\mathrm{cm/sec}$, and an 'effective' spin $S=\frac{1}{2}$. We find $\Gamma^2\sim10^{-20}\,\mathrm{ergs^2}$. Using this value, the thermal resistance W from eqn. (5) with, say, 5·6% Fe^{2+} in $ZnSO_4.7H_2O$ [i.e. $N_v=2{\cdot}93\times10^{20}$ spins cm^{-3}] $\approx 30\,\mathrm{watts^{-1}\,cm\,deg}$, in very good order of magnitude agreement with the mean experimental value (see figure). According to eqn. (5), W should be temperature independent and directly proportional to the splitting Δ and the concentration N_v.

In fact, for 5·6% Fe^{2+} in $ZnSO_4.7H_2O$, Rosenberg and Sujak find a thermal resistance which is temperature dependent (see figure). Further, the resistance does not appear to be directly proportional to concentration and the temperature dependence seems to vary with concentration. Both these apparent discrepancies can be removed by noting that our calculation of W may have been too naive. If we let $\Delta\to0$, then eqn. (3) will have the same frequency dependence as one would find from impurity scattering, and the thermal resistance as given by eqn. (5) would vanish due to the heat flux of those phonons whose energy is $\ll kT$ not being significantly attenuated. In fact, as Δ is significantly less than T in the experiments of Rosenberg and Sujak, it would appear that just such a spurious effect might be entering here. Two apparently equivalent treatments have been given (Callaway 1959, Berman *et al.* 1959) to remedy such a situation. Both consider that the usually neglected momentum conserving (N) processes tend to bring the low frequency phonons back into equilibrium with the higher frequency phonons (of energy $\geqslant kT$) whose heat flux is much more effectively impeded by the non-momentum conserving processes (in their case, impurity scattering). We follow the treatment of Callaway because of its simplicity. We assume that a phonon of frequency ω has a lifetime τ_N due to N-processes given by

$$1/\tau_N=A\omega(kT/\hbar)^4 \qquad \dots\dots\dots \quad (6)$$

where A is a constant. This is the usual expression for transverse phonons. Longitudinal phonons would obey a law like $1/\tau_N\approx A\omega^3(kT/\hbar)^2$ for an orthorhombic crystal, but, as we are interested in those phonons for which $\omega<kT/\hbar$, the N-process transverse phonon relaxation time (6) is much shorter than the N-process longitudinal phonon relaxation time. We make the rather reasonable assumption that the longitudinal phonons are in equilibrium with the transverse phonons and hence consider (6) as the overall effective N-process relaxation time. Our expression for the thermal resistance W is then, using the formalism due to Callaway,

$$1/W=4v^6k\rho^2/(\pi S^4\Gamma^2N_v)\times(\hbar/kT)^2$$

$$\times\int\omega^3\,d\omega\exp(\hbar\omega/kT)/\{[\omega^3+(k\Delta/\hbar)^2\omega+\alpha(T/\Delta)(kT/\Delta)^3]\,[\exp(\hbar\omega/kT)-1]^2\} \qquad \dots \quad (7)$$

where α is a dimensionless constant giving the relative strength of the momentum conserving processes to the non-momentum conserving Raman processes. Explicitly,

$$\alpha = A(k\Delta/\hbar)\times 12\pi\rho^2 v^7/(S^4\Gamma^2 N_v). \qquad \ldots\ldots \quad (8)$$

Using the approximate theory due to Orbach (*loc. cit.*), we find that $A \sim 10^{-54}\,\mathrm{sec}^4$ utilizing the appropriate elastic properties of $ZnSO_4 . 7H_2O$.

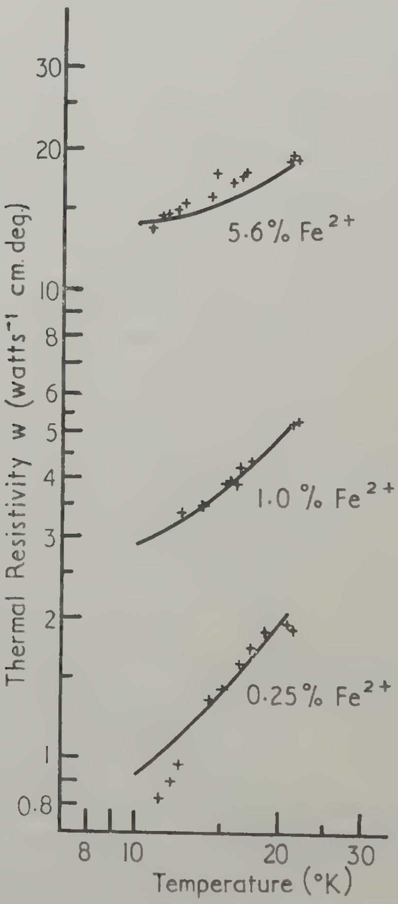

The calculated thermal resistance W due to substitutions of 0·25, 1·0 and 5·6 at. % ferrous sulphate in zinc sulphate given by eqn. (7), plotted against temperature. The crosses are the experimental points of Rosenberg and Sujak (previous paper) for the corresponding salts.

We evaluate the expresion for α for this value of A and for the values of ρ, v, Δ and Γ^2 given above. Respectively for 5·6%, 1% and 0·25% Fe^{2+} in $ZnSO_4 . 7H_2O$, $\alpha = 0{\cdot}001$, $0{\cdot}0056$ and $0{\cdot}022$. Inserting these values in eqn. (7) and evaluating the integral, we find the expected thermal resistance due to spin–phonon interactions in this salt. If we divide our order of magnitude results by a factor of ~ 2 in order to fit the experimental magnitude of W for $5\cdot6\%$ $FeSO_4$ at 10°K we find the theoretical curves of W against temperature T shown in the figure. These are to be compared with the experimental results of Rosenberg and Sujak given in the preceding paper which are also shown in the figure for convenience. Without any further adjustments the temperature dependence of W as predicted by eqn. (7) seems to fit the experimental data rather well for the substitution of $5\cdot6\%$ Fe^{2+}. The predicted change in temperature dependence with concentration and the relative magnitude of the thermal resistance also seem to be in excellent agreement with the experimental results for $1\cdot0$ and $0\cdot25\%$ Fe^{2+} over the measured temperature range.

This agreement would seem to justify our interpretation of the experimental results. In particular, the choice of the phenomenological spin–phonon coupling Hamiltonian (eqn. (1)) to give the corresponding phonon relaxation time (eqn. (3)), and the use of the N-processes to restore thermal equilibrium amongst the phonon modes would both appear to be consistent with the experimental results. Further investigations are planned in other better behaved substances (see preceding paper). It is hoped that the values of Γ and A can then be pinned down more closely and more accurate experimental results can be obtained.

ACKNOWLEDGMENTS

In acknowledgment, the author wishes to thank Professor C. Kittel for the original suggestion of this investigation and Dr. J. M. Ziman for valuable discussions. Appreciation is also due to Drs. W. M. Lomer and R. J. Elliott for their comments on the manuscript, and Mr. M. J. D. Powell who carried out the numerical integrations of eqn. (7).

REFERENCES

BERMAN, R., NETTLEY, P. T., SHEARD, F. W., SPENCER, A. N., STEVENSON, R. W. H., and ZIMAN, J. M., 1959, *Proc. roy. Soc.* A, **253,** 403.
CALLAWAY, J., 1959, *Phys. Rev.*, **113,** 1046.
KLEMENS, P. G., 1958, *Solid State Physics*, Vol. 7 (New York: Academic Press).
ORBACH, R., 1960, Ph.D. Thesis, University of California (unpublished).
ROSENBERG, H. M., and SUJAK, B., 1960, *Phil. Mag.*, **5,** 1299.
TINKHAM, M., 1956, *Proc. roy. Soc.* A, **236,** 535.
VAN VLECK, J. H., 1940, *Phys. Rev.*, **57,** 426.

The Spin of ^{124}Sb and the Spin and Moments of ^{122}Sb

By P. C. B. Fernando†, G. K. Rochester and K. F. Smith
Cavendish Laboratory, Cambridge

[Received August 19, 1960]

The spin of ^{124}Sb and the spin and hyperfine structure of ^{122}Sb have been measured by the atomic beam magnetic resonance method. We find $I_{124}=3$, which verifies Steffen's (1960) β decay scheme for ^{124}Sb, and $I_{122}=2$, in agreement with Pipkin's (1958) independent measurement made by the paramagnetic resonance technique. The $\Delta F=1$ transitions $5/2,\ -1/2 \longleftrightarrow 3/2,\ 1/2$ and $7/2,\ -3/2 \longleftrightarrow 5/2,\ -3/2$ were among those observed in ^{122}Sb, and from these it was deduced that

$$A_{122}=+212{\cdot}01 \pm 0{\cdot}06 \text{ Mc/s} \quad \text{and} \quad B_{122}=+8{\cdot}7 \pm 0{\cdot}5 \text{ Mc/s}.$$

The assignment of the positive sign to A_{122} was made on the basis of the determination of the sign of μ_{121} by Eisinger and Feher (1958), that of μ_{122} by Pipkin (1958), and that of A_{121} by Rochester (1960). The ratio A_{122}/A_{121} is consistent with the ratio g_{122}/g_{121} derived from Pipkin's measurements, but we cannot deduce a value for the hyperfine structure anomaly because the error of $\pm 1\%$ in this g ratio is much greater than a typical s state anomaly (Fernando 1960). The uncorrected quadrupole moment deduced from B_{122} is $Q_{122}=(+0{\cdot}47 \pm 0{\cdot}03) \times 10^{-24}$ cm^2.

References

Eisinger, J., and Feher, G., 1958, *Phys. Rev.*, **109,** 1172.
Fernando, P. C. B., Rochester, G. K., Spalding, I. J., and Smith, K. F., 1960, *Phil. Mag.*, **5,** 1291.
Pipkin, F. M., 1958, *Phys. Rev.*, **112,** 935.
Steffen, R. M., 1960, *Phys. Rev. Letters*, **4,** 290.

---

† Now at University of Columbo, Columbo, Ceylon.

Activation of Single Phonon Infra-red Lattice Absorption in Neutron Irradiated Diamond

By S. D. Smith and J. R. Hardy†
J. J. Thomson Physical Laboratory, University of Reading

[Received October 13, 1960]

Lax and Burstein (1955) have proved that the symmetry of the perfect diamond structure forbids single phonon absorption of radiation. They have also shown that such absorption may be allowed when imperfections are present, since these can provide a local coupling between the fundamental lattice frequencies and the radiation field. They have ascribed the specimen dependent infra-red absorption, shown by natural type I diamonds, to a coupling of this kind. Such an absorption spectrum is shown in the figure (*a*) and one can see that the continuous absorption commences near the maximum lattice frequency which is known from Raman scattering measurements.

We have succeeded in activating a corresponding band in the absorption spectrum of a type II a diamond by fast neutron irradiation. Absorption spectra taken before and after a fast neutron dose of $3 \times 10^{17}/\mathrm{cm}^2$ in a hollow uranium slug of the Harwell BEPO pile are shown in the figure (*b*). That taken prior to irradiation shows the negligible absorption characteristic of type II a crystals. After the irradiation the spectrum shows strong continuous absorption, commencing sharply at the Raman energy and extending to lower frequencies, which can only be explained satisfactorily as single phonon lattice absorption. This effect has not been observed previously, although a number of workers (see Kaiser and Bond 1959 for references) have examined specimens known to contain appreciable numbers of radiation produced defects. Moreover it seems that it is relatively easy to activate this absorption in diamond, compared with silicon, for which Fan and Ramdas (1959) have reported a dose of 10^{19} fast neutrons/cm^2 to be necessary to produce a similar effect. This conclusion is confirmed by the fact that a control specimen of silicon irradiated with the diamond showed no measurable single phonon absorption afterwards.

Kaiser and Bond (1959) have shown that the strengths of the 0·159, 0·148 and 0·139 ev peaks in the type I spectrum are directly proportional to nitrogen content. They have suggested that these peaks are due to absorption by molecular stretching vibrations of the C–N unit. If one compares the two spectra in the figure it is evident that the only marked difference, within the regions of continuous absorption, is in the vicinity of the two strong peaks (X) of the type I spectrum. We see that the 0·148 and 0·139 ev peaks are present in both spectra, although the position of the second peak is slightly influenced by the strength of the first. They are not dependent on the presence of nitrogen and therefore cannot arise from vibrations of C–N units. Their presence and that of the 0·125 ev peak in spectra activated by two very different coupling mechanisms implies that all three arise from maxima in the density of plane wave normal modes of the host lattice, since this is the only common

---

† A.E.I. Research Fellow.

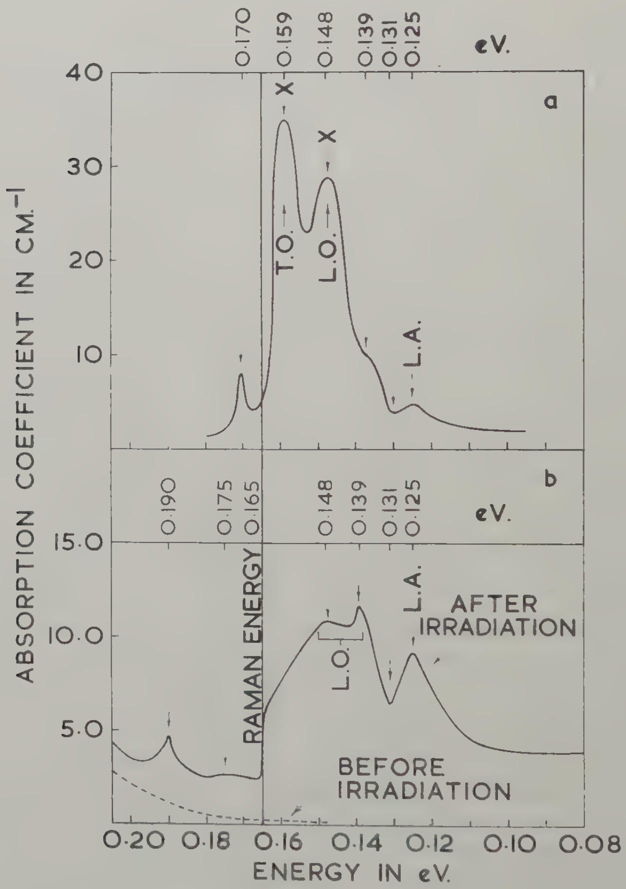

Absorption coefficient versus energy for:

(*a*) A type I diamond.

(*b*) A type II a diamond before and after a dose of 3×10^{17} fast neutrons/cm^2.

The various maxima are assigned to those in the density of normal modes thus : T.O. denotes that arising from the maximum density of transverse optical modes, L.O., that due to maximum density of longitudinal optical modes, and L.A. that associated with the maximum density of longitudinal acoustic modes.

factor involved. However, the 0·159 ev peak is apparently characteristic of the nitrogen impurity. Even so, one cannot regard it as arising from a local C–N vibration since the frequencies involved lie within the band of allowed lattice frequencies and energy absorbed near nitrogen impurities must propagate throughout the crystal, and this is exactly the process envisaged by Lax and Burstein (1955). Either this peak is due to exceptionally strong coupling to relatively few modes, or it corresponds to a sharp maximum in the density of normal modes of the whole lattice. We believe that the second explanation is correct, since one expects the transverse optical (T.O.) modes to show very little dispersion and to produce such a maximum. One way to explain the absence of this peak from the damage induced absorption spectrum is to assume that the coupling involved falls off rapidly close to the Raman frequency. The figure also shows isolated peaks lying above the maximum frequency for which lattice waves can propagate. However, Montroll and Potts (1955) have shown theoretically that vibrational modes localized about lattice imperfections would, if present, occur in this region. The dipole moment associated with such modes could cause the observed absorption. The peaks present in the spectrum of the irradiated diamond have evidently been produced directly by the bombardment and are presumably associated with specific defects (e.g. vacancies and interstitials). This appears to be the first time that such an effect has been observed in any material.

The continuous absorption produced by damage appears to be too strong to be associated solely with isolated point defects. A lower limit to the number required is given by assuming that they provide a coupling as efficient as that due to nitrogen atoms in type I crystals†. If one then considers the 0·148 ev peak, common to both spectra, one finds at least 10^{20} defects/cm^3 to be necessary to produce the observed intensity. This is at least an order of magnitude greater than the number one infers from the dose. Hence we suggest that most of the damage induced activation arises from regions of local disorder which probably involve more than 10^{20} atoms/cm^3.

Since we have associated the absorption peaks with maxima in the density of normal modes we have classified them in the figure according to the branches of the spectrum believed to be responsible (e.g. the 0·148 ev peak is believed to arise from the maximum density of longitudinal optical (L.O.) modes). The 0·139 ev peak is also associated with the L.O. branch. It could correspond to the maximum density of longitudinal acoustic (L.A.) modes, but this implies that the 0·125 ev peak is due to transverse acoustic (T.A.) modes. Since Phillips (1959) has concluded that the T.A. mode energy at the centre of a (111) zone face is 0·063 ev it seems unlikely that there will be a large number of such modes at twice this energy. Consequently if our assignment is correct, the 0·131 ev absorption minimum is associated with a similar feature in the density of L modes.

---

† R. J. Elliott (Clarendon Laboratory Dept., Ref. 23/60) has shown that, however the nitrogen in type I's is present, its extra electron is probably equally shared with the host lattice. The strength of the resultant dipole will then account for that of the 0·159 ev peak. It seems unlikely that irradiation produced point defects provide any more efficient coupling mechanism.

Our suggestion that practically no coupling to the transverse optical (T.O.) modes results from damage appears to be in marked contrast with the silicon results of Fan and Ramdas (1959) since their strong 20·5 micron band would seem, from the inelastic neutron scattering data of Brockhouse (1959), to arise from strong coupling to T.O. modes. We hope to clarify this by studying the activated absorption as a function of dose and annealing time.

We may conclude that activation of absorption in the ‘ one phonon ’ region by damage, strongly supports the theory that it is due to defect induced coupling to the fundamental lattice modes. Furthermore the common features of this and type I absorption indicate that the latter has a similar origin. Differences in detailed shape should thus be explicable in terms of the actual coupling mechanisms involved.

ACKNOWLEDGMENTS

We should like to thank Dr. E. W. J. Mitchell and Dr. C. D. Clark of this laboratory for valuable discussions during the course of this work, Mr. W. H. Wynd of A.E.R.E., Harwell, for irradiating the specimen, and one of us (S. D. S.) wishes to thank the C.E.G.B. for financial support.

REFERENCES

BROCKHOUSE, B. N., 1959, *Phys. Rev. Letters*, **2**, 256.
FAN, H. Y., and RAMDAS, A. K., 1959, *J. appl. Phys.*, **30**, 1127.
KAISER, W., and BOND, W. L., 1959, *Phys. Rev.*, **115**, 857.
LAX, M., and BURSTEIN, E., 1955, *Phys. Rev.*, **97**, 39.
MONTROLL, E. W., and POTTS, R. B., 1955, *Phys. Rev.*, **100**, 525.
PHILLIPS, J. C., 1959, *Phys. Rev.*, **111**, 147.

REVIEWS OF BOOKS

Figures of Equilibrium of Celestial Bodies. By ZDENEK KOPAL. (University of Wisconsin Press, 1960.) [Pp. 135.] $3.

INVESTIGATIONS into the shapes, gravitational fields, moments of inertia, oscillations, etc. of approximately spherical masses like the planets have led to important work by Clairaut, Laplace, Stokes and many other experts. This branch of applied mathematics has come into prominence recently on account of the use of gravity surveying and satellite orbits in the study of the shape of the Earth.

In the first of the three principal sections of his book, Professor Kopal presents a treatment of the problem on classical lines, based on the idea of a general disturbing potential, and using expansions in harmonic functions. In particular, the disturbing potential is taken as one representing the rotation of the body, or as one corresponding with equilibrium-tidal influences of an external mass.

Professor Kopal then extends the treatment to the second order of the distortions. In the third principal section, he considers ' interaction phenomena ' connected with the essential non-linearity of the equations for the rotating body under tidal forces : at this stage, needless to say, the formulae become extremely complicated.

Much of the advanced work set out in the book is the result of the investigations of Professor Kopal himself.

There is also a short section dealing with dynamical considerations under the title ' non-radial oscillations '.

Formulae connected with the external potential of the Earth are of course fundamental in the geodetic applications of artificial satellites, but the book contains no treatment of satellite orbits, and the second part of the title referring to ' motion of artificial satellites ' may therefore be a little misleading.

J. E. J.

[*The Editors do not hold themselves responsible for the views expressed by their correspondents.*]

Fig. 2

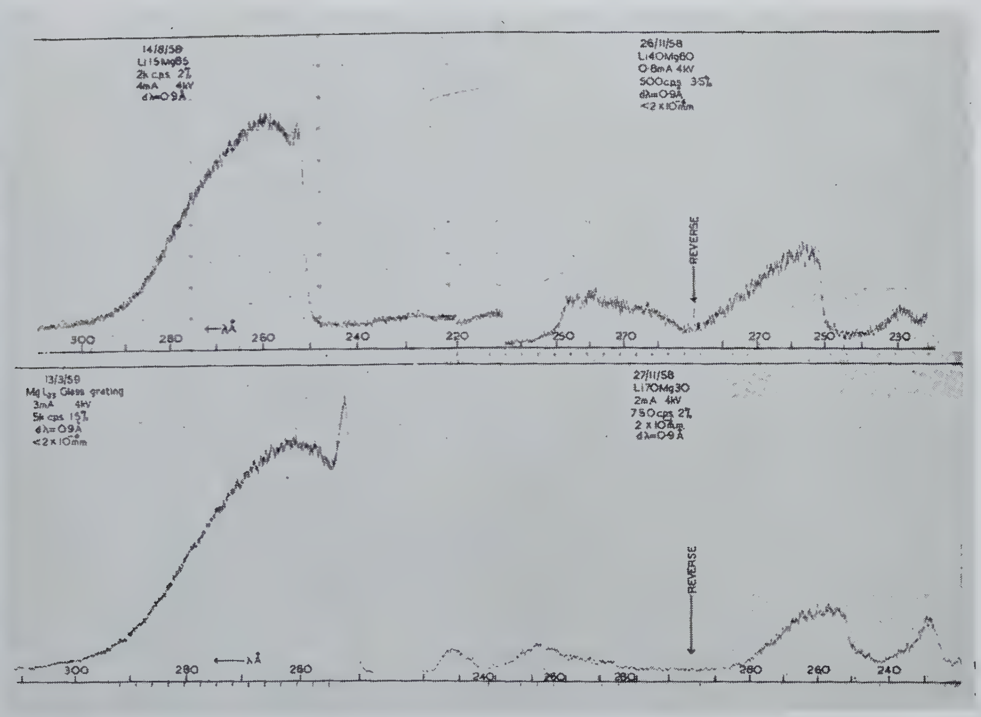

L_{23} spectra of pure Mg and Mg in Li15Mg85, Li40 Mg60 and Li70Mg30 alloys. Li K spectra for Li40Mg60 and Li70Mg30 alloys, in which cases the lead screw drive was reversed and the spectra retraversed to show the effect of contamination. In the Li70Mg30 alloy the Mg L_{23} has been replaced by the Li ‘ line ’ after reversal.

Fig. 3

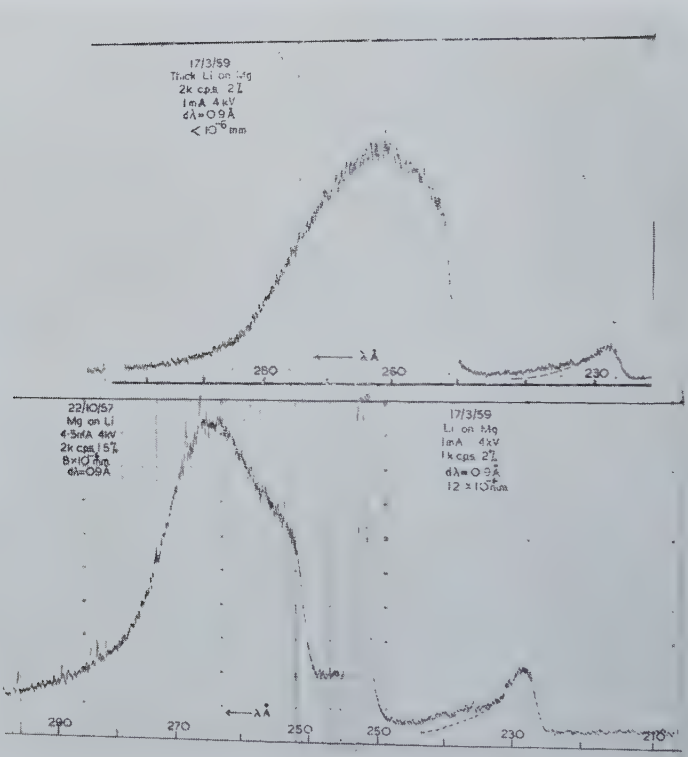

Mg L_{23} spectra for Li deposited on Mg and Mg deposited on Li. Two Li K spectra for Li on Mg. Profile of the normal Li K spectrum is shown by the broken lines.

Fig. 4

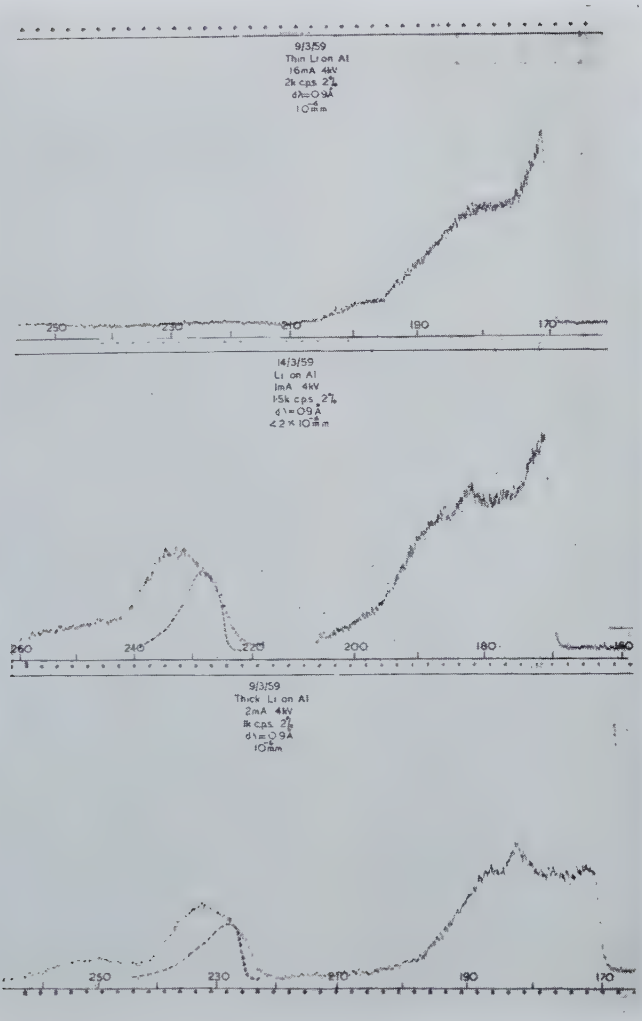

Al L_{23} spectra for ‘ thin ’, ‘ medium ’ and ‘ thick ’ coats of Li on Al and Li K spectra for ‘ medium ’ and ‘ thick ’ coats. Profile of the normal Li K spectrum is shown by broken lines.

Fig. 5

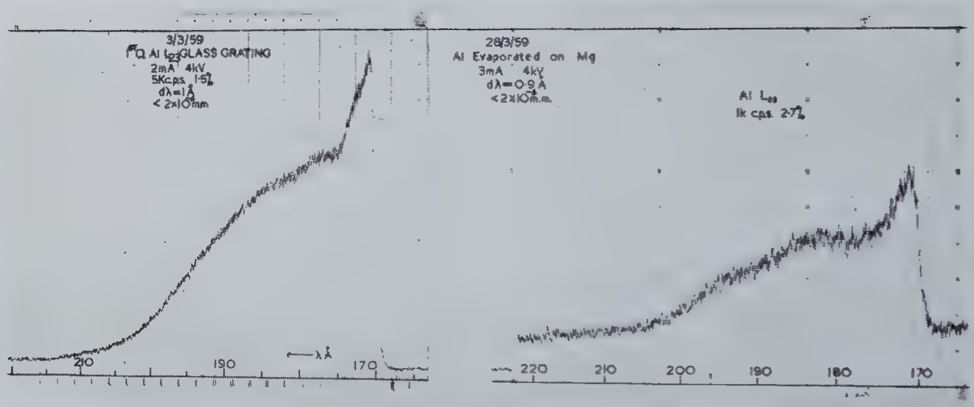

Al L_{23} spectra from pure Al and Al deposited on Mg. ($d\lambda$ for the pure Al should be 0·9 Å not 1 Å.)

Fig. 1

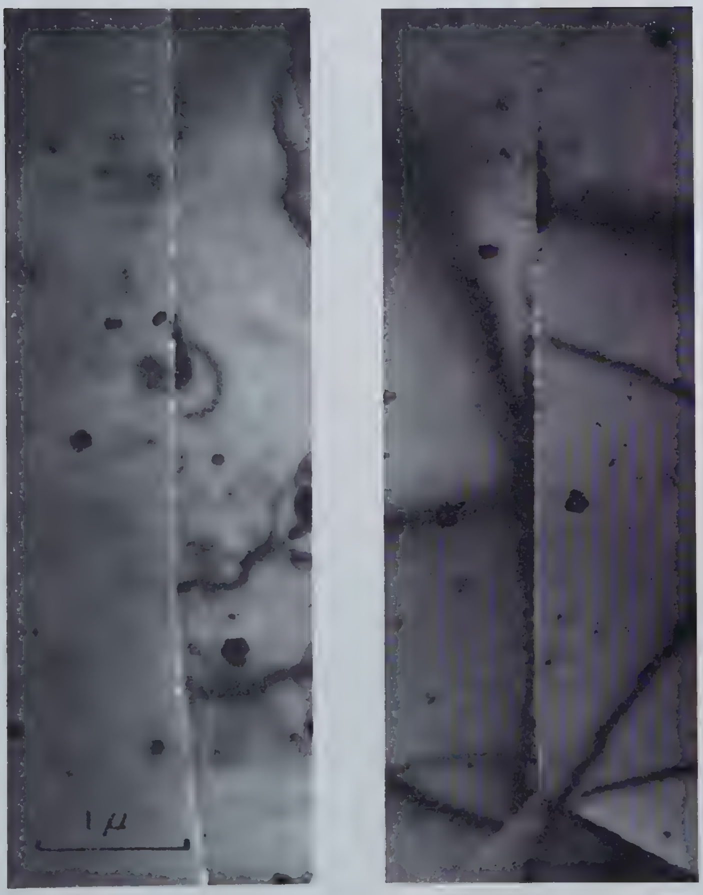

(*a*) (*b*)

Surface pits at the grain boundaries of a thin aluminium foil. ×20 000.

Fig. 2

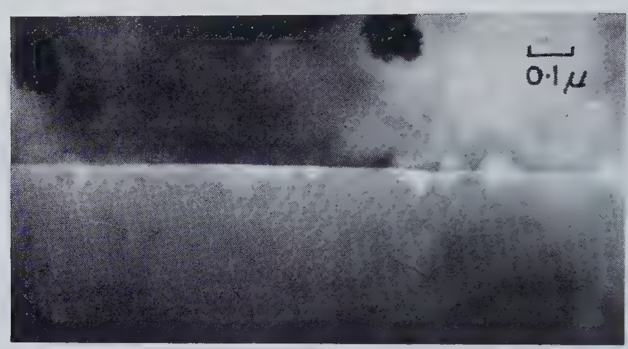

Surface pits at the grain boundaries of a thin aluminium foil. ×60 000.

Fig. 3

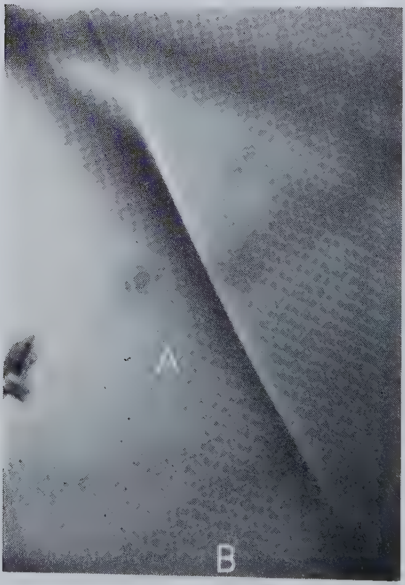

Grain boundary of aluminium foil before ageing. ×40 000.

Fig. 4

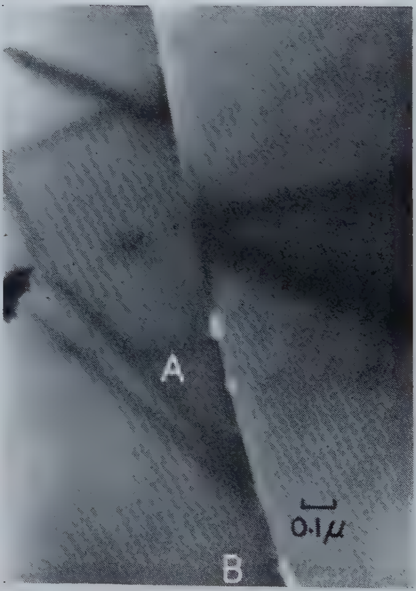

The boundary of fig. 3 after ageing. ×40 000.

Fig. 5

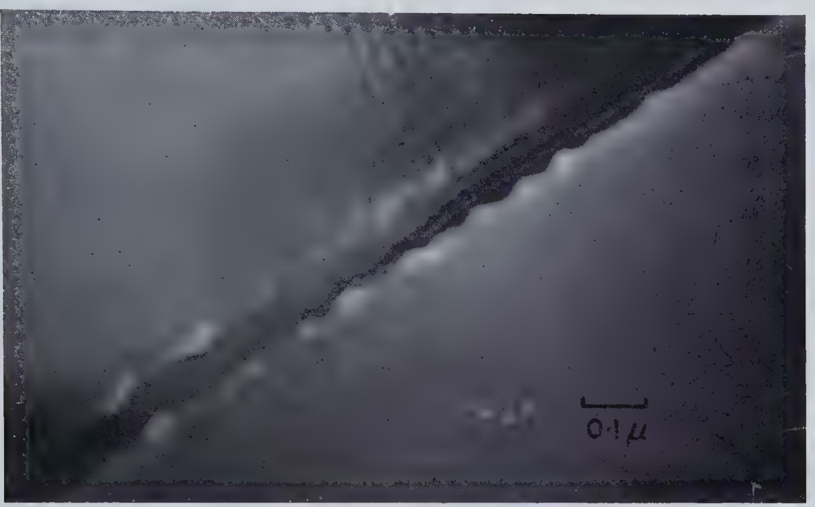

Pits at both surfaces of a thin aluminium foil. × 80 000.

Fig. 6

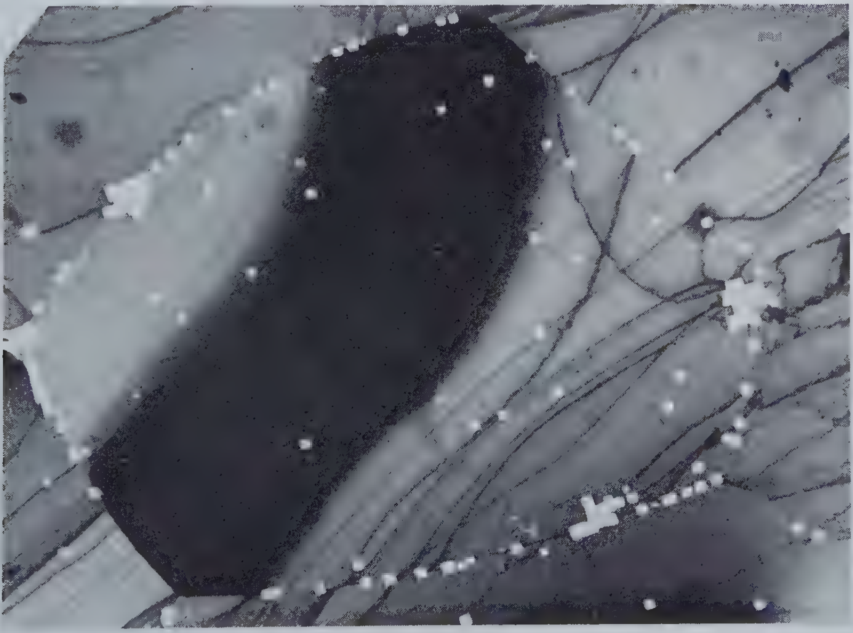

Etch pits in a thin aged aluminium foil. × 4000.

Fig. 1

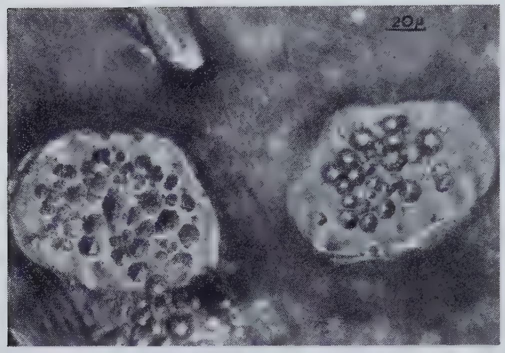

Large etch pits containing smaller hexagonal pits on the basal surface of ice grown from the melt. (Replica.)

Fig. 2

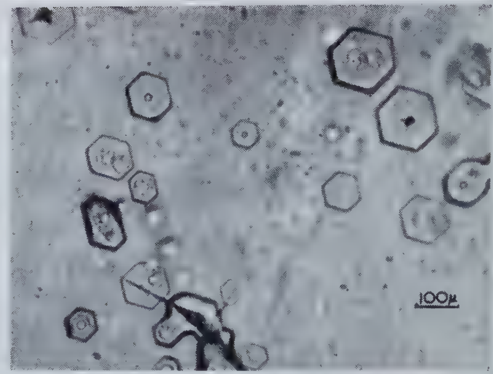

Hexagonal etch pits on the basal face of ice.

Fig. 3

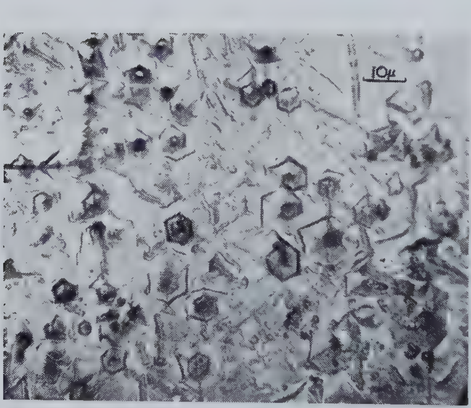

Replica of basal plane showing spiral steps on etch pits. (Replica.)

Fig. 4

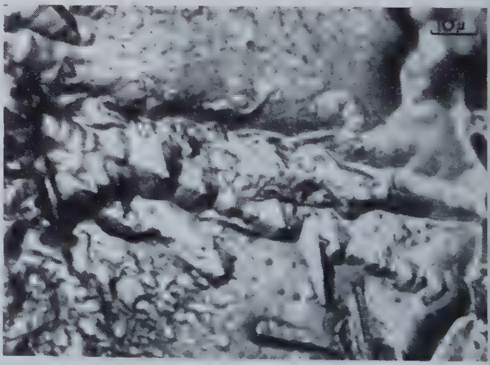

A line of pyramidal etch pits along a low-angle grain boundary. (Replica.)

Fig. 5

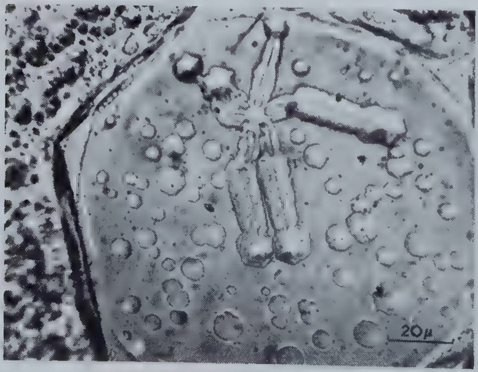

Etch channels on basal surface initiated by an included dust particle and terminating in etch pits. (Replica.)

Fig. 6

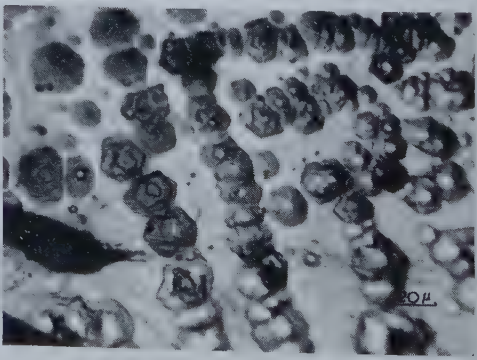

Pyramidal hillocks showing concentric and spiral steps on the basal face of an ice crystal grown from the vapour. (Replica.)

Fig. 7

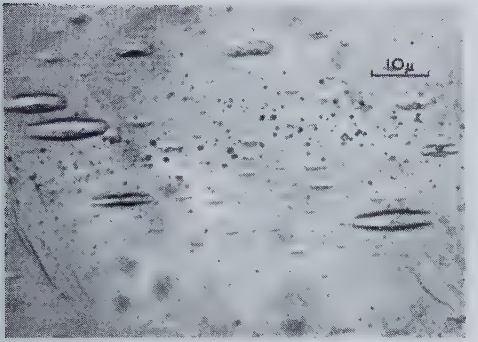

Elongated etch pits on the prism face of an ice crystal grown from the vapour. (Replica.)

Fig. 8

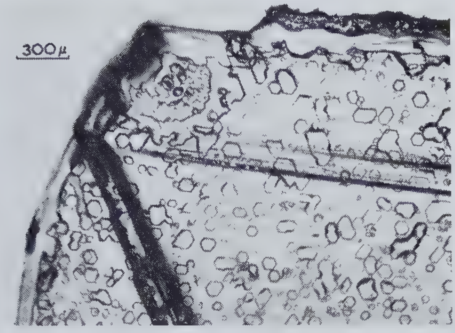

A high concentration of hexagonal etch pits on the basal surface of a plate-like crystal grown from the vapour.

Fig. 9

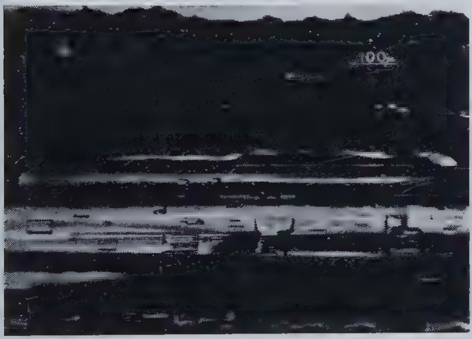

Rectangular etch pits on the prism faces of an ice needle.

Fig. 10

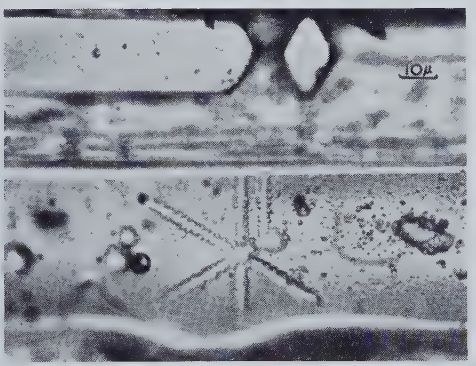

Etch channels radiating from an impurity speck in a plate-like crystal grown from the vapour. Each channel consists of a double row of small etch pits which probably represent the intersection of dislocation loops with the surface. (Replica.)

Fig. 11

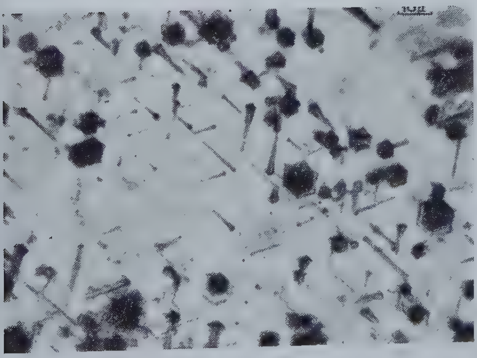

Etch channels oriented along the $\langle 11\bar{2}0\rangle$ directions on the basal plane produced by the movement of dislocations under mechanical vibration at −20°c (Replica.)

Fig. 12

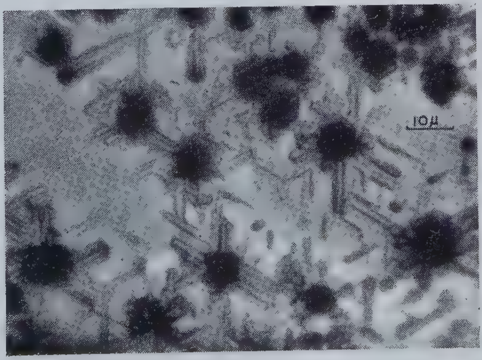

'Rosettes' produced by dropping lead shot on a basal surface of ice at −20°c. (Replica.)

Fig. 1

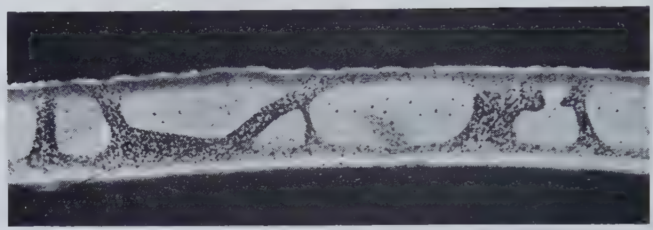

Cross section of a 0·001 in. copper foil after an anneal of 2 hours at 800°c to show the formation of helium bubbles near the grain boundaries. ×550.

Fig. 2

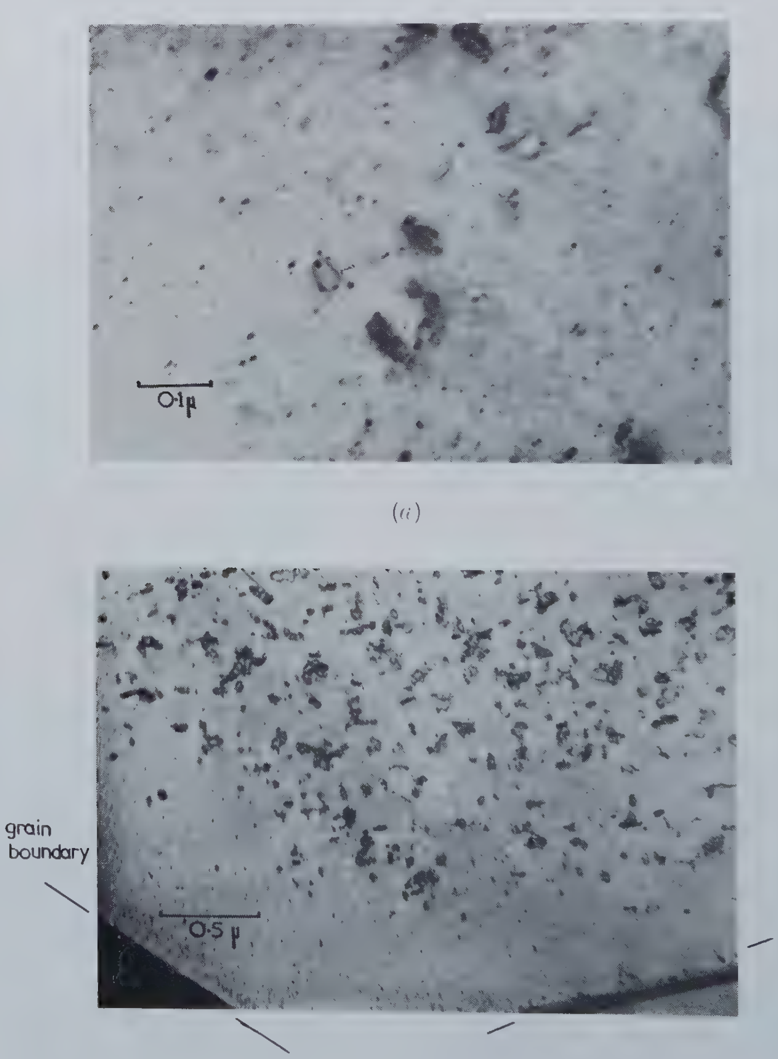

(a)

(b)

Two films of copper (a) and (b) through which $1{\cdot}4\times10^{17}$ alpha-particles cm^{-2} (32 μ amp hr.) have passed.

Fig. 3

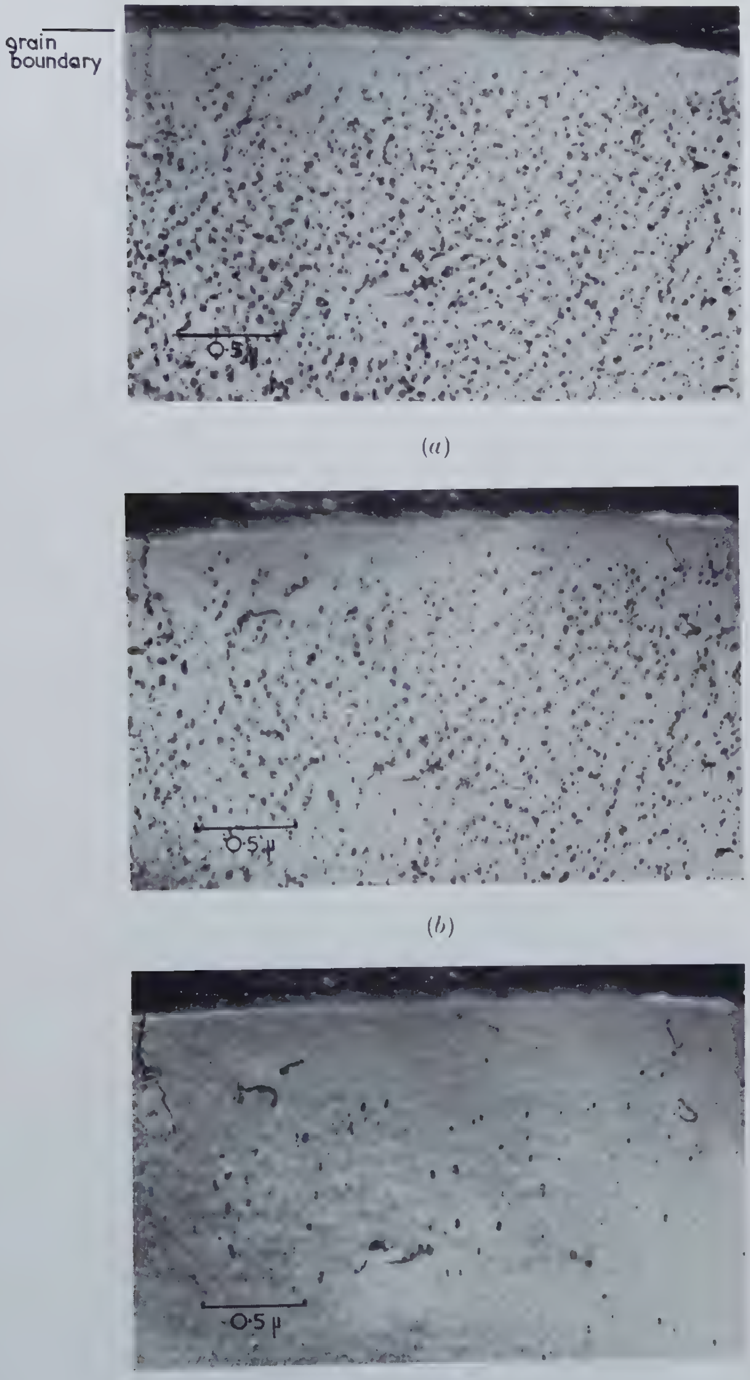

(*a*)

(*b*)

(*c*)

Three successive photographs (*a*) $t=0$; (*b*) $t=15$ min ; (*c*) $t\simeq 20$ min showing annealing of damage in a copper film while at about 350°c on the ‘ hot-stage ’ of the electron microscope.

Fig. 4

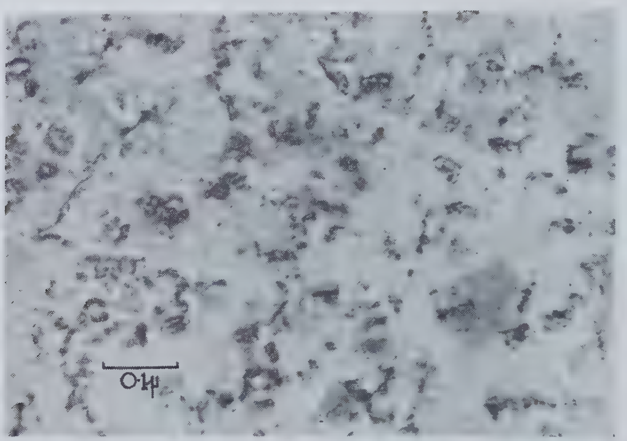

A thin film of copper containing helium atoms after bombardment with $1 \cdot 4 \times 10^{17}$ alpha-particles cm^{-2}.

Fig. 5

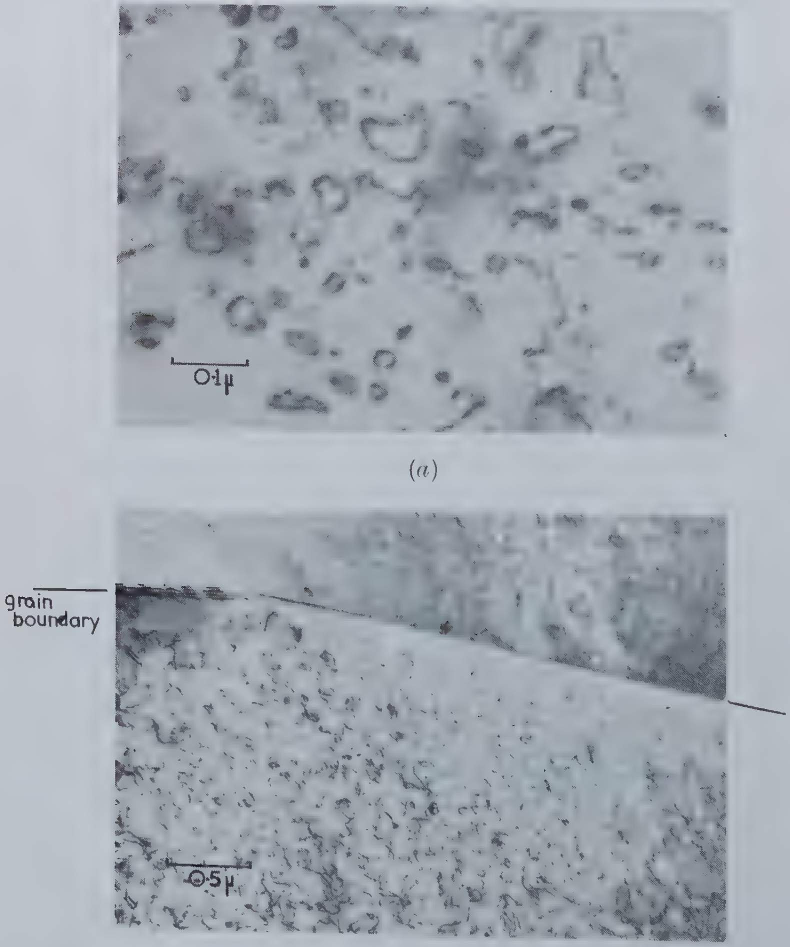

(a)

(b)

Fig. 5 (*continued*)

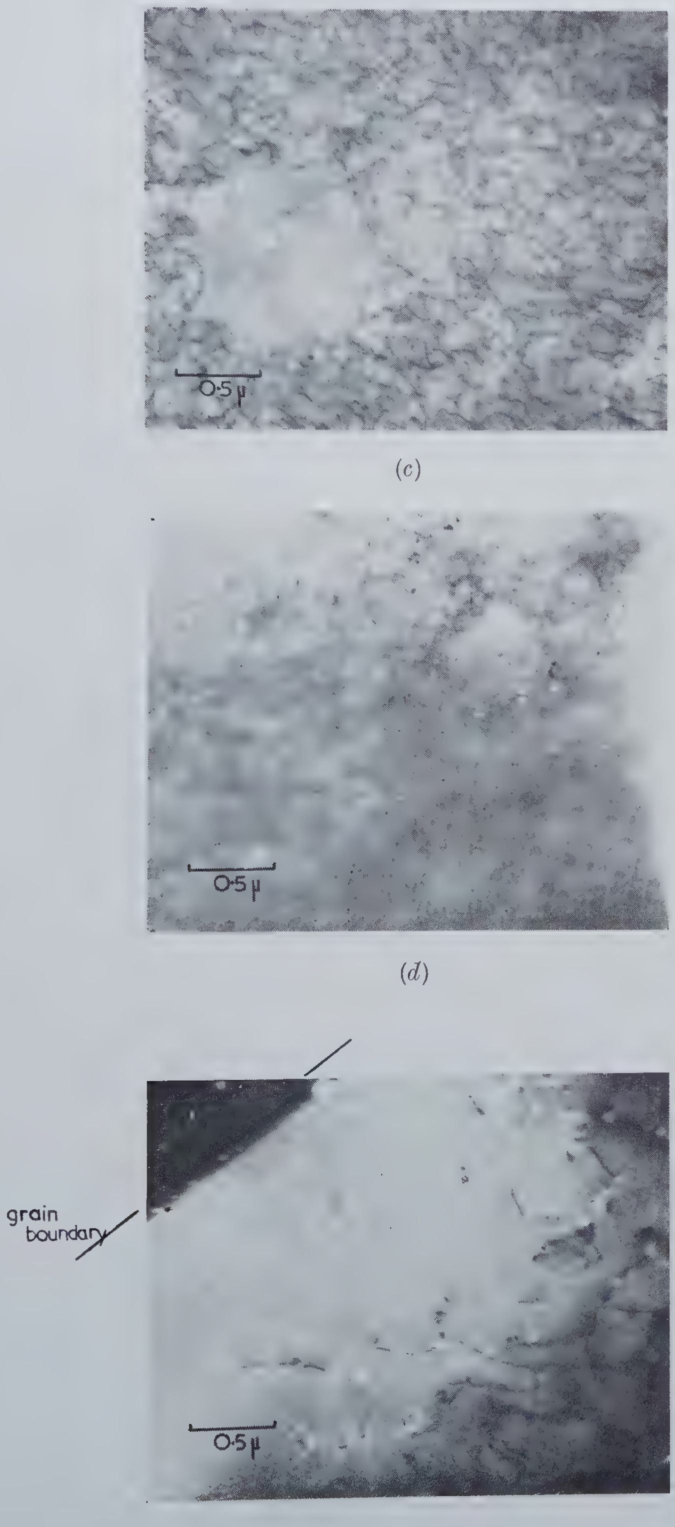

(*c*)

(*d*)

(*e*)

Copper films similar to that in fig. 4 but after (*a*) a 2-hour anneal at 350°c *in vacuo*, (*b*) 2 hours at 450°c, (*c*) 1 hour at 750°c, (*d*) as for (*c*) but with the dislocations out of contrast, (*e*) 2 hours at 750°c, near a grain boundary (7×10^{16} alpha-particles cm^{-2}).

Fig. 3

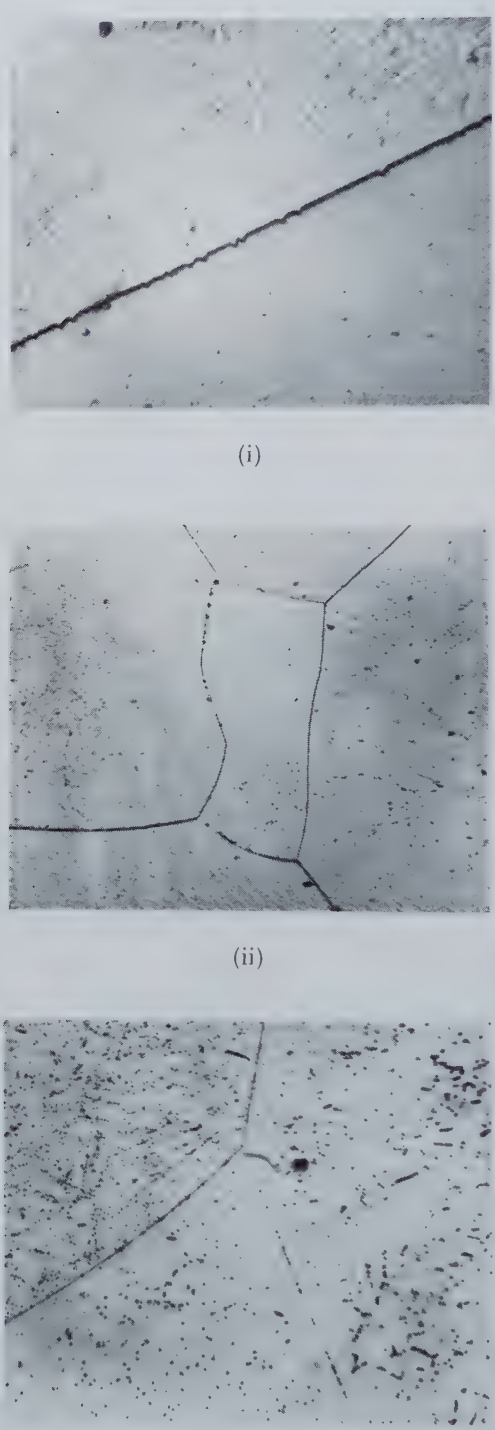

(i)

(ii)

(iii)

Typical micrographs of the alloys (×250).
(i) 1·91 at. % chromium (F.R.I./B.M.I.);
(ii) 12·1 at. % chromium (J.M./J.M.);
(iii) 38·5 at. % chromium (F.R.I./U.S.B.M.).

SUBJECT INDEX

PAGE
Adsorbed gas films, study by electron diffraction 222
Aluminium:
  copper alloys, effect of quenching 200
  copper alloys, segregation of solute 1119
  dislocations in quenched 1, 24
  electropolishing, retention of vacancies 101
  etching of strained 709
  kinetics of ordering Fe_3Al 343
  pitting after ageing 1217
  point defects, movement during fatigue 1147
  point defects induced 1247
  unloading effects: also aluminium–zinc 947
Anisotropy of inertia mass 409
Argon, refractive indices, liquid and solid 355

Beryllium, etching of substructures 1195
Beryllium, internal friction peaks 325
Binary alloys, eutectic composition and immiscibility 383
Binary alloys, residual resistance 753
Brass, alpha-, creep 649
Brass, alpha-, stress corrosion cracking 1029
Brass, beta, nuclear magnetic resonance 899
Bubble chamber, liquid hydrogen 146, 154
Book notices 200, 648, 980, 1202
Book reviews 104, 194, 302, 421, 647, 763, 871, 975, 1201, 1315

Cadmium crystals, growth from vapour 473
Chromium, heat capacity anomaly 188
Copper:
  aluminium, segregation of solute 1119
  dilute alloys, internally oxidized 298
  point defects induced 1247
  silicon, internal oxidation, damping, capacity 140
  strain broadening, magnetic resonance lines 843
  thermoelectric power, pure 765
Cosmic rays:
  abundance of heavy nuclei 311
  extensive air showers 305
  flux of protons 1105
  intensity, interplanetary field 601
  muon decay, γ internal conversion 297
  primary alpha, flux and spectrum 1151
  solar daily variation 585
Cracks in magnesium oxide 407, 697
Creep, micro, in zinc whiskers 417
Creep in f.c. metals and α-brasses 649
Cyclotron resonance in lead 1001

de Haas–van Alphen effect 105, 115
Diamagnetic shielding of nuclei in metals 529
Diamond, single phonon infra-red lattice absorption 1311
Diamonds, semiconducting, infra-red absorption 127
Diffusion in metals 803, 1171

PAGE

Dislocations:
  aluminium, quenched substructure 24
  and etch pits in ice 1221
  angular 161
  bismuth and antimony tellurides 729
  charged, lithium fluoride 815
  formation by vacancy collapse 43, 669, 1203
  locking in α-iron 30
  magnesium oxide 192
  prismatic loops 1, 921, 1255
  quarter, talc 533
  silver, cold worked 485
  silver bromide, Burgers vector $a\langle 100\rangle$ 799
  silver bromide, loops 445
  zinc, climb of loops 873

Electrical resistance, iron aluminium 451
Electrical resistance, residual binary, alloys 753
Electrical resistivity, stacking faults 251
Electrical resistivity, quenched-in recovery, gold 687
Electron absorption, metal foils 967
Electron diffraction, absorbed gas films 222
Electron Fermi energy and work function 64

Fermi surface in white tin 1089
Ferromagnetism in palladium–iron alloys 335
Fracture, ductile, shear component 759

Gold, cobalt precipitation, magnetic study 1127
Gold, diffusion of platinum, atomic 803
Gold, quench hardening 939
Gold, quenched-in resistivity recovery 687
Graphite, radiation damage 621

Hall effect, liquid and solid mercury 100

Indium arsenide, thermal conductivity 84, 887
Internal friction, sodium chloride 425
Interstitial atoms in f.c.c. metals 853
Ionospheric drifts statistical theory 553
Iron:
  alpha, Debye–Waller factor 1229
  alpha, dislocation locking 30
  aluminium, electrical resistance 451
  kinetics of ordering Fe_3Al 343
  nickel films, microtwinning 373
  palladium, ferromagnetism 335
Irradiation:
  alpha, induced point defects 1247
  electron, damage in graphite 1049
  electron, hardening of lithium fluoride 237
  electron and neutron, optical absorption, sapphire 1013
  neutron, damage in graphite 621
  neutron, damage and recovery in tungsten 278
  neutron, embrittlement of molybdenum 413
Ising model, magnetic properties 909
Isotopic spin selection rules 359, 365

PAGE

Krypton, solid, density and expansivity 186

Lead, cyclotron resonance 1001
Lead, density of states 70
Lead iodide crystals, decomposition 787
Lithium and Li–Mg alloys, nuclear magnetic resonance 467
Lithium, metallic, K emission 525
Lithium fluoride, charged dislocations 815
Lithium fluoride, hardening by irradiation 237
Lithium fluoride, mechanical properties 981

Magnesium oxide, cracks 407, 697
Magnesium oxide, deformed 991
Magnesium oxide, dislocations 192
Magnetic properties of the Ising model 909
Magnetic recording tapes, anhysteretic remanence 717
Magnetic study, gold–cobalt 1127
Magnetic susceptibility, vanadium–chromium 1267
Magnetoresistance, copper, silver and gold 111, 304
Mercury, Hall effect 100
Molybdenum, embrittlement by irradiation 413

Neutron scattering, effect of lattice distortion 1235
Nickel, annealing of deformed 499
Nickel, iron films, epitaxial, microtwinning 373
Nuclear interactions, 5·7 Bev protons 537
Nuclear magnetic resonance, β brass, Li and Li–Mg 467, 899
Nuclear magnetic resonance lines, strain broadening, copper 843
Nuclear scattering, optical model 1181
Nuclei :
  diamagnetic shielding in metals 529
  hyperfine structure, ^{209}Bi, ^{121}Sb, ^{123}Sb 1281, 1291
  isotopic spin selection rules 359, 365
  spin, ^{124}Sb and ^{122}Sb 1309

Optical constants, liquid silver 272
Optical transitions in alloys, selection rules 757

Permalloy, films, cross-tie walls 625
Photographic processes in crystals 723
Platinum, atomic diffusion in gold 803
Platinum, point defects 201
Polymers, fine structure of films 78
Precipitates, growth from solid solutions 176

Quench hardening, gold 939

Rock magnetism, carboniferous system 675, 1087
Rock magnetism, statistical methods 523
Rubber, fine structure of films 78

PAGE

Scattering of phonons by spin 1299, 1303
Silver:
  cold worked, annealing 833
  Debye–Waller factor 1229
  evaporated, defects 571
  Liquid, optical constants 272
Silver bromide, dislocations 445, 799
Silver chloride, photographic processes 723
Silver chloride, reverse bending 441
Sodium chloride, embrittlement, stress concentrations . . . 1197
Sodium chloride, internal function 425
Sodium chloride, lattice vibrations 859
Spectra, absorption, details in crystals 691
Spectra, X-ray emission, metals and alloys. . . . 525, 1161, 1205
Spin density fluctuations, giant 1193
Stacking faults, electrical resistivity 251
Stored energy, calculation, deformed isotropic material . . . 519
Stored energy, cold worked silver 485
Stored energy, deformed nickel 499
Stress corrosion cracking in alloys 1029

Thermal conductivity, germanium, silicon and indium arsenide . . 84
Thermal conductivity, impure indium arsenide 887
Thermoelectricity, below 1°K 867
Thermoelectric power, alkali metals, phonon component . . . 1059
Thermoelectric power, pure copper 765
Thin films, thermal aspects of growth 1041
Tin, white, Fermi surface 1089
Tungsten, elastic and thermal properties 927
Tungsten, neutron irradiated 278

Vacancies in metals, generation 635

Yield and flow stress in b.c.c. metals 745

Zinc, pyramidal glide and dislocation loops 873
Zinc, whiskers, microcreep 417
Zirconium, elastic and thermal properties 927

INDEX OF AUTHORS (WITH TITLES)

PAGE

Alston, Margaret H., Cundy, D. C., Evans, W. H., Newport, R. W., and Williams, P. R.: A 10 in. diameter liquid hydrogen bubble chamber. 146
Amelinckx, S., and Delavignette, P.: Direct evidence for the presence of quarter-dislocations in talc monocrystals 533
Amelinckx, S., with Delavignette, P.: Dislocation nets in bismuth and antimony tellurides 729
Anderson, E., with Hume-Rothery, W.: Eutectic compositions and liquid immiscibility in certain binary alloys. 383
Ashby, M. F., and Smith, G. C.: Direct electron microscopy of thin foils of internally oxidized dilute copper alloys 298
Aubrey, J. E.: Cyclotron resonance in lead 1001

Bailey, J. E., and Hirsch, P. B.: The dislocation distribution, flow stress, and stored energy in cold-worked polycrystalline silver. . . . 485
Bailey, J. E.: Electron microscope observations on the annealing processes occurring in cold-worked silver 833
Bailyn, M.: The phonon drag component of the thermoelectric power of the alkali metals at low temperatures. 1059
Barnes, R. S.: The generation of vacancies in metals 635
Barnes, R. S., and Mazey, D. J.: The nature of radiation-induced point defect clusters 1247
Bartlett, J. T., and Mitchell, J. W.: The generation of dislocation loops at the surfaces of crystals of silver bromide. 445
Bartlett, J. T., and Mitchell, J. W.: Dislocations with Burgers vectors of $a\langle 100\rangle$ in crystals of silver bromide 799
Bassett, G. A., and Edeleanu, C.: Etching of strained aluminium . 709
Bassett, G. A., and Edeleanu, C.: Pitting of aluminium at grain boundaries after ageing 1217
Beaumont, R. H., Chihara, H., and Morrison, J. A.: An anomaly in the heat capacity of chromium at 38·5°c 188
Belshé, J. C., with Everitt, C. W. F.: Palaeomagnetism of the British carboniferous system 675, 1087
Blount, E. I., with Cohen, M. H.: The g-factor and de Haas–van Alphen effect of electrons in bismuth 115
Bollmann, W.: Electron-microscopic observations on radiation damage in graphite 621
Bradley, E. F., and Porter, N. A.: Observations on extensive air showers. VIII: The distribution in declination and curvature of the shower front 305
Bryant, G. W., and Mason, B. J.: Etch pits and dislocations in ice crystals 1221
Buck, B., Maddison, R. N., and Hodgson, P. E.: Optical model analysis of nuclear scattering 1181
Bullough, R., and Newman, R. C.: The spacing of prismatic dislocation loops 921
Burbank, R. D., and Heidenreich, R. D.: Microtwinning in epitaxial nickel–iron films 373
Burke, J.: The kinetics of the growth of precipitates from solid solutions. 176
Burley, D. M.: Some magnetic properties of the Ising model . . 909

PAGE

Cahn, R. W., and Davies, R. G.: X-ray evidence for segregation of solute to stacking faults in a copper–aluminium alloy 1119
Cahn, R. W., with Feder, R.: Kinetics of ordering in Fe_3Al . . . 343
Cahn, R. W., and Feder, R.: The electrical resistance of iron–aluminium alloys and its dependence on crystallographic order 451
Chihara, H., with Beaumont, R. H., and Morrison, J. A.: An anomaly in the heat capacity of chromium at 38·5°C 188
Childs, B. G., Gardner, W. E., and Penfold, J.: The magnetic susceptibility of vanadium–chromium solid solutions 1267
Ciccarello, I. S., Palma-Vittorelli, M. B., and Palma, M. U.: An electron spin resonance investigation of photographic processes in crystals of AgCl containing traces of CuCl 723
Clark, C. D., Kemmey, P., and Mitchell, E. W. J.: The infra-red absorption of hot semiconducting diamonds 127
Clarke, F. J. P., and Sambell, R. A. J.: Micro-cracks and their relation to flow and fracture in single crystals of magnesium oxide . . 697
Codd, I., and Petch, N. J.: Dislocation-locking by carbon, nitrogen and boron in α-iron 30
Cohen, M. H., and Blount, E. I.: The g-factor and de Haas–van Alphen effect of electrons in bismuth 115
Copley, G. J., with Feltham, P.: Creep in face-centred metals and solid solutions with reference to α-brasses 649
Conrad, H.: Effect of temperature on yield and flow stress of b.c.c. metals 745
Crangle, J.: Ferromagnetism in Pd-rich palladium–iron alloys . . 335
Crisp, R. S.: Soft x-ray emission from potassium metal in the 40–1000 Å range 1161
Crisp R. S., and Williams, S. E.: The K emission spectrum of metallic lithium 525
Crisp, R. S., and Williams, S. E.: The soft x-ray spectra of lithium, magnesium and aluminium and their alloys 1205
Cundy, D. C., with Alston, Margaret H., Evans, W. H., Newport, R. W., and Williams, P. R.: A 10 in. diameter liquid hydrogen bubble chamber 146
Cundy, D. C., Evans, W. H., Hadley, D. W., Mason, P., Newport, R. W., Smith, J. R., and Williams, P. R.: Systematic track distortion in a 10 in. diameter liquid hydrogen bubble chamber 154
Cusack, N. E., with Kendall, P. W.: Hall effect in liquid and solid mercury 100

Das, T. P., and Sondheimer, E. H.: Diamagnetic shielding of nuclei in metals 529
Davies, R. G., with Cahn, R. W.: X-ray evidence for segregation of solute to stacking faults in a copper–aluminium alloy 1119
Delavignette, P., with Amelinckx, S.: Direct evidence for the presence of quarter-dislocations in talc monocrystals 533
Delavignette, P., and Amelinckx, S.: Dislocation nets in bismuth and antimony tellurides 729
Dickson, E. W.: The observation of sharp internal friction peaks in beryllium 325
Dougherty, J. P.: A statistical theory of ionospheric drifts . . . 553
Drever, R. W. P.: Upper limit to anisotropy of inertial mass from nuclear resonance 409
Duke, P. J.: The variation with time of the flux and energy spectrum of primary cosmic ray alpha particles 1151

PAGE
Edeleanu, C., with Bassett, G. A.: Etching of strained aluminium . 709
Edeleanu, C., with Bassett, G. A.: Pitting of aluminium at grain boundaries after ageing 1217
Edeleanu, C., and Forty, A. J.: Some observations on the stress-corrosion cracking of α-brass and similar alloys 1029
Elbaum, C.: On dislocations formed by the collapse of vacancy discs 669, 1203
Elliot, H.: Cosmic-ray intensity variations and the interplanetary magnetic field 601
Englman, R.: Localized modes in crystals and sharp details of the optical absorption spectra 691
Evans, W. H., with Alston, Margaret H., Cundy, D. C., Newport, R. W., and Williams, P. R.: A 10 in. diameter liquid hydrogen bubble chamber 146
Evans, W., with Cundy, D. C., Hadley, D. W., Mason, P., Newport, R. W., Smith, J. R., and Williams, P. R.: Systematic track distortion in a 10 in. diameter liquid hydrogen bubble chamber . 154
Everitt, C. W. F., and Belshé, J. C.: Palaeomagnetism of the British carboniferous system 675, 1087

Faulkner, E. A.: Calculation of stored energy from broadening of x-ray diffraction lines 519
Faulkner, E. A.: Strain-broadening of nuclear magnetic resonance lines in copper 843
Feder, R., and Cahn, R. W.: Kinetics of ordering in Fe$_3$Al . . . 343
Feder, R., with Cahn, R. W.: The electrical resistance of iron–aluminium alloys and its dependence on crystallographic order 451
Feltham, P., and Copley, G. J.: Creep in face-centred metals and solid solutions with special reference to α-brasses 649
Fernando, P. C. B., Rochester, G. K., and Smith, K. F.: The spin of ^{124}Sb and the spin and moments of ^{122}Sb 1309
Fernando, P. C. B., Rochester, G. K., Spalding, I. J., and Smith, K. F.: The hyperfine structure of ^{121}Sb and ^{123}Sb 1291
Figgins, B. F., and Smith, B. L.: Density and expansivity of solid krypton 186
Fine, M. E., with Freise, E. J., and Kelly, A.: The effect of electropolishing on the retention of vacancies during quenching in Al and Al alloys 101
Forty, A. J.: Observations of the decomposition of crystals of lead iodide in the electron microscope 787
Forty, A. J., with Edeleanu, C.: Some observations on the stress-corrosion cracking of α-brass and similar alloys 1029
Freise, E. J., Fine, M. E., and Kelly, A.: The effect of electropolishing on the retention of vacancies during quenching in Al and Al alloys . 101

Gafner, G.: Thermal aspects of the growth of thin films by vacuum sublimation 1041
Gardner, W. E., with Childs, B. G., and Penfold, J.: The magnetic susceptibility of vanadium–chromium solid solutions 1267
Gaunt, P.: A magnetic study of precipitation in a gold–cobalt alloy . 1127
Germer, L. H., Scheibner, E. J., and Hartman, C. D.: Study of adsorbed gas films by electron diffraction 222
Goggin, P. R., with Reynolds, W. N.: The annealing of electron irradiation damage in graphite 1049
Gibbons, T. B., and O'Hara, S.: The effect of internal oxidation on the damping capacity of copper–silicon alloys 140

PAGE

Gold, A. V.: The density of states in lead . . . 70
Gold, A. V., MacDonald, D. K. C., Pearson, W. B., and Templeton, I. M.: The thermoelectric power of pure copper . . . 765
Gold, A. V., and Priestley, M. G.: The Fermi surface in white tin . 1089
Groves, G. W., with Washburn, J., Kelly, A., and Williamson, G. K.: Electron microscope observations of deformed magnesium oxide . 991

Hadley, D. W., with Cundy, D. C., Evans, W. H., Mason, P., Newport, R. W., Smith, J. R., and Williams, P. R.: Systematic track distortion in a 10 in. diameter liquid hydrogen bubble chamber . 154
Hardy, J. R., and Karo, A. M.: Lattice vibrations of sodium chloride: Experimental and theoretical heat capacity data 859
Hardy, S. D., with Smith, S. D.: Activation of single phonon infra-red lattice absorption in neutron irradiated diamond 1311
Hartman, C. D., with Germer, L. H., and Scheibner, E. J.: Study of adsorbed gas films by electron diffraction 222
Hashimoto, H., Howie, A., and Whelan, M. J.: Anomalous electron absorption effects in metal foils 967
Haworth, C. W.: Measurement of the Debye–Waller temperature factor for silver and α-iron 1229
Heidenreich, R. D., with Burbank, R. D.: Microtwinning in epitaxial nickel–iron films 373
Hirsch, P. B., with Bailey, J. E.: The dislocation distribution, flow stress, and stored energy in cold-worked polycrystalline silver . 485
Hodgson, J. N.: Infra-red measurements of the optical constants of liquid silver 272
Hodgson, P. E., with Buck, B., and Maddison, R. N.: Optical model analysis of nuclear scattering 1181
Honeycomb, R. W. K., with Roberts, E.: Movement of point defects during fatigue of aluminium crystals 1147
Howie, A.: The electrical resistivity of stacking faults 251
Howie, A., with Hashimoto, H., and Whelan, M. J.: Anomalous electron absorption effects in metal foils 967
Hughes, D. G.: Nuclear magnetic resonance in lithium and dilute lithium–magnesium alloys 467
Hume-Rothery, W., and Anderson, E.: Eutectic compositions and liquid immiscibility in certain binary alloys 383

Johnson, A. A.: The embrittlement of molybdenum by neutron irradiation 413
Johnson, C. A.: The growth of prismatic dislocation loops during annealing 1255
Johnston, W. G.: An observation of crack formation in MgO . . . 407
Jones, G. O., and Smith, B. L.: The refractive indices of liquid and solid argon 355

Kane, J. V., Pixley, R. E., and Wilkinson, D. H.: Isotopic spin selection rules. XIV: Transitions between mirror states in ^{13}C and ^{13}N . 365
Kane, J. V., with Pixley, R. E., and Wilkinson, D. H.: Isotopic spin selection rules. XIII: The 6·92 MEV state of ^{16}O revisited . . 359
Karo, A. M., with Hardy, J. R.: Lattice vibrations of sodium chloride: Experimental and theoretical heat capacity data 859
Kauffman, J. W., with Meshii, M.: Recovery of quenched-in resistivity at high temperatures in gold 687
Kauffman, J. W., with Meshii, M.: The mechanism of quench-hardening and its recovery in gold 939

PAGE

Kelly, A., with Freise, E. J., and Fine, M. E.: The effect of electropolishing on the retention of vacancies during quenching in Al and Al alloys 101
Kelly, A., with Washburn, J., and Williamson, G. K.: Direct observation of dislocations in magnesium oxide 192
Kelly, A., with Washburn, J., Groves, G. W., and Williamson, G. K.: Electron microscope observations of deformed magnesium oxide . 991
Kemmey, P., with Clark, C. D., and Mitchell, E. W. J.: The infra-red absorption of hot semiconducting diamonds 127
Kendall, P. W., and Cusack, N. E.: Hall effect in liquid and solid mercury 100
Kronmüller, H., with Seeger, A., and Schiller, P.: Observation of interstitial atoms in f.c.c. metals 853

Le Claire, A. D., with Mortlock, A. J., and Rowe, A. H.: The atomic diffusion of platinum in gold 803
Lidiard, A. B.: The influence of solutes on self-diffusion in metals . 1171
Lovegrove, E., with Michell, D.: Investigation of the annealing of nickel deformed by compression by x-ray and stored energy measurements 499

MacDonald, D. K. C., Pearson, W. B., and Templeton, I. M.: Measurements of thermoelectricity below 1°K—IV 867
MacDonald, D. K. C., with Gold, A. V., Pearson, W. B., and Templeton, I. M.: The thermoelectric power of pure copper 765
Maddison, R. N., with Buck, B., and Hodgson, P. E.: Optical model analysis of nuclear scattering 1181
Makin, M. J., with Whapham, A. D.: The hardening of lithium fluoride by electron irradiation 237
Marsh, D. M.: Stress concentrations at crystal surfaces and the embrittlement of sodium chloride 1197
Martin, D. G.: The effect of lattice distortion around point defects on the scattering of long wavelength neutrons 1235
Mason, B. J., with Bryant, G. W.: Etch pits and dislocations in ice crystals 1221
Mason, P., with Cundy, D. C., Evans, W. H., Hadley, D. W., Newport, R. W., Smith, J. R., and Williams, P. R.: Systematic track distortion in a 10 in. diameter liquid hydrogen bubble chamber. . 154
Mayes, Valerie: A possible example of the muon radiative decay with internal conversion of the γ-ray 297
Mazey, D. J., with Barnes, R. S.: The nature of radiation-induced point defect clusters 1247
Meredith, J. E., with Sawkill, J.: The etching of sub-structures in beryllium 1195
Meshii, M., and Kauffman, J. W.: Recovery of quenched-in resistivity at high temperatures in gold 687
Meshii, M., and Kauffman, J. W.: The mechanism of quench-hardening and its recovery in gold 939
Michell, D., and Lovegrove, E.: Investigation of the annealing of nickel deformed by compression by x-ray and stored energy measurements 499
Mitchell, E. W. J., with Clark, C. D., and Kemmey, P.: The infra-red absorption of hot semiconducting diamonds. 127
Mitchell, E. W. J., Rigden, J. D., and Townsend, P. D.: The anisotropy of optical absorption induced in sapphire by neutron and electron irradiation 1013
Mitchell, J. W., with Bartlett, J. T.: The generation of dislocation loops at the surfaces of crystals of silver bromide. 445

PAGE

Mitchell, J. W., with Bartlett, J. T.: Dislocations with Burgers vectors of $a\langle 100\rangle$ in crystals of silver bromide 799
Morrison, J. A., with Beaumont, R. H., and Chihara, H.: An anomaly in the heat capacity of chromium at $38\cdot5$°C 188
Mortlock, A. J., Rowe, A. H., and Le Claire, A. D.: The atomic diffusion of platinum in gold 803
Myers, A.: Some elastic and thermal properties of zirconium and tungsten 927

Newman, R. C., with Bullough, R.: The spacing of prismatic dislocation loops 921
Newport, R. W., with Alston, Margaret H., Cundy, D. C., Evans, W. H., and Williams, P. R.: A 10 in. diameter liquid hydrogen bubble chamber 146
Newport, R. W., with Cundy, D. C., Evans, W. H., Hadley, D. W., Mason, P., Smith, J. R., and Williams, P. R.: Systematic track distortion in a 10 in. diameter liquid hydrogen bubble chamber . . . 154

O'Hara, S., with Gibbons, T. B.: The effect of internal oxidation on the damping capacity of copper–silicon alloys 140
Orbach, R.: On the scattering of phonons by spins at low temperatures: Theoretical 1303

Palma, M. U., with Ciccarello, I. S., and Palma-Vittorelli, M. B.: An electron spin resonance investigation of photographic processes in crystals of AgCl containing traces of CuCl 723
Palma-Vittorelli, M. B., with Ciccarello, I. S., and Palma, M. U.: An electron spin resonance investigation of photographic processes in crystals of AgCl containing traces of CuCl 723
Pearson, W. B., with Gold, A. V., MacDonald, D. K. C., and Templeton, I. M.: The thermoelectric power of pure copper 765
Pearson, W. B., with MacDonald, D. K. C., and Templeton, I. M.: Measurements of thermoelectricity below 1°K—IV. 867
Penfold, J., with Childs, B. G., and Gardner, W. E.: The magnetic susceptibility of vanadium–chromium solid solutions 1267
Petch, N. J., with Codd, I.: Dislocation-locking by carbon, nitrogen and boron in α-iron 30
Phillips, J. C.: Giant spin density fluctuations 1193
Phillips, V. A.: Direct observation of defects in evaporated silver . . 571
Piercy, G. R.: Point defects in platinum 201
Pixley, R. E., with Kane, J. V., and Wilkinson, D. H.: Isotopic spin selection rules. XIV: Transitions between mirror states in ^{13}C and ^{13}N 365
Pixley, R. E., Kane, J. V., and Wilkinson, D. H.: Isotopic spin selection rules. XIII: The 6·92 MeV state of ^{16}O revisited 359
Porter, N. A., with Bradley, E. F.: Observations on extensive air showers. VIII: The distribution in declination and curvature of the shower front 305
Price, P. B.: On microcreep in zinc whiskers 417
Price, P. B.: On the growth of cadmium crystals from the vapour . 473
Price, P. B.: Pyramidal glide and the formation and climb of dislocation loops in nearly perfect zinc crystals 873
Priestley, M. G.: Magneto resistance of copper, silver and gold . 111, 304
Priestley, M. G., with Gold, A. V.: The Fermi surface in white tin . 1089

PAGE

Prutton, M.: Cross-tie walls in thin permalloy films . . . 625
Puttick, K. E.: The shear component of ductile fracture . . . 759

Quenby, J. J., and Thambyahpillai, T.: Atmospheric temperature effects on the solar daily variation of cosmic ray intensity . . . 585

Rajopadhye, V. Y.: Nuclear interactions of 5·7 BeV protons in photographic emulsions 537
Reynolds, W. N., and Goggin, P. R.: The annealing of electron irradiation damage in graphite 1049
Rigden, J. D., with Mitchell, E. W. J., and Townsend, P. D.: The anisotropy of optical absorption induced in sapphire by neutron and electron irradiation 1013
Roberts, E., and Honeycomb, R. W. K.: Movement of point defects during fatigue of aluminium crystals 1147
Rochester, G. K., with Fernando, P. C. B., Spalding, I. J., and Smith, K. F.: The hyperfine structure of ^{121}Sb and ^{123}Sb . . . 1291
Rochester, G. K., with Fernando, P. C. B., and Smith, K. F.: The spin of ^{124}Sb and the spin and moments of ^{122}Sb 1309
Rosenberg, H. M., and Sujak, B.: On the scattering of phonons by spins at low temperatures: Experimental 1299
Rowe, A. H., with Mortlock, A. J., and Le Claire, A. D.: The atomic diffusion of platinum in gold 803
Runcorn, S. K.: Statistical methods in rock magnetism . . . 523

Sambell, R. A. J., with Clarke, F. J. P.: Microcracks and their relation to flow and fracture in single crystals of magnesium oxide . . 697
Sawkill, J., and Meredith, J. E.: The etching of sub-structures in beryllium 1195
Scheibner, E. J., with Germer, L. H., and Hartman, C. D.: Study of adsorbed gas films by electron diffraction 222
Schiller, P., with Seeger, A., and Kronmüller, H.: Observation of interstitial atoms in f.c.c. metals 853
Schoeck, G., and Tiller, W. A.: On dislocation formation by vacancy condensation 43
Seal, M.: The fine structure of films of rubber and other polymers . 78
Seeger, A., Schiller, P., and Kronmüller, H.: Observation of interstitial atoms in f.c.c. metals 853
Sheard, F. W.: The thermal conductivity of impure InAs at high temperatures 887
Shoenberg, D.: The de Haas–van Alphen effect in copper, silver and gold 105
Silcox, J., and Whelan, M. J.: Direct observations of the annealing of prismatic dislocation loops and of climb of dislocations in quenched aluminium 1
Smith, J. R., with Cundy, D. C., Evans, W. H., Hadley, D. W., Mason, P., Newport, R. W., and Williams, P. R.: Systematic track distortion in a 10 in. diameter liquid hydrogen bubble chamber. . 154
Smith, B. L., with Figgins, B. F.: Density and expansivity of solid krypton 186
Smith, G. C., with Ashby, M. F.: Direct electron microscopy of internally oxidized dilute copper alloys 298
Smith, B. L., with Jones, G. O.: The refractive indices of liquid and solid argon 355
Smith, K. F., with Title, R. S.: The hyperfine structure of ^{209}Bi . . 1281

PAGE

Smith, K. F., with Fernando, P. C. B., Rochester, G. K., and Spalding, I. J.: The hyperfine structure of ^{121}Sb and ^{123}Sb 1291
Smith, K. F., with Fernando, P. C. B., and Rochester, G. K.: The spin of ^{124}Sb and the spin and moments of ^{122}Sb 1309
Smith, S. D., and Hardy, J. R.: Activation of single phonon infra-red lattice absorption in neutron irradiated diamond 1311
Sondheimer, E. H., with Das, T. P.: Diamagnetic shielding of nuclei in metals 529
Spalding, I. J., with Fernando, P. C. B., Rochester, G. K., and Smith, K. F.: The hyperfine structure of ^{121}Sb and ^{123}Sb 1291
Sprackling, M. T.: Reverse bending of crystals of silver chloride . . 441
Sproull, R. L.: Charged dislocations in lithium fluoride 815
Stuckes, Audrey, A.: The thermal conductivity of germanium silicon and indium arsenide from 40°c to 425°c 84
Sujak, B., with Rosenberg, H. M.: On the scattering of phonons by spins at low temperatures: Experimental 1299

Templeton, I. M., with Gold A. V., MacDonald, D. K. C., and Pearson, W. B.: The thermoelectric power of pure copper 765
Templeton, I. M., with MacDonald, D. K. C., and Pearson, W. B.: Measurements of thermoelectricity below 1°K—IV 867
Thambyahpillai, T., with Quenby, J. J.: Atmospheric temperature effects on the solar daily variation of cosmic ray intensity . . 585
Thomas, A. T.: Unloading effects in aluminium and aluminium–zinc single crystals 947
Thompson, M. W.: The damage and recovery of neutron irradiated tungsten 278
Tiller, W. A., with Schoeck, G.: On dislocation formation by vacancy condensation 43
Title, R. S., and Smith, K. F.: The hyperfine structure of ^{209}Bi . . 1281
Townsend, P. D., with Mitchell, E. W. J., and Rigden, J. D.: The anisotropy of optical absorption induced in sapphire by neutron and electron irradiation 1013

Vandervoort, R., and Washburn, J.: On the stability of the dislocation substructure in quenched aluminium 24
Varley, J. H. O.: An approximate correlation between the electron Fermi energy and work function of a metal. 64
Verboven, E.: On the residual resistance of binary alloys . . . 753

Waddington, C. J.: The relative abundances of the heavy nuclei in the primary cosmic radiation 311
Waddington, C. J.: The determination of the flux of cosmic ray protons with nuclear emulsions 1105
Washburn, J., Kelly, A., and Williamson, G. K.: Direct observation of dislocations in magnesium oxide 192
Washburn, J., Groves, G. W., Kelly, A., and Williamson, G. K.: Electron microscope observations of deformed magnesium oxide. . . . 991
Washburn, J., with Vandervoort, R.: On the stability of the dislocation substructure in quenched aluminium 24
West, G. W.: Nuclear magnetic resonance in β brass 899
Westwood, A. R. C.: The effects of surface condition on the mechanical properties of lithium fluoride crystals 981
Whapham, A. D., and Makin, M. J.: The hardening of lithium fluoride by electron irradiation 237

PAGE

Whelan, M. J., with Hashimoto, H., and Howie, A.: Anomalous electron absorption effects in metal foils 967

Whelan, M. J., with Silcox, J.: Direct observations of the annealing of prismatic dislocation loops and of climb of dislocations in quenched aluminium 1

Whitworth, R. W.: Some effects of vibration on the internal friction of sodium chloride 425

Wilkinson, D. H., with Kane, J. V., and Pixley, R. E.: Isotopic spin selection rules. XIV: Transitions between mirror states in ^{13}C and ^{13}N 365

Wilkinson, D. H., with Pixley, R. E., and Kane, J. V.: Isotopic spin selection rules. XIII: The 6·92 MEV state of ^{16}O revisited . . 359

Williams, P. R., with Alston, Margaret H., Cundy, D. C., Evans, W. H., and Newport, R. W.: A 10 in. diameter liquid hydrogen bubble chamber 146

Williams, S. E., with Crisp, R. S.: The K emission spectrum of metallic lithium 525

Williams, S. E., with Crisp, R. S.: The soft x-ray spectra of lithium, magnesium and aluminium and their alloys. 1205

Williams, P. R., with Cundy, D. C., Evans, W. H., Hadley, D. W., Mason, P., Newport, R. W., and Smith, J. R.: Systematic track distortion in a 10 in. diameter liquid hydrogen bubble chamber . 154

Williamson, G. K., with Washburn, J., Groves, G. W., and Kelly, A.: Electron microscope observations of deformed magnesium oxide . 991

Williamson, G. K., with Washburn, J., and Kelly, A.: Direct observation of dislocations in magnesium oxide 192

Wohlfarth, E. P.: The anhysteretic remanence of magnetic recording tapes 717

Yoffe, Elizabeth H.: The angular dislocation 161

Ziman, J. M.: A note on the selection rules for optical transitions in alloys 757

END OF THE FIFTH VOLUME

Printed by Taylor & Francis Ltd
Red Lion Court, Fleet Street, London, E.C.4

U. of Haw